Alma Mater Studiorum - Università di Bologna

DOTTORATO DI RICERCA IN

Ingegneria Biomedica, Elettrica e dei Sistemi

Ciclo XXXIII

Settore Concorsuale: 09/E1

Settore Scientifico Disciplinare: ING-IND/31

NUMERICAL METHODOLOGIES FOR NON-EQUILIBRIUM PLASMA MODELLING

Presentata da: Arturo Popoli

Coordinatore Dottorato | **Supervisore**

Prof. Michele Monaci | Prof. Andrea Cristofolini

Esame finale anno 2021

Abstract

The development of reliable numerical tools for the simulation of non-equilibrium plasma devices is a fundamental requirement the technological progress. The main challenge in this context is to adequately represent multiple physical phenomena that take place over different temporal and spatial scales, while retaining reasonable computational performances.

In the first part of the work, a fluid methodology in which electrons are modelled using the Boltzmann relation is developed as an alternative to *Full Drift-Diffusion* models. The proposed *Boltzmann Drift-Diffusion* methodology allows to limit the drift-diffusion approach to the ionic species, granting substantial savings in terms of computational performances. Both methodologies are applied to the 1D/2D simulation of a volumetric Dielectric Barrier Discharge reactor, operating with air at atmospheric pressure. A semi-implicit numerical technique for the integration of plasma kinetic processes is presented and numerically validated against a well established implicit methodology. The *Boltzmann Drift-Diffusion* and *Full Drift-Diffusion* approaches are compared, showing a good agreement. The obtained results are validated against experimental measurements of the deposited surface charge on to the dielectric layers covering the electrodes.

In the second part of the work, a hybrid fluid/Particle-In-Cell approach is employed to model a miniaturized annular Hall thruster for space propulsion. The results yielded by two different treatments of the electron transport mechanism inside and outside the thruster channel are compared to macroscopic and microscopic physical information obtained through experimental measurements. These latter are then used to infer the anomalous transport collision frequency along the axis of the thruster. It is shown that the model can accurately predict the considered thruster performances and structure of the acceleration region, as well the measured fraction of doubly charged ions. The obtained efficiency of the two chemical kinetic channels for the doubly charged ions production is discussed and correlated with the computed spatial distribution of the species.

Acknowledgements

First of all, I want to thank prof. Andrea Cristofolini for the invaluable support he has given me throughout the last years, starting from my "adventurous" master thesis work. I am deeply grateful for the countless, patient explanations, and for sharing with me his passion for plasmas and science

I also wish to express my gratitude to Dr. Laurent Garrigues for accepting me as a visiting student at the LAPLACE laboratory, and for his scientific guidance during (and after!) my stay in Toulouse

I owe much gratitude to my mother, my father and the rest of my family for the endless support through all these years

. . . speaking of family, I want to thank Alberto: he is responsible for the word "space" appearing so many times in this work

Lorenzo, Andrea, Diego and Umberto: thank you for the time we have spent together inside and outside the university during the last three years

Thanks to my friends, wherever they are. Each of you deserves much more than a few words, so I'll simply say it again: thank you

Finally, I want to thank Silvia. This work is dedicated to you

Contents

1 Introduction **1**

1.1 Non-Equilibrium plasmas 1

1.2 Technological applications 2

1.3 Motivation 3

1.4 Thesis outline 6

1.5 Dielectric Barrier Discharges 8

1.6 Hall Thrusters 9

1.7 Hall thruster functioning principle 11

2 Fluid model of an atmospheric pressure dielectric barrier discharge **15**

2.1 Drift-diffusion approach 15

2.2 Electrostatics 17

2.2.1 Linear and nonlinear electrostatic formulations 17

2.2.2 Linear and nonlinear electrostatic formulations comparison 19

2.2.3 Charge accumulation at dielectric interfaces 20

2.3 Drift-diffusion equation finite volume discretization 21

2.3.1 Numerical flux evaluation 23

2.4 Electrostatics finite volume discretization 24

2.4.1 Interface between two materials 26

2.4.2 Algebraic system for electrostatics 27

2.4.3 Nonlinear Poisson equation solution 28

2.5 Time discretization 34

2.6 Source terms integration 35

3 Simulation Results **38**

3.1 Numerical code description 38

3.1.1 Mesh generation 39

3.1.2 Species initial distribution . . . 40
3.1.3 Macroscopic transport parameters . . . 41
3.1.4 Drift-diffusion fluxes integration . . . 42
3.1.5 Linear and non-linear Poisson solvers . . . 45
3.1.6 Plasma kinetics . . . 46
3.1.7 Plasma-wall interaction . . . 49
3.2 Simulation of a DBD volumetric reactor . . . 51
3.2.1 DBD reactor description . . . 52
3.2.2 Applied voltage and surface charge density . . . 52
3.2.3 Spatial distribution of the charged species . . . 56
3.3 Comparison between different electron models . . . 62
3.4 Surface charge density experimental measurements . . . 67
3.4.1 High-voltage multilevel generator . . . 68
3.4.2 Surface charge density measurement procedure . . . 69
3.4.3 Comparison between simulations and experimental results . . . 70
3.4.4 Influence of the initial ionization degree . . . 74

4 Particle Modelling **77**
4.1 Electrostatic Particle-in-Cell . . . 79
4.1.1 Particle Mover . . . 80
4.1.2 Scattering and Gathering . . . 84
4.1.3 Field Solution . . . 86
4.1.4 Collisions . . . 89

5 Numerical simulations of a 20 W annular Hall thruster **91**
5.1 Chapter Overview . . . 91
5.2 Numerical Methodology . . . 91
5.2.1 Ions and neutrals . . . 91
5.2.2 Electrons . . . 93
5.2.3 Anomalous transport . . . 97
5.2.4 Magnetic field calculation . . . 99
5.3 Simulation Results . . . 100
5.3.1 Mode B . . . 103
5.3.2 Mode A . . . 118

5.4 Summary 121

6 Conclusion **123**

List of Figures

1.1 Basic dielectric-barrier discharge configurations, after [1] 10
1.2 Schematic representation of a Hall thruster, after [2] 12

2.1 Sketch of a plasma-dielectric interface 21
2.2 Generic node centered volume 23
2.3 Interface between two mesh nodes 25
2.4 Control volume shared between plasma and dielectric 26
2.5 Electric potential, charge density, and electronic number densities over a 5 mm domain, obtained from the nonlinear Poisson problem solution with uniform density of ions, $\phi_0 = 0\,\mathrm{V}$ and $\phi_1 = 5\,\mathrm{V}$, $\phi_n = -5\,\mathrm{V}$ 30
2.6 Total electric charge dependence from the employed reference electric potential; The minimum value of Q_t, corresponding to the required charge neutrality condition, is pointed out 31
2.7 Sub-cycling of the semi-implicit solver employed to perform the time-integration of the plasma kinetics source terms 37

3.1 Example of a 2D regular non-uniform grid, with a refinement of the spacing towards the boundaries of the discretised domain 39
3.2 Electrical mobility for ions and electrons in atmospheric pressure dry air computed with the expressions in Table 3.1 for $T = 400\,\mathrm{K}$ and $T_e = 2\,\mathrm{eV}$ (a), and corresponding drift velocity (b) 43
3.3 Comparison between the described semi-implicit numerical scheme and the TR-BDF2 [3, 4] integration method; Time evolution of the charged species considered in [5], with $|E| = 200\,\mathrm{Td}$ 49
3.4 Sketch of the control volume V_i, shared between the generic dielectric layer and the gap; Δy and d are the dielectric layer width and thickness, respectively; the spacing between the nodes in the gap is Δx 50

3.5 Schematic representation of the modeled Dielectric Barrier Discharge reactor volumetric reactor 51

3.6 Electric potential difference over the gap ($\Delta\phi_{gap}$) during the first two cycles of the externally applied voltage (V_{ext}); The spatial distribution of the species number densities and electric potential is discussed at time-instants τ_{1-4} 54

3.7 Surface charge density deposited onto dielectric layers I and II (see Fig. 3.5), over two cycles of the externally applied voltage (V_{ext}) 55

3.8 Electric potential difference over the gap (a) and surface charge accumulated on the dielectric layers (b) when a a frequency of 10 MHz is employed 56

3.9 (τ_1) - number density and electric potential over the air gap after 67 µs since the beginning of the simulation 57

3.10 (τ_2) - number density and electric potential over the air gap after 83 µs since the beginning of the simulation 59

3.11 (τ_3) - number density and electric potential over the air gap after 87 µs from the beginning of the simulation 60

3.12 (τ_4) - number density and electric potential over the air gap after 90 µs from the beginning of the simulation 61

3.13 Total current density (J) computed at the midpoint of the gap during the first two cycles of the performed simulation, plotted against the externally applied voltage (V_{ext}) and the electric potential difference applied to the gap ($\Delta\phi_{gap}$) 62

3.14 Simulation of the volumetric Dielectric Barrier Discharge reactor described in Sec. 3.2 with two different numerical methodologies; Comparison between the gap voltage obtained with the *Full Drift-Diffusion* (FDD) and *Boltzmann Drift-Diffusion* (BDD) approaches 63

3.15 Surface charge density deposited onto dielectric layers I and II (see Fig. 3.5), over two cycles of the externally applied voltage; Comparison between the *Full Drift-Diffusion* (FDD, black line) and *Boltzmann Drift-Diffusion* (BDD, red line) approaches 65

3.16 Spatial distribution of ${N_2}^+$ and e^- (left) and electric potential (right) yielded by the *Full Drift-Diffusion* (FDD, solid lines) and *Boltzmann Drift-Diffusion* (BDD, dashed lines) approaches at τ =57 µs 67

3.17 Geometry of the employed Dielectric Barrier Discharge reactor 68

3.18 Handling of the electrostatic probe employed to perform the described measurements of deposited charge on surfaces of the dielectric layers . . . 70
3.19 Numerical results for Test I, configuration with two dielectrics; Externally applied voltage, gap voltage and surface charge deposited on the dielectric layers obtained with the *Boltzmann drift-diffusion* methodology 73
3.20 Numerical results for Test II, configuration with one dielectric (covering the HV electrode); Externally applied voltage, gap voltage and surface charge deposited on the dielectric layer obtained with the *Boltzmann drift-diffusion* methodology 74
3.21 Distribution of O3 number density ($\log(n_{03})$) obtained from the simulation of the symmetric configuration corresponding to Test I, after 86 µs 75
3.22 Left Axis: temporal evolution over one period at 15 kHz of the average number density in the gap, starting from two different initial ionization rates; Right Axis: maximum electric field in the gap during the same time interval. 76

4.1 Typical scheme of a collisionless electrostatic PIC simulation cycle 80
4.2 Scheme of the Leapfrog integrator 82
4.3 Schematic representation of the NGP (a) and CIC (b) weighting schemes, applied to a 1D spatial grid 87
4.4 Typical scheme of a an electrostatic Particle-In-Cell code including a Monte Carlo Collision (MCC) module 89

5.1 2D (r-z) example of grid for ions and neutrals (left) and 1D (λ) grid for the electrons, from [6]. Both grids are delimited by the anode position and the magnetic field line intersecting the cathode 94
5.2 Singly and doubly charged Xe ions electron impact cross sections (a); corresponding rate coefficients (b) 95
5.3 KmHT-20 magnetic field; (a) magnetic field magnitude and magnetic field lines in proximity of the channel exit; (b) magnetic field radial component; (c) magnetic field axial component; (d) magnetic field along the channel axis 101
5.4 Mean ion velocity outside the KmHT-20 channel exit, obtained with LIF measurements (courtesy of KEPL research group) 102

5.5 Mode B (200V; 0.42 $\mathrm{mg\,s^{-1}}$) – computed values of thrust (a), discharge current (b), anode efficiency (c) and ratio between the ion and electron current at the cathode (d) as a function of empirical parameters α (wall momentum losses) and k_b (Bohm anomalous transport) 106
5.6 (a,c) electric potential and mean ion velocity along the thruster channel axis, comparison between the computed velocities and the LIF measurements; (b,d) electron collision frequency along the channel axis; (a,b) refer to CASE I ($\alpha = 3$, $k_b = 0.25$), (c,d) correspond to CASE II ($\alpha = 4, k_b = 0.125$); the black, dashed line in (a) and (c) marks the channel exit 108
5.7 Ratio between the voltage drop after the channel exit and the total voltage drop $V_{ext}/(V_{ext} + V_{in})$ as a function of empirical parameters α and k for operational mode B 109
5.8 (a) electric potential and mean ion velocity along the thruster channel axis, comparison between the computed velocities and the LIF measurements; (b,d) electron collision frequency enforced along the channel axis . 110
5.9 (a) electric potential and mean ion velocity along the thruster channel axis, comparison between the computed velocities and the LIF measurements for the same conditions of Fig. 5.8, with the additional constraint of $I_d = I_d^*$; (b) employed anomalous collision frequency values along the channel axis (ν_{an}) 112
5.10 Ion energy distribution function computed at the cathode line; the black (solid and dashed) lines have been obtained with the empirical methodology described in the previous section, based on empirical coefficients for the anomalous electron transport; the green line correspond to the manually enforced anomalous frequency profile in Fig 5.9b 114
5.11 (a) ionization source terms and mean electron density along the thruster channel axis when the anomalous electron collision frequency in Fig. 5.9b is enforced; (b) corresponding axial distribution of neutral and ionized Xe 116
5.12 Experimental (red) and simulated (black) I-V characteristic for the KmHT-20 annular Hall thruster; The simulated results have been obtained with the anomalous collision frequency profile ν_{an} shown in Fig. 5.9, using a fixed flow rate of 0.42 $\mathrm{mg\,s^{-1}}$ 117

5.13 Mode A (160V; 0.32 $\mathrm{mg\,s^{-1}}$) – thrust (a), discharge current (b), efficiency (c) and ratio between the voltage drop after the channel exit and the total voltage drop along the thruster channel axis (d) as a function of empirical parameters α (wall momentum losses) and k_b (Bohm anomalous transport). 119
5.14 Simulation of mode A using empirical parameters for anomalous electron transport ($\alpha = 4$,$k_b = 0.875$); (a) electric potential and mean ion velocity along the thruster channel axis, comparison between the computed velocities and the LIF measurements; (b) employed anomalous collision frequency values along the channel axis 120
5.15 Simulation of mode A enforcing the anomalous collision frequency along the thruster channel axis; (a) electric potential and mean ion velocity along the channel axis, comparison between the computed velocities and the LIF measurements; (b) employed anomalous collision frequency values 121

List of Tables

3.1 Electrical mobility coefficients for ions and electrons in dry air, from [5]; N is the background neutrals density [m^{-3}], T the heavy ions temperature [K] and T_e the electron temperature [K] 41
3.2 List of considered kinetic processes, along with the relevant reference . . 47
3.3 Physical characteristics of the modeled Dielectric Barrier Discharge reactor 52
3.4 Measurements of the electrostatic potential induced by the surface charge deposited on the dielectric layers of a symmetric (Test I) and asymmetric (Test II) Dielectric Barrier Discharge volumetric reactor 71

5.1 Target experimental results for Mode A and Mode B 103
5.2 Settings employed for the performed simulations 103
5.3 Comparison between the measured (EXPER) and computed (*HALLIS*) thruster performances for operational mode B, using empirical parameters for the electron anomalous transport 106
5.4 Thruster performances of the KmHT-20 AHT with V_a =200 V, flow rate = 0.42 mg s^{-1}. The three rows correspond to the experimental results and the *HALLIS* results obtained using the two anomalous collision frequency profiles of Fig. 5.8b and 5.9b, respectively. 112
5.5 Mode A, comparison between the measured thruster performances and results obtained enforcing the anomalous frequency profileν_{an} depicted in Fig. 5.15b. 121

1 Introduction

1.1 Non-Equilibrium plasmas

This work deals with the development of numerical models for the simulation of devices operating with non-equilibrium plasmas. One of the most commonly employed ways to artificially obtain a non-equilibrium plasma is through a gas discharge. An electric field is applied across a gas, which accelerates free electrons to energies sufficiently high to ionize other atoms by collisions. One characteristic of this process is that the applied electric field transfers energy more efficiently to the light electrons than to the relatively heavy ions [6]. The subsequent thermal energy transfer from electrons to the heavy particles through collisions requires a characteristic relaxation time τ, that can be large compared to the discharge observation time scale. In non-equilibrium (cold) plasmas, then, the electron temperature (T_e) is considerably higher than that of the ions (T_i) and neutrals (T_n). It is worth noticing that, while a non-thermal plasma is not sufficiently collisional to reach thermal equilibrium between the different species, the latter can be individually at thermodynamic equilibrium. In this case, the plasma is said to be in partial thermodynamic equilibrium, and the velocity distribution functions of electrons and ions are both Maxwellian, albeit having different mean energies $\epsilon_e \neq \epsilon_i$. In contrast, collisions between electrons, ions and neutrals in thermal plasmas are so frequent that thermodynamic equilibrium conditions are obtained in very short times from the discharge onset. Examples of thermal plasmas on earth can be constituted by high-intensity electric arcs, plasma torches or radio frequency discharges at or above atmospheric pressure [7].

1.2 Technological applications

Because of the relative ease with which a non-thermal plasma can be produced on earth, a great deal of attention has raised over the decades around the employment of such kind of plasmas for a multitude of industrial, aerospace and medical applications.

Industry and environment

Non-thermal plasmas can be used to treat surfaces and volumes in both direct and indirect ways. Treatments performed using non-thermal plasmas are also non-destructive and highly energetic [8]. In addition, non-thermal plasmas produce a remarkable number of chemically active species in economically convenient ways [9]. These are the primary features that make plasma technologies so interesting from an industrial point of view.

Typical examples of industrial uses of non-thermal plasmas at atmospheric pressure include the production of ozone for air cleaning [10, 11], controlled deposition of thin-films [12, 13], and the reduction of thin oxide layers [14, 15]. The surfaces of polymers [16], ceramic materials and metals are often treated with technologies based on non-equilibrium plasmas [17]. Other important applications include plasma display panels [18, 19], ultraviolet light sources [20] and plasma assisted combustion. The presence of free radicals generated by the plasma can indeed improve engine performances, increase the stability of flames and reduce emissions [21].

The environmental applications include treatment and conversion of Greenhouse gases [22], electrostatic precipitation for the cleaning of air from fumes and particulates [23], as well as exhaust gases of internal combustion engines and incinerators and contaminated air produced variety of different sources [24].

Aeronautics and space

In the aeronautic community, plasma actuators are employed to mitigate the detrimental effects of shock waves in supersonic/hypersonic flights. Indeed, the effective aerodynamic shape and the efficiency [25] of aircraft can be improved through the counter-flow injection of plasmas [26]. At lower flight speeds, Dielectric Barrier Discharge (DBD) plasma actuators are employed to perform active control of flow over aerodynamic bodies, without the need of moving parts or relevant additional weight [27]. Indeed, DBD actuators have demonstrated their usefulness in preventing or to induce flow separation and the possibility to reduce drag and to enhance the lift of airfoils [28].

Regarding the space applications, plasma thrusters are gradually challenging the monopoly of chemical thrusters for the tasks of satellite/spacecraft displacement (in space) and its attitude control [29]. Plasma propulsion uses electric energy to ionize the gas propellant and then impart kinetic energy to the resulting plasma, generating thrust through action and reaction principle. The reasons behind the considerable interest that has been grown in recent decades around plasma propulsion is due to both technical and economic reasons. Plasma thrusters can indeed perform complex orbital manoeuvres since the produced thrust can be easily controlled, and attain considerably faster exhaust speeds compared to chemical rockets [2].

Medicine

Because the ions and the neutrals of a non-thermal plasma remain relatively cold, the plasma can come in contact with biological tissues without causing any thermal damage. This characteristic opens up the possibility of using these plasmas for the direct and indirect treatment of heat sensitive materials, including biological tissues [7]. Thanks to these properties, non-equilibrium plasmas have been applied in the field of electrosurgery [30] tissue engineering [31] and surface modification of bio-compatible materials [32,33]. Non-equilibrium plasmas at atmospheric pressure conditions are characterized by the presence of a multitude of active chemical species such as reactive oxygen species (ROS), reactive nitrogen species (RNS) and free radicals [34]. These species, together with the ions and free electrons, can be conveniently exploited for sterilization of heat-sensitive medical instruments [35]. Moreover, radicals and excited species in the plasma can be used for pathogens inactivation, performed by directly damaging the capsid of viruses. This kind of approach has already been successfully employed for the tasks of surface disinfection and inactivation [36, 37], and several interesting preliminary results have recently been obtained in the disinfection of air streams [38].

1.3 Motivation

In Sec. 1.2, a number of different applications (in different sectors) for technologies based on non-equilibrium plasmas has been listed. The main reason behind the reported vastness and diversity of non-thermal plasma applications lies indeed in the rich physics that characterizes this physical state. The quantity and complexity of the different phenomena taking place in non-equilibrium plasmas, however, also constitutes a challenge from the perspective of understanding, operating and optimizing technologies based on these principles. In this context, considering the high costs associated with prototyping and experiments, the development of reliable tools allowing to perform numerical simulations plays a very prominent role in technological and scientific advancement.

The task of simulating the physical mechanisms involved in non-thermal plasma physics, however, comes by no means without major challenges. From a modelling perspective, the overall behaviour of a plasma device is influenced by the combination of a large number of different physical contributions, that must be correctly addressed. The charged species constituting the plasma respond – in reason of their (different) physical characteristics – to both (external and self-induced) electric and magnetic fields, as well as density gradients. The distributions of charged and neutral species are then subjected to chemical processes, which in turn depend on both the dynamics of the species and their energies. In addition, non-thermal plasmas are often confined by some kind of dielectric or metallic vessels or walls. The interaction between these latter and the charged species constitutes another fundamental influence on the overall plasma behaviour, involving both chemical and electromagnetic aspects.

In order to adequately capture the mentioned mechanisms taking place in a plasma device, a key role is excerpted by whether a fluid or kinetic physical description is performed. Indeed, the spectrum of different ionization rates (1×10^{-10} to 1×10^{-3}) and electron energies (0.1 eV to 10 eV) encountered in typical applications of non-equilibrium plasmas is such that both approaches are commonly adopted, depending on the specific characteristics of the considered application. A further challenge is constituted by the fact that, as well known, the boundary between whether a fluid approach should be employed instead of a kinetic one and vice versa is often blurred. As an example of this, one can consider a DBD device operating at atmospheric air pressure. In reason of the high pressure conditions and collisional regimes established in these devices, fluid models are often employed to describe DBD devices on the time-scales of the employed supply voltage waveforms. Contextually, streamer discharges – constituting one of the main fundamental processes in a DBD – are also modelled with kinetic approaches (such as Monte Carlo simulations and Particle-In-Cell (PIC) models) on considerably shorter time-scales [39]. The employment of kinetic approaches allow to avoid expressing the electron energy distribution as a function of the local reduced field strength or the electron average energy, as usually performed in fluid approaches under the assumption of a Maxwell-Boltzmann distribution. In this way, a more accurate description of the considered collisional phenomena – which play a fundamental role in the streamer development – is obtained through a detailed representation of the velocity distribution function.

In this work, both fluid and kinetic approaches are employed to model a DBD reactor operating with atmospheric air pressure and a miniaturized Hall thruster for space propulsion. Even if the practical scopes of these two technologies are completely different, the challenges involved in the process of modelling these devices are surprisingly similar. In both cases, indeed, the large difference between the dynamics of the electrons and the heavy species – leading to unpractical computational loads – is the driver for the development of hybrid approaches, where electrons are assessed using a different approach with respect to the ions. Moreover, in both cases a key role is played by the physics taking place at the considered plasma region boundaries. Considering the modelled DBD reactor, the surface charge deposited on to the dielectric layers heavily affects the gap voltage, as well the population of the species inside the gap through secondary emission, recombination and attachment phenomena. An equally important role is played by the annular channel Boron Nitride inner walls of the considered Hall thruster. Indeed, the electron-wall collisions are the main source of the so-called *anomalous* transport inside the thruster channel, allowing the electrons to partially escape the magnetic confinement and travel towards the thruster anode. Again, similarly to the case of DBDs, the walls secondary emission coefficient excerpts a marked influence on both the density of electrons inside the considered devices and their velocity distribution function.

Summarizing, the challenges associated with the modelling of electronic transport and the effects exerted by the walls on the charged species are common to a multitude of different non-equilibrium plasma applications. As technological development moves forward, the computational resources that can be devoted to the simulation of these devices will significantly increase. In this way, thanks to the contextual development of parallel computing techniques both on CPUs and GPUs, kinetic and hybrid approaches will gradually be extended to the applications that are currently being modelled mainly through fluid models.

1.4 Thesis outline

In Chapter 2, a general fluid model (valid in one, two or three dimensions) is presented, devoted to the numerical simulation of non-equilibrium plasma devices operating at atmospheric pressure. The adoption of a fluid approach for the physical description of such phenomena is justified by the highly collisional regime due to the atmospheric pressure operation. Indeed, at such pressures the collision rates are high enough for electrons to reach thermal equilibrium conditions corresponding to the local electric field within picoseconds [1]. The developed approach is based on the Finite Volume solution of the continuity equation for the charged species, written under the drift-diffusion approximation. The operator-splitting technique is employed to separate the integration of the two contributions to the particle fluxes from both the electrostatic problem solution and the kinetic source terms integration. Two different approaches are discussed, with respect to the electron transport modelling. In the first proposed methodology, named *Full Drift Diffusion* (FDD) approach, the electron fluxes due to diffusion and advection are computed with the same technique employed for the heavy species. Hence, at each time-step, a linear Poisson electrostatic solver can be employed to compute the electric potential distribution due to externally applied voltages, as well as volume and charge density distributions. Conversely, in the other proposed technique – named *Boltzmann Drift Diffusion* (BDD) – the electrons are assumed to instantaneously adapt their position to the local electrostatic field caused by external applied voltages and the motion of the (slower) heavy ions. Hence, their spatial distribution is computed using the Boltzmann relation, leading to a non-linear electrostatic Poisson problem. The two approaches are then compared, and the employed numerical methodologies for the Poisson problem solution are discussed. The same is performed for the explicit time-integration of the number density fluxes, and a semi-implicit numerical approach for the plasma kinetic source terms integration is presented.

In Chapter 3, the fluid approach introduced in Chapter 2 is applied to the numerical simulation of a DBD volumetric reactor, operated in atmospheric pressure air. The development of the fundamental parts of a 1D/2D computational code implementing the proposed approach is discussed from the perspective of two markedly different computer languages, i.e., Matlab and Fortran 90. First, the criteria employed for the generation of non-uniform grids allowing to resolve the Debye length in the sheaths are described. Then, the different ways in which the distributions of charged species are injected into the computational domain are considered, as well as the implemented methodologies for the computation of the macroscopic transport parameters. The latter are expressed as a function of the local reduced electric field value under the Local Field Approximation (LFA). The latter is adopted under the assumption that the charged species gain energy from the electric field, and lose it locally as a result of collisions. Afterwards, the dimensionless forms of the employed conservation equations and electrostatic formulation are derived, and the set of reactions used to represent the source terms due to chemical kinetic processes. The developed semi-implicit numerical scheme is compared to a well-established implicit solver, and the methodology employed to account for the surface charge deposition in the dielectric layers due to positive and negative charged fluxes is presented. The remaining part of the chapter is devoted to the discussion of the simulation results obtained using both the FDD and BDD approaches. The trends in obtained gap voltage and deposited surface charge are shown during two cycles of the 15 kHz applied sinusoidal waveform. The detailed spatial distribution of the species number density and obtained electric potential are discussed at several key-moments of the considered simulation. Finally, the FDD and BDD approaches are quantitatively compared, and the computed values of deposited surface charge density are validated by means of experimental measurements.

In Chapter 4, kinetic numerical approaches are compared to fluid models from the perspective of non-equilibrium plasma modelling. It is highlighted how kinetic approaches allow to avoid a series of physical assumptions on the energy distribution function of the considered plasma species that are inherent to fluid models. Subsequently, the fundamental features of the Electrostatic Particle-In-Cell (ES-PIC) approach are presented and discussed. This is performed aiming to provide an introduction to the following chapter, where a hybrid fluid/Particle-In-Cell code is applied to the task of modelling the physical behaviour of a Hall plasma thruster. The typical scheme of a simple collisional ES-PIC code is firstly presented, together with a discussion on the different schemes that can be adopted to account for the dynamics of the considered species. Different weighting techniques – employed to *gather* the values of fields on to the particle positions and to *scatter* the particles and their velocities to the grid nodes – are also discussed. Finally, a Monte Carlo procedure to account for the effects of collisions between the considered particles is presented.

In Chapter 5, a hybrid fluid/Particle-In-Cell code is employed to study a miniaturized

Hall thruster for space propulsion. The employed code – *HALLIS* – simulates the plasma physics taking place both inside and outside the thruster annular channel in two dimensions, exploiting the axial symmetry typical of these devices. The numerical model implemented in *HALLIS* is hybrid, in the sense that the kinetic approach is only employed to describe the dynamics of the heavy species, while a fluid approach is used to solve the electron transport and energy equations. This is possible thanks to the assumption that the electrons – magnetized by a static radial magnetic field – are in thermodynamic equilibrium conditions along the magnetic field lines. Since a fluid approach is employed for the physical description of the electrons, their mobility must be expressed through empirical macroscopic transport coefficients. The code is employed to compute the main macroscopic performances of the thruster under different discharge voltages and gas propellant flow rates. The considered figures of merit include thrust, discharge current, specific impulse and efficiency. The obtained thruster performances are compared against experimental measurements. Then, thanks to the availability of Laser Induced Fluorescence (LIF) measurements of the ions velocity distribution function, the macroscopic electron transport coefficients are adapted to accurately match the microscopic information on the dynamics of the ions. The obtained results are discussed for two specific operational modes of the considered annular thruster, and the observed production rate of doubly charged Xenon is analysed and compared to experimental measurements.

1.5 Dielectric Barrier Discharges

Among the different kinds of non-thermal plasma sources, a particularly relevant role is played by the Dielectric Barrier Discharges. Originally developed and employed for ozone generation [40], the DBD is nowadays employed in broad spectrum of scientific, industrial and biomedical applications.

The DBD shares many features with the corona discharge, although the latter term is preferred for discharges between bare metal electrodes without dielectric (other than the gas gap) [1]. Also, corona discharges are usually operated in DC or pulsed DC regime, whereas DBDs require AC voltage sources (from low frequencies up to MHz) or nanopulses. In a corona discharge, a strong electric field is produced near the high voltage (HV) electrode, which accelerates the free electrons in the considered gas (often air). The electrons, in turn, ionize the surrounding gas, generating a plasma in the electrode surroundings [41]. Although corona is employed for material surface treatments and bacterial decontamination, its industrial use is limited by the non-uniformity of the produced plasma, leading to non-homogeneous treatments [42]. Moreover, the discharge volumes are rather small, limiting the use of corona treatment devices to small surfaces [43].

In a DBD device, the non-uniformity of corona discharge is avoided introducing a dielectric barrier in the discharge gap. As shown in Fig. 1.1, either one or both the electrodes are covered with a dielectric layer. This has the effect of limiting the electric current and preventing spark formation [44]. It is important to remark that the nature of the discharge taking place in the gas gap between the electrodes depends (among other parameters) on the kind of employed gas, on the geometry and the characteristics of the employed dielectric layers. Hence, the characteristics of the discharge regime produced by a DBD device can be controlled through an appropriate choice of operating conditions, geometry and employed materials.

Another key difference between the corona and DBD discharge is the characteristic charge accumulation process that takes place in the dielectric layers for this second kind of device. Indeed, the electric potential due to the dielectric surface charge generates an additional electric field with respect to the *external* field due to the electrodes potential. The dielectric layers in a DBD serve a twofold purpose: it limits the amount of charged transport by a single micro discharge, and it distributes the micro discharges over the entire electrode surface. The displacement current can pass through the dielectric film by an alternative electric potential source, thus the circuit is closed. However, the distinctive feature of DBD is constituted by the accumulated charges over the dielectric layers that excerpts the effect of reducing (or, occasionally, increasing) the local electric field intensity, causing a self-limiting behaviour characteristic of this type of discharges [45].

1.6 Hall Thrusters

A Hall thruster belongs, along with its gridded counterpart – the ion thruster – to the category of electrostatic thrusters. The main idea behind these devices is to accelerate the gas propellant through the application of a body force. A stream of ions (produced by ionization of the propellant), is accelerated by an electric field, generated between

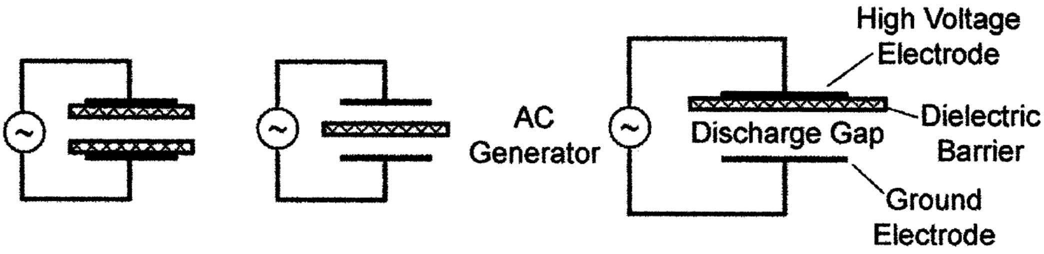

Figure 1.1: Basic dielectric-barrier discharge configurations, after [1]

an anode (also serving as neutral gas injector) and an external cathode. The external cathode also provides a stream of electrons used as primary electrons to ignite the discharge and to neutralize the ions accelerated by the electric field. In absence of collisions, the velocity of the ions leaving the thruster is determined by the total potential drop between the anode and the cathode and by the charge-to-mass ratio of the employed ions. The maximum velocity that can be imparted to the ions is defined as:

$$v_i = \sqrt{\frac{2eV_d}{m_i}} \tag{1.1}$$

where V_d is the discharge voltage and m_i the mass of the considered ions. Experimentally, the mean ion energy in well-developed thrusters correspond to 70 % to 90 % of V_d [46]. The obtained thrust depends on the propellant mass flow rate and exit speed [47], which can be approximated with m_i and v_i due to the velocity of the ions greatly exceeding that of the neutral gas propellant:

$$T = \dot{m} v_{ex} \approx \dot{m}_i v_i \tag{1.2}$$

The considerable exit speed that can be obtained in a Hall thruster ($10\,\mathrm{km\,s^{-1}}$ to $30\,\mathrm{km\,s^{-1}}$) can be conveniently employed to obtain the change of speed required to perform a given maneuver (Δv), defined as:

$$\Delta v = v_{ex} \ln\left(\frac{m_f}{m_0}\right) \tag{1.3}$$

In this expression, v_{ex} is the ejected propellant speed, while m_0 is the mass of the considered spacecraft at the beginning and end of the mission, respectively. In comparison, values of v_{ex} achieved by conventional chemical thrusters are typically one order of magnitude lower. This peculiarity of the Hall (and on) thrusters allow to considerably reduce the embarked propellant mass, leading to relevant advantages in terms of mission cost and spacecraft size.

The efficiency of a plasma thruster is defined as the ratio between the power imparted to the expelled jet and the electric power (P_{el}) provided to the thruster. The efficiency can be defined with:

$$\eta = \frac{T^2}{2\dot{m}P_{el}} \tag{1.4}$$

This figure of merit is sometimes referred to as *anode efficiency*, neglecting the power consumption of the cathode. Hence, the electric power in the denominator of Eq. (1.4) is simply given by the product of the anode voltage V_a and the discharge current I_d.

Compared to ion thrusters, Hall thrusters cannot reach the same levels of specific impulse (Isp), defined as:

$$Isp = v_{ex}/g, \tag{1.5}$$

where g is the gravitational acceleration. Moreover, they suffer from larger plume divergence, which can lead to highly energetic particles impacting sensitive spacecraft parts, such as solar panels.

Conversely, Hall thrusters exhibit higher thrust at the same power level. Additionally, Hall thrusters can be operated at lower voltages and require fewer power supplies to be operated [2]. Finally, the ion current in a Hall thruster is proportional to the neutral gas flow rate, and independent from the operating voltage. This is a very interesting property, as it allows to operate the thruster at maximum thrust (for orbit insertion) or maximum specific impulse (for station keeping), making it suitable for a large span of different missions [29].

1.7 Hall thruster functioning principle

Figure 1.2 depicts a schematic representation of a typical annular hall thruster configuration. An electrically biased metallic anode is positioned at the closed end of an annular channel. The anode often serves the additional purpose of introducing the neutral gas in the channel. The most common propellant for this kind of thrusters is Xenon.

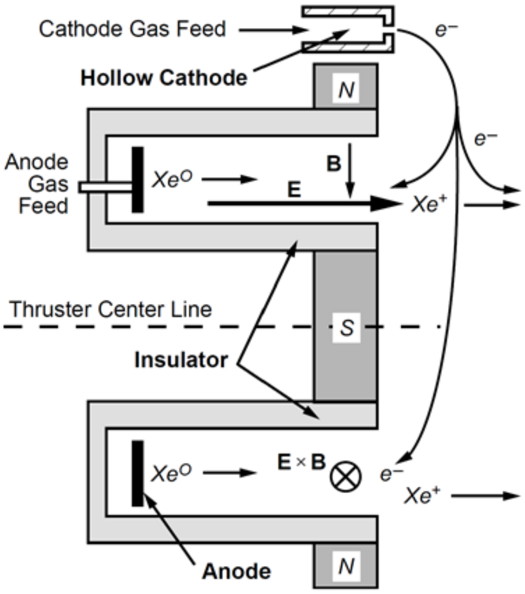

Figure 1.2: Schematic representation of a Hall thruster, after [2]

While this choice could seem counter intuitive, as the imparted ions speed decreases with the ions mass, the reason for the popularity of the Xenon is that it features a low ionization threshold, around 12 eV. The benefit of this choice is that it allows the employment of lower voltages and hence less stringent requirements for the electrical power circuit.

The channel walls can either be made of metal or a dielectric material, such as boron nitride (BN). In the latter case, the device takes the name of Stationary Plasma Thruster (SPT), while the name Thruster with Anode Layer (TAL) is employed when conductive walls are used. From here onward, only thrusters with dielectric walls will be considered.

The neutral Xenon injection does not only take place at the anode. Indeed, a (smaller) part of the Xe flow rate is provided through an external cathode. The cathode completes the electric circuit and provides a flux of electrons. Part of these electrons neutralize the ejected ionic beam, while the remaining ones travel to the anode thanks to the axial electric field generated by potential difference between the anode and cathode.

Given that the standard operational pressure of these devices is in the order of mtorr, the electrons mean free path λ_e is too long to allow significant ionization from electron impact in a device with typical lengths in the centimetre/tens of centimetres range. In order to locally reduce the mean free path of electrons, a (mainly radial) stationary magnetic field is generated using DC coils or permanent magnets. The magnetic field peak intensity (typically in the range 100 G to 400 G is located in proximity of the channel exit. The maximum intensity of the magnetic field is chosen high enough to confine the electrons, while not perturbing the motion of the ions travelling from the anode to the cathode. Perpendicularly to the discharge current (which coincides with the direction of the electric field E), an electron drift is generated in the $\mathbf{E} \times \mathbf{B}$ direction, i.e., the azimuthal direction. This is also known as Hall current. The consequently generated electron azimuthal drift velocity is on the order of the ratio between the electric and magnetic field intensities:

$$v_{d,\theta} = \frac{\mathbf{E} \times \mathbf{B}}{B^2} \approx \frac{E_r}{B_z}, \tag{1.6}$$

where E_r and B_z are the radial electric field and axial magnetic field components, respectively. The expression for the azimuthal velocity holds provided that the electron collision frequency ν is small with respect to the electron angular cyclotron frequency [48], defined as:

$$\Omega_{ce} = \frac{eB}{m_e} \tag{1.7}$$

The electrons, injected from the cathode, are subjected to momentum-exchange collisions with the neutral gas and the channel walls. This allows the electrons to partially escape the magnetic confinement and progressively drift towards the anode. The resulting axial drift velocity can be expressed as:

$$v_{d,z} = -\frac{E}{B}\frac{\nu}{\Omega_{ce}}, \tag{1.8}$$

where ν is the electrons collision frequency.

Thanks to the presence of the radial magnetic field, increasing the residence time of the electrons inside the channel, the latter can ionize the neutral gas quite effectively. Indeed, ionization rates between 0.9 and 0.95 are achievable with this kind of devices. Another important consequence due to the presence of the radial magnetic field is that it leads to a strong local reduction of the plasma electrical conductivity (proportional to $1/B^2$ inside the thruster channel).

This lead, in turn, to a localized voltage drop, creating an intense electric field, with magnitudes in the range of tens of kV m. The strong electric field accelerates the ions, ultimately generating the thrust.

Following the path of the electrons injected from the external cathode and travelling towards the anode, three broad regions can be defined. The *acceleration* zone, located partly outside and inside the channel, corresponds with the high B region. In this zone, the mean energy of the electrons grows due to the presence of an intense electric field. Then, the acquired energy is partially lost to ionize the neutral gas propellant in the *ionization* zone, located upstream of the electric field maximum value. In this region, a highly collisional regime is granted due to the strong magnetic confinement. Finally, in the *anodic* region the electrons are no longer trapped by the magnetic field, and they their motion is driven by diffusion.

In this kind of thruster, the described ionization an acceleration zones overlap, causing dispersion in the ion velocity, and angular divergence in the ion beam resulting from the acceleration. Conversely, ion thrusters have a distinct ionization region in the plasma chamber, separated from the acceleration region by the grid. Hence, an ion thruster will produce a nearly mono-energetic beam, with lower angular divergence compared to its Hall counterpart.

2 Fluid model of an atmospheric pressure dielectric barrier discharge

Abstract

This chapter is concerned with the development of a fluid model for the numerical simulation of a barrier discharge (DBD) in high pressure conditions. In the following sections, the mathematical formulation adopted to assess the different physical phenomena taking place in this kind of discharges is described. In particular, two different methodologies for the assessment of the electron transport are presented and compared. Then, the discretization of the provided physical formulation is described, along with the employed numerical schemes.

2.1 Drift-diffusion approach

As already mentioned, this work consisted in the development of a fluid model, with the purpose of providing a physical description the main plasma dynamics and kinetic processes taking place in a dielectric barrier discharge. In order to ensure that such a macroscopic physical description applies to the particular kind of plasma under exam, two main assumptions must be verified.

The first fundamental hypothesis is that the physical system under exam behaves like a continuum, and not an ensemble of particles in molecular free-flow. This is found to be verified if the average distance travelled by charged particles without undergoing collisions is small compared to the characteristic length of the system under analysis. This condition is expressed by the Knudsen number, as detailed in Chapter 4.

The second hypothesis is that a partial local thermodynamic equilibrium (PLTE) is established between the considered charged species. This means that the electron and the ion populations are - singularly - at local thermodynamic equilibrium (LTE), but each specie is characterized by a different temperature ($T_e \neq T_i$) [49]. The LTE state of the considered species implies that, even if a global thermodynamic equilibrium state is not reached, the thermodynamic equilibrium (TE) is still valid locally. Hence, the velocity distribution function of the ionic and electronic species - in a given point in space - is described by a Maxwellian distribution function.

One of the main requirements of a dielectric barrier discharge (DBD) model is to adequately assess the dynamics of the different charged and neutral species of the gas under consideration. Let's consider the Boltzmann equation, describing the spatial and temporal evolution of the distribution function $f_s = f_s(\mathbf{r}, \mathbf{v}, t)$ for the particles of a given species s:

$$\frac{\partial f_s}{\partial t} + \mathbf{v} \cdot \nabla_{\mathbf{r}} f_s + \frac{\mathbf{F}}{m} \cdot \nabla_{\mathbf{v}} f_s = \left(\frac{\partial f_s}{\partial t} \right)_c , \tag{2.1}$$

The right hand side of the equation represents the contribution due to collisions. Integrating Eq. (5.1) over the velocity space, a conservation equation for the species s number density $n_s = n_s(\mathbf{r}, t)$ is obtained [50]:

$$\frac{\partial n_s}{\partial t} + \boldsymbol{\nabla} \cdot \boldsymbol{\Gamma}_s = \Omega_s, \tag{2.2}$$

where $\boldsymbol{\Gamma}_s = n_s \mathbf{u_s}$ represents the flux due to the mean velocity of the s species, $\mathbf{u_s}$. In the right-hand side of 2.2, Ω_s is the source term for s, and describes the rate at which particles are created or destroyed due to kinetic processes. The drift-diffusion approximation consists in expressing the flux $\boldsymbol{\Gamma}_s$ by means of two contributions, one due to the electric field (drift) and the other due to diffusion:

$$\boldsymbol{\Gamma}_s = \pm n_s \mu_s \mathbf{E} - D_s \nabla n_s. \tag{2.3}$$

Drift (or advection) is the transport of a scalar quantity due to the bulk motion of the fluid carrying the given quantity (in this case, the number density). Diffusion is the transport of the same scalar quantity due to the random motion induced by a concentration gradient. In Eq. (2.3), μ_s and D_s are the electrical mobility and diffusion coefficients for the species s. The aforementioned relation states that the flux of a species s, i.e., the particles flow rate per unit area, is caused by electric fields and gradients of density. The electric field $\mathbf{E}$ appearing in Eq. (2.3) is obtained using one of the two electrostatic formulations described in Sec. 2.2. Details on the derivation of the drift-diffusion expression for the flux $\mathbf{\Gamma}_s$ can be found in [2] and [51].

The diffusion and mobility coefficients appearing in Eq. (2.3) are related one to each other via the Einstein relation, as:

$$\frac{D}{\mu} = \frac{k_B T}{e}, \tag{2.4}$$

where e is the elementary charge, k the Boltzmann constant and T the temperature in K. Hence, for a given charged specie, the ratio of the diffusion coefficient to the electric mobility is proportional to the specie mean energy,

$$\epsilon = \frac{3}{2} k_B T \tag{2.5}$$

It should be noticed that, even if in principle the relation is valid for both ions and electrons, it is more accurate for the heavy species [52]. Nevertheless, this relation is employed for both electrons and ions in the developed model.

It is worth noticing that the drift-diffusion equation is a special case of the advection-diffusion equation, in which advection is caused due drift generated by the presence of an electric field. There are cases in which it is necessary to take into account a "true" advective term. This happens when the investigated gas is subject to a bulk flow, characterized by a mass velocity $\mathbf{U}$. In these cases, an advective term $n_s\mathbf{U}$ should be added to the above defined flux, giving:

$$\mathbf{\Gamma}_s = n_s(\mathbf{U} + \mu_s \mathbf{E}) - D_s \boldsymbol{\nabla} n_s \tag{2.6}$$

2.2 Electrostatics

2.2.1 Linear and nonlinear electrostatic formulations

The electric field $\mathbf{E}$ appearing in the Eq. (2.3) can be due to several physical phenomena. These include externally applied voltages, volumetric charge densities resulting from the spatial distribution of the charged species and surface charge densities accumulated on interfaces. Under the assumption of conservative electric field, the governing equation for the electric potential is given by Poisson's equation:

$$\boldsymbol{\nabla} \cdot (\epsilon_r \boldsymbol{\nabla} \varphi) = -\frac{\rho}{\epsilon_0}, \tag{2.7}$$

in which ϵ_0 is the vacuum's electrical permittivity and ϵ_r the relative electrical permittivity of the considered media. The volumetric charge density ρ at a given time instant is given by the distribution of the charged species number densities, as:

$$\rho = \sum_s q_s n_s, \tag{2.8}$$

where q_s is the elementary charge (with sign) associated with the specie s.

Alternatively to the above presented linear Poisson's equation of Eq. (2.7), a nonlinear version of the same relation is discussed and employed in this work. Indeed, considering that the dynamics of the electrons are much faster compared to the ions, one can assume that the electrons adapt instantaneously to the local value of the electric field.

The momentum transport equation for a given specie is the obtained as the first moment of the Boltzmann equation, by multiplying Eq. (5.1) by $\mathbf{u}$ and integrating over the velocity space:

$$mn\left[\frac{\partial \mathbf{u}}{\partial t} + (\mathbf{u} \cdot \nabla)\mathbf{u}\right] = qn(\mathbf{E} + \mathbf{u} \times \mathbf{B}) - \boldsymbol{\nabla} \cdot \mathbf{P} + \mathbf{f}\Big|_c . \tag{2.9}$$

The first (local) term of the substantial derivative on the left-hand side of Eq. (2.9) represents an acceleration due to time variations of $\mathbf{u}$, whereas the second (convective) term accounts for accelerations produced by spatial variations of the mean velocity $\mathbf{u}$. The right-hand side of Eq. (2.9) is constituted by force densities due to electric and magnetic fields, by the divergence of the pressure tensor and by collisions with other species, respectively.

The momentum equation for electrons in thermal equilibrium, in absence of electron drifts ($\mathbf{u}_e = 0$), inertial, magnetic and frictional forces can be written as: [50]:

$$en_e\mathbf{E} + \boldsymbol{\nabla} p_e = 0, \tag{2.10}$$

where p_e is the electron pressure. Setting $\mathbf{E} = -\boldsymbol{\nabla}\varphi$ and $p_e = nkT_e$ one obtains:

$$e\boldsymbol{\nabla}\varphi = \frac{kT_e}{n_e}\boldsymbol{\nabla}n_e. \tag{2.11}$$

The integration of the previous equation yields an expression for the electron number density as a function of the local electric potential φ, known as the Boltzmann relation:

$$n_e = n_{e,0}\exp\left(\frac{e(\varphi - \varphi_0)}{kT_e}\right), \tag{2.12}$$

where $n_{e,0}$ is the unperturbed electron number density, and φ_0 the reference electric potential. A more concise form of Eq. (2.12) can be obtained expressing the electron temperature in electronvolt:

$$n_e = n_{e,0}\exp\left(\frac{\varphi - \varphi_0}{T_{e,eV}}\right). \tag{2.13}$$

Substituting Eq. (2.13) into Eq. (2.7), a nonlinear Poisson problem is defined:

$$\boldsymbol{\nabla}\cdot(\epsilon_r\boldsymbol{\nabla}\varphi) = -\frac{1}{\epsilon_0}\left[\sum_{s\in H} q_s n_s - e n_{e,0}\exp\left(\frac{\varphi - \varphi_0}{T_{e,eV}}\right)\right]. \tag{2.14}$$

The first term in the right-hand side (RHS) of Eq. (2.14) represents the charge density due to the heavy species (H), i.e., the positive and negative ions. The remaining term of the RHS is the charge density contribution provided by the electrons, causing the nonlinearity of the problem. Details on the developed procedure for the numerical solution of Eq. (2.14) are provided in Sec. 2.4.3.

So far, two different electrostatic formulations have been presented. In the following section, the advantages of the two different approaches are discussed from the perspective of DBD modeling.

2.2.2 Linear and nonlinear electrostatic formulations comparison

In order to solve the linear Poisson problem (Eq. (2.7)) at a given time instant τ, the spatial number density distribution $n = n(\mathbf{r}, \tau)$ of both ions and electrons must be obtained at $t = \tau$. This task can be performed by solving the drift-diffusion equation (Eq. (2.2)) described in Sec 2.1 for all the considered charged species, including the electrons. This is a fairly common adopted approach in fluid models applied to both low and high-pressure non equilibrium discharges, including the considered dielectric barrier discharges [53–62]. The reason for the popularity of this approach is that it allows for a straightforward formulation and numerical solution of the electrostatic problem.

Nevertheless, as already mentioned, the high mass ratio between ions and electrons causes the dynamics of these two species to be very different one from each other. Hence, from the perspective of an explicit integration (subjected to a stability condition of the drift-diffusion equations, the employed time step must be small enough to follow the dynamics of the fastest species, i.e., the electrons. Because of this, it not unusual for the employed time-steps to be in the order of 1×10^{-12} s to 1×10^{-13} s. This fact does not constitute a major issue, as long as a drift-diffusion model is employed to study physical phenomena taking place in the range of nanoseconds or microseconds. A typical example of this is constituted by the study of streamer dynamics.

Conversely, the advantage provided by the adoption of the described nonlinear Poisson formulation Eq. (2.14) over the linear one is that, at a given time instant, the electron number density distribution is assumed to instantaneously adapt to the heavy species charge density distribution (and externally applied electric potentials) via the Boltzmann relation Eq. (2.13). This allows to omit the electrons from the drift-diffusion equations, with substantial beneficial effects in terms of achieved computational times. This is particularly convenient for 2D and 3D models, where the computational load can become a major issue. This is particularly relevant if one is interested in assessing the discharge physics for time lengths dictated by the external voltage supply.

2.2.3 Charge accumulation at dielectric interfaces

If a solid dielectric material is interposed between an electrode and the region where plasma is present (gap here onwards), a surface electric charge ρ_Σ may (and generally will) accumulate at the interface between the solid dielectric and the gap. A sketch of typical interface between a dielectric (characterized by $\epsilon_d > 1$) and a gas gap is reported in Fig. 2.1. In these cases, the electric field normal component experiences a discontinuity due to the surface charge [63], that can be expressed as:

$$\epsilon_{r,d} E_{\perp,d} - E_{\perp,gap} = \frac{\rho_\Sigma}{\epsilon_0}, \tag{2.15}$$

where $\epsilon_{r,d}$ is the relative dielectric permittivity. $E_{\perp,d}$ and $E_{\perp,gap}$ refer to the values

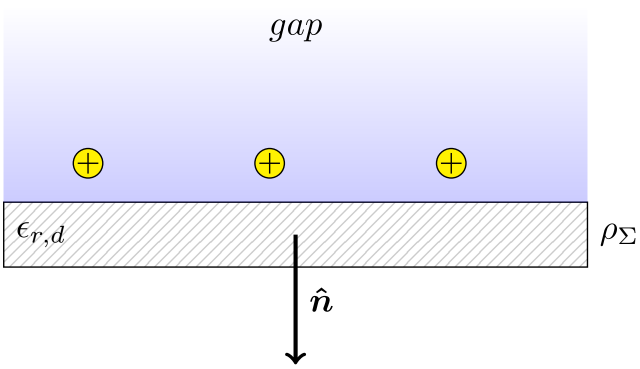

Figure 2.1: Sketch of a plasma-dielectric interface

of the electric field normal component at the two sides of the dielectric layer interface. This expression can be more conveniently formulated by means of the electric potential yielding:

$$\epsilon_{r,d} \left.\frac{\partial \varphi}{\partial n}\right|_{d} - \left.\frac{\partial \varphi}{\partial n}\right|_{gap} = -\frac{\rho_\Sigma}{\epsilon_0}, \tag{2.16}$$

where the subscript d and *gap* designate that the normal derivatives are computed in correspondence of the dielectric and gap sides of the discontinuity, respectively. In Eq. (2.16), the normal direction is assumed to be directed from the gap towards the dielectric surface.

The physical above described contributions due by the surface charge density are modelled in the same way whether the linear or nonlinear electrostatic formulation is employed. This is performed by including the surface charge density in the RHS of Poisson's equation, as detailed in Sec. 2.4.

2.3 Drift-diffusion equation finite volume discretization

The differential formulation of the conservation equation in Eq. (2.2) can also be expressed by means of an integral formulation. Considering a generic volume V, bounded by a closed surface ∂V with an outward pointing normal $\hat{\mathbf{n}}$, the integration of Eq. (2.2) yields the following expression:

$$\frac{dN_s}{dt} = \int_{\partial V} \mathbf{\Gamma}_s \cdot \hat{\mathbf{n}} dS + P_s. \tag{2.17}$$

The term on the left-hand side of Eq. (2.17) represents the time rate of change of the number of particles (of the species s) due to the fluxes and the source terms. This latter is defined as:

$$N_s = \int_V n_s dV. \tag{2.18}$$

The RHS of Eq. (2.17) comprises two terms:

1. $\int_{\partial V} \mathbf{\Gamma}_s \cdot \hat{\mathbf{n}} dS$, i.e., the number of particles of the species s that leave the volume V through its surface ∂V, per unit of time;
2. $P_s = \int_V \Omega_s dV.$, i.e., the number of particles of the species s produced (or eliminated) in the volume V by the kinetic processes, per unit of time.

Let's consider a generic bidimensional physical domain, discretized via a grid of nodes. Adopting a node centered approach, the generic volume V_i is represented in Fig. 2.2. A finite volume discrete formulation of the drift-diffusion equation can be obtained by applying the integral form of Eq. (2.17) to the generic control volume V_i. The following expression is therefore obtained:

$$\frac{dN_{s,i}}{dt} = - \sum_{A_p \in \partial V_i} \phi_{A_p}(\mathbf{\Gamma}_s) + P_{s,i}, \tag{2.19}$$

where the partial flux $\phi_{A_p}(\mathbf{\Gamma}_s)$ is the integral flux of $\mathbf{\Gamma}_s$ over the generic face A_p with belongs to the control volume boundary, defined as:

$$\phi_{A_p}(\mathbf{\Gamma}_s) = \int_{A_p} \mathbf{\Gamma}_s \cdot \mathbf{n} dS. \tag{2.20}$$

As one can see, the integral flux of $\mathbf{\Gamma}_s$ through the control volume boundary surface ∂V_i is expressed as the sum of the partial fluxes through the faces constituting ∂V_i. The number of particles of the species s in the control volume, $N_{s,i}$, is approximated assuming a uniform number density over the control volume:

$$N_{s,i} = \int_{V_i} n_s dV \approx n_{s,i} V_i. \tag{2.21}$$

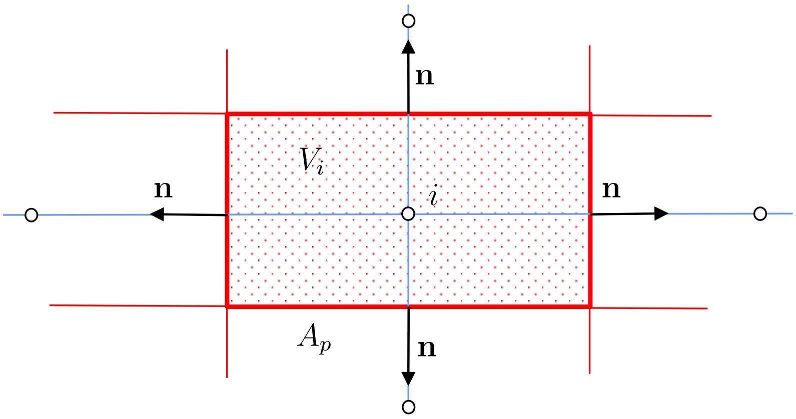

Figure 2.2: Generic node centered volume

The same approximation is adopted for the source term:

$$P_{s,i} = \int_{V_i} \Omega_s dV \approx \Omega_{s,i} V_i. \tag{2.22}$$

Hence, dividing Eq. (2.19) by the volume V_i, a finite volume expression for the number density conservation equation can be obtained:

$$\frac{dn_{s,i}}{dt} = -\frac{1}{V_i} \sum_{A_p \in \partial V_i} \phi_{A_p}(\mathbf{\Gamma}_s) + \Omega_{s,i}, \tag{2.23}$$

The following section is concerned with the numerical evaluation of the first term of the RHS of Eq. (2.23), i.e., the flux due to drift and diffusion. The evaluation process of the remaining two terms is described in Sec. 2.5 and Sec. 2.6, respectively.

2.3.1 Numerical flux evaluation

Let's consider a generic interface A_p between two adjacent mesh nodes i and j, as depicted in Fig. 2.3. The integral flux of $\mathbf{\Gamma}_s$ through A_p, can be split into a drift and a diffusion components:

$$\phi_{A_p}(\mathbf{\Gamma}_s) = \int_{A_p} \mathbf{\Gamma}_s dS = \int_{A_p} n_s \mu_s \mathbf{E} \cdot \mathbf{n} dS - \int_{A_p} D_s \nabla n_s \cdot \mathbf{n} dS \tag{2.24}$$

The diffusive flux is discretized using a centered differencing formula for the evaluation of the number density spatial derivative. Defining the partial integral flux due to diffusion as $\phi_{df,A_p}(\mathbf{\Gamma}_s)$, and $\tilde{\phi}_{df,A_p}(\mathbf{\Gamma}_s)$ as its (finite difference) approximated value, we have that:

$$-\int_{A_p} D_s \frac{\partial n_s}{\partial n} dS \approx \tilde{\phi}_{df,A_p}(\mathbf{\Gamma}_s) = \bar{D}_s \frac{n_{s,i} - n_{s,j}}{\Delta_{i,j}} A_p, \tag{2.25}$$

where $\Delta_{i,j}$ is the distance between the two considered adjacent nodes (depicted in Fig. 2.3), and $\bar{D}_s$ the average between D_i and D_j, the diffusion coefficients evaluated at nodes i and j.

For what concerns the drift flux, a centered differencing scheme is not applicable to this task, due to well known instability issues [64]. In this work, a first order upwind-differencing scheme is employed for the drift flux. In analogy to what has been performed for the diffusion flux, defining $\tilde{\phi}_{dr,A_p}(\mathbf{\Gamma}_s)$ as the approximated value of the partial integral flux due to advection,

$$\int_{A_p} n_s \mu_s E_n dS \approx \tilde{\phi}_{dr,A_p}(\mathbf{\Gamma}_s) = (n_{s,i} v_{s,+} + n_{s,j} v_{s,-})\, A_p, \tag{2.26}$$

where:

$$v_{s,+} = max(0, \mu_{s,i} E_n), \tag{2.27}$$

$$v_{s,-} = min(0, \mu_{s,j} E_n). \tag{2.28}$$

In Eq. (2.27) and Eq. (2.28), E_n denotes the electric field component perpendicular to the interface surface A_p, while $\mu_{s,i}$ and $mu_{s,j}$ are the values of electrical mobility for the specie s evaluated at nodes i and j. Finally, the total approximated integral flux is given by the sum of the obtained diffusive and drift contributions, as:

$$\tilde{\phi}_{A_p}(\mathbf{\Gamma}_s) = \tilde{\phi}_{df,A_p}(\mathbf{\Gamma}_s) + \tilde{\phi}_{dr,A_p}(\mathbf{\Gamma}_s) \tag{2.29}$$

2.4 Electrostatics finite volume discretization

The finite volume approach employed in the previous section for the approximated flux evaluation can be be utilized to discretize the governing equation for electrostatics.

An integral formulation for the electrostatic problem can be derived starting from the

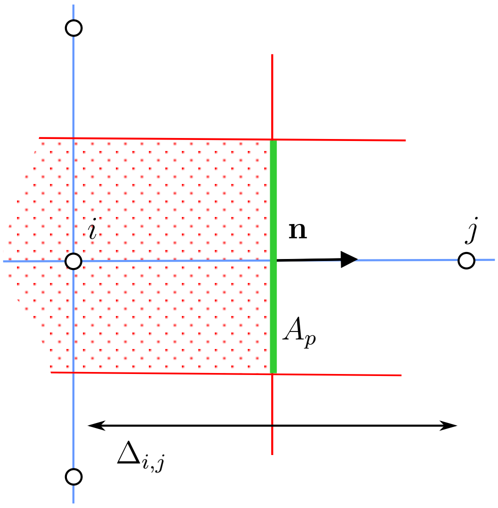

Figure 2.3: Interface between two mesh nodes

Gauss law in terms of the electric displacement field $\mathbf{D}$:

$$\nabla \cdot \mathbf{D} = \rho, \tag{2.30}$$

and integrating it over a generic volume V. Applying the divergence theorem to the left-hand side of Eq. (2.30), the resulting expression is:

$$\int_{\partial V} \mathbf{D} \cdot \mathbf{n} dS = \int_V \rho dV \tag{2.31}$$

where ∂V is the closed surface bounding the volume V in which the charge density ρ is contained.

With reference to the generic control volume V_i in Fig. 2.2 the total integral flux of the electric displacement vector can be expressed as the sum of the partial fluxes through the interfaces constituting the bounding surface ∂V_i:

$$\frac{1}{V_i} \sum_{A_p \in \partial V_i} \phi_{A_p}(\mathbf{D}) = \sum_s q_s n_{s,i} \tag{2.32}$$

Considering now a generic interface with area A_p between two nodes i and j such as the one depicted in Fig. 2.3, the (approximated) discrete expression of the integral flux

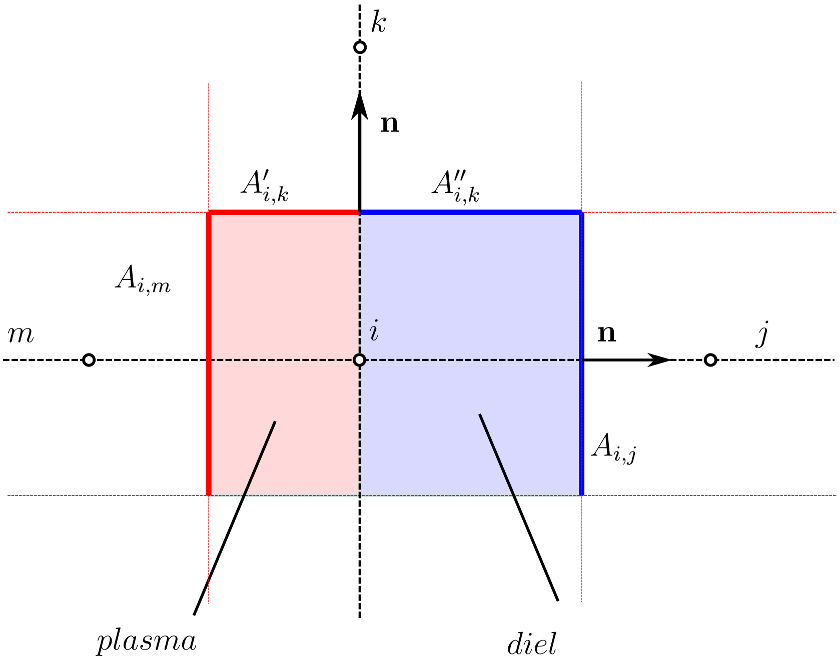

Figure 2.4: Control volume shared between plasma and dielectric

becomes:

$$\phi_{A_p}(\mathbf{D}) = \int_{A_p} \epsilon \frac{\partial \phi}{\partial n} dS \approx \tilde{\phi}_{A_p}(\mathbf{D}) = -\epsilon \frac{\phi_j - \phi_i}{\Delta_{i,j}} A_p, \tag{2.33}$$

where $\mathbf{D}$ has been expressed as $-\epsilon \nabla \phi$ as a result of the hypothesis of conservative field[1].

2.4.1 Interface between two materials

Let's consider the particular case depicted in Fig. 2.4, where the node i lies on the interface between the plasma (with permittivity ϵ_0) and another material (for instance, a dielectric layer with relative permittivity $\epsilon_{r,d}$).

With reference to Fig. 2.4, the electric displacement vector flux through faces entirely within the plasma or the dielectric (such as $A_{i,m}$ and $A_{i,j}$) is computed using the expression in Eq. (2.33) with the appropriate electric permittivity value, yielding:

$$\tilde{\phi}_{A_{i,m}}(\mathbf{D}) = -\epsilon_0 \frac{\phi_m - \phi_i}{\Delta_{m,i}} A_{i,m}, \tag{2.34}$$

---

[1] This assumption is justified as the electric currents are not strong enough to produce a time varying magnetic field capable of affecting the electric field through $\nabla \times \mathbf{E} = \frac{-\partial B}{\partial t}$.

for the interface entirely contained in the plasma domain, and:

$$\tilde{\phi}_{A_{i,j}}(\mathbf{D}) = -\epsilon_d \frac{\phi_j - \phi_i}{\Delta_{i,j}} A_{i,j}, \tag{2.35}$$

for the interface entirely contained in the dielectric domain.

The interface $A_{i,k}$ is shared between the plasma region and the dielectric. Thanks to the linearity of the problem, the approximated electric displacement flux can be expressed as:

$$\tilde{\phi}_{A_{i,k}}(\mathbf{D}) = -\frac{\phi_j - \phi_i}{\Delta_{i,k}} (\epsilon_0 A'_{i,k} + \epsilon_d A''_{i,k}). \tag{2.36}$$

2.4.2 Algebraic system for electrostatics

Following the finite volume approach described in the previous section, an equation is written for each interface expressing the integral electric displacement flux. Hence, the equation for each node is obtained by summing the partial fluxes through the interfaces bounding its control volume, as indicated in Eq. (2.32). The sum of the these fluxes is equal to the net electric charge contained in the same control volume.

After assembling the equations for all the mesh nodes into a coefficient matrix $[K]$, an algebraic system is obtained, that can be used to obtain the stationary electric potential at every node due to the charged carriers (and the boundary conditions):

$$[K]\{\phi\} = \{RHS\}. \tag{2.37}$$

The coefficient matrix $[K]$ is sparse, with at most 5 non-zero coefficients for each row in a 2D implementation, and 3 non-zero coefficients if a 1D domain is considered.

As already mentioned, the system in Eq. (2.37) is time independent. The time-varying behavior of the physical system is driven by the drift-diffusion equations, and (at least if an explicit time integration approach is adopted) the described algebraic system must be solved at each time iteration of the drift-diffusion equations. The rationale behind solving the Poisson equation independently from the plasma kinetics lies in the marked difference between the characteristic times scales of the electric power sources and the dynamics of the charge carriers [54]. If, for example, a DBD device is driven by a 15 kHz

AC voltage, the period of the applied sinusoidal waveform is:

$$T_{AC} = \frac{1}{15 \times 10^3} = 6.67 \times 10^{-5}\,\mathrm{s}. \tag{2.38}$$

The electric response of the charged species to electric forces (such as the AC power itself) can be characterized by the drift velocity, expressed as:

$$v_d = \mu E \tag{2.39}$$

Let's consider a DBD device with a 1 mm gap, powered by a 5 kV sinusoidal voltage source with frequency $f_{AC} = 15\,\mathrm{kHz}$. Assuming a linear potential drop over the gap, the obtained electric field driving the charge carriers is $E = 5 \times 10^6\,\mathrm{Vm^{-1}}$. Then, assuming that $\mu_{el} = 0.7\,\mathrm{m^2\,s^{-1}\,V^{-1}}$, $v_d = 3.5 \times 10^5\,\mathrm{m\,s^{-1}}$. Hence, the time τ_d required for an electron to drift from one side to the other of the gap due the electric field E is:

$$\tau_d = \frac{L_{gap}}{v_d} = 2.86 \times 10^{-9}\,\mathrm{s} \ll T_{AC}. \tag{2.40}$$

As one can, see, τ_d is considerably smaller than T_{AC}. For this reason, it can be assumed that the charge carriers (in particular electrons, due to their higher electric mobility) react instantaneously to externally supplied voltages, and the physical effects of the electrostatics can be accounted separately from the charged particles motion and generation.

Provided that all the number density are known at a generic time (i.e., the drift-diffusion equations are solved for both the heavy species and the electrons), the algebraic system is linear, and its solution provides the distribution of the electric potential and of the electric field over the calculation domain.

2.4.3 Nonlinear Poisson equation solution

In this section, the main features of the procedure developed solve the nonlinear Poisson problem are discussed. Therefore, let's consider the nonlinear Poisson equation, derived in Sec. 2.2:

$$\boldsymbol{\nabla} \cdot (\epsilon_r \boldsymbol{\nabla} \varphi) = -\frac{1}{\epsilon_0}\left[\rho_{ion} - e n_{e,0} \exp\left(\frac{\varphi - \varphi_0}{T_{e,eV}}\right)\right]. \tag{2.41}$$

The heavy species charge density is computed on the generic grid node k as:

$$\rho_{i,k} = \sum_s n_s q_s, \tag{2.42}$$

where s and q_s refer to the generic ionic species and its electric charge, respectively.

The initial net electric charge (due to the heavy species) contained in the discretized domain (the gap and the j considered dielectrics layers) is evaluated as:

$$Q_0 = \sum_k \rho_{i,k} V_k + \sum_j Q_{\Sigma,j}, \tag{2.43}$$

where V_k is the $k-$th node volume, and $Q_{\Sigma,j}$ the charge stored in the $j-$th dielectric layer. $Q_{\Sigma,j}$ is evaluated as:

$$Q_{\Sigma,j} = \rho_{\Sigma,j} S_d, \tag{2.44}$$

where $\rho_{\Sigma,j}$ is the charge density obtained from the charged species flux, and S_d dielectric layer area. This preliminary evaluation is carried out to verify if the sum of the charge due to heavy species and to surfaces is positive. As will subsequently be clarified, this is a necessary condition for the procedure used to determine the electric potential.

Once Q_0 in Eq. (2.43) has been verified to be positive, the background electron number density $n_{e,0}$ is computed as:

$$n_{e,0} = \frac{Q_0}{q_e V}, \tag{2.45}$$

where V is the total volume of the gap and Q_0 has been defined in Eq. (2.43).

The numerical solution of the nonlinear Poisson equation (2.41) can be obtained using the well-known Newton-Raphson algorithm. As an example, Fig. 2.5 shows the electric potential distribution and electron number density obtained on a 2.5 mm domain, with a uniform number density of ions ($n_i = 1 \times 10^{16}\,\mathrm{m}^{-3}$) when Dirichlet boundary conditions ($\phi_1 = 5\,\mathrm{V}$, $\phi_n = -5\,\mathrm{V}$) are enforced at the two ends of the domain.

The Newton-Raphson method has an iterative nature. Hence, it requires a starting electric potential distribution φ^*, in order to evaluate the initial electron contribution to the charge density. The first tentative value of φ^* is estimated by solving a linear Poisson problem, with the electron number density set to the obtained value $n_{e,0}$. This

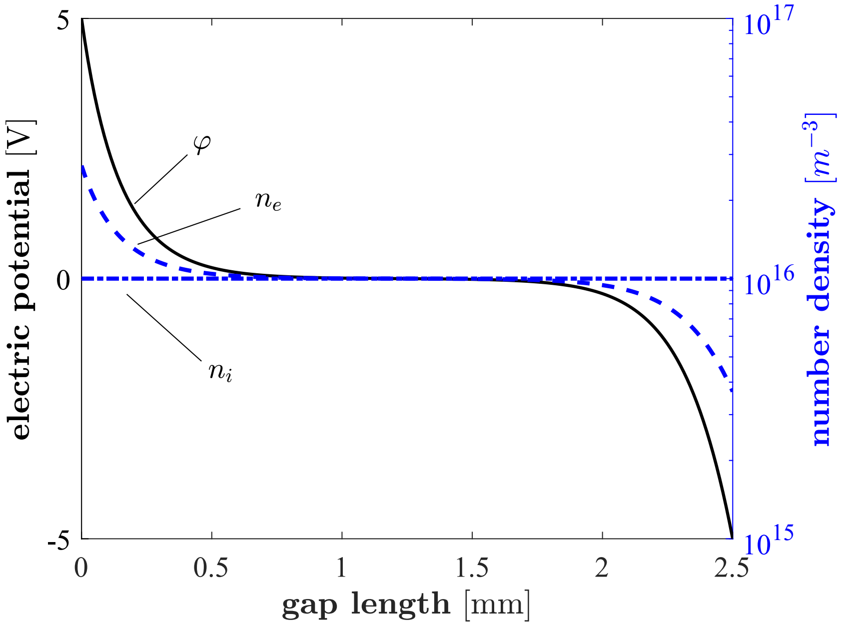

Figure 2.5: Electric potential, charge density, and electronic number densities over a 5 mm domain, obtained from the nonlinear Poisson problem solution with uniform density of ions, $\phi_0 = 0\,\mathrm{V}$ and $\phi_1 = 5\,\mathrm{V}$, $\phi_n = -5\,\mathrm{V}$

choice has proven to reduce the number of iterations of the Newton-Raphson algorithm, compared to when a null starting potential is employed.

Global electric charge conservation

At this point it worth highlighting that, so far, the presented nonlinear Poisson problem does not imply the conservation of the electric charge in the considered domain. Indeed, there is no guarantee that the total negative charge provided by the electrons – found by solving the nonlinear electrostatic formulation – is neutralized by the volume and surface charges due to the ions and the dielectric layers, respectively. In comparison, this condition is automatically satisfied when the drift-diffusion approach is extended to the electrons and a linear Poisson problem is solved at each iteration.

In order to preserve the charge neutrality condition when solving the nonlinear Poisson problem, the charge conservation is added as a constraint of the nonlinear problem. For a given value of the reference electric potential φ_0, Eq. (2.41) yields a spatial distribution of electrons, that can be added to the net charge due to the ions and surface charge

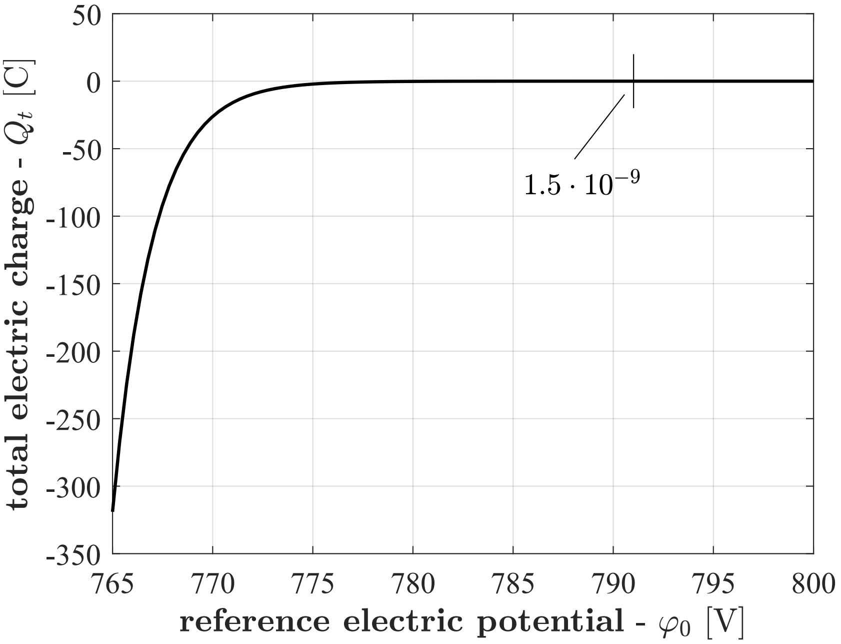

Figure 2.6: Total electric charge dependence from the employed reference electric potential; The minimum value of Q_t, corresponding to the required charge neutrality condition, is pointed out

distributions defined in Eq. (2.43):

$$Q_t = Q_0 - \sum_k \rho_{e,k} V_k, \tag{2.46}$$

where V_k is the $k-$th nodal volume, and the nodal charge density due to electrons. In this way, the reference electric potential φ_0 is regarded as a free parameter, employed to satisfy the desired electric neutrality condition, corresponding to $Q_t = 0$.

This problem, i.e., finding a reference electric potential value φ_0^* that leads to a solution of Eq. (2.41) which satisfies the electric neutrality, is once again nonlinear. The most straightforward approach could seem to include the condition $Q_t = 0$ as an additional equation the Newton-Raphson algorithm. Indeed, the quadratic convergence rate of this algorithm makes it one of the fastest ways to solve a generic nonlinear problem. However, the dependence of Q_t form φ_0 makes the Newton-Raphson rather unsuited to tackle the considered numerical problem. To clarify this, Fig. 2.6 shows the total electric charge (Q_t) as a function of φ_0 when 800 V are applied between the two ends of the considered domain. Except for the applied voltage, the other physical parameters are the same as in the example shown in Fig. 2.5. The Newton-Raphson method is notoriously unsuited to solve problems where the unknown function exhibits near-zero or very steep slopes. The example physical example depicted in Fig. 2.5 features both these two critical situations, above and below the zero of the unknown function Q_t.

For this reason, instead of including the $Q_t = 0$ condition in the Newton-Raphson algorithm employed to solve the electrostatic nonlinear formulation, an iterative procedure based on the bisection method has been developed to solve the described problem robustly. The bisection method, while being significantly slower than the Newton-Raphson algorithm, is unconditionally stable provided that appropriate initial conditions are provided. Indeed, in order to employ the bisection method, two initial values of φ_0 must be provided. These $\varphi_{0,+}$ and $\varphi_{0,-}$ must yield – once used as reference potential in the nonlinear Poisson equation – a positive and negative value for Q_t, respectively.

Algorithm 1: Nonlinear poisson solver with global charge conservation

```
$\varphi_{0,+}$ such that $Q_{t,\varphi_{0,+}} > 0$
$\varphi_{0,-}$ such that $Q_{t,\varphi_{0,-}} < 0$
while $Q_{t,\phi_0} > Q_{tol}$ do
    $\varphi_0^* = \frac{\varphi_{0,+} - \varphi_{0,-}}{2}$
    Solve nonlinear Poisson for $\varphi_0^*$ (NR algorithm)
    Evaluate $Q_{t,\varphi_0^*}$
    if $Q_{t,\phi_0^*} > 0$ then
        $\varphi_{0,+} = \varphi_0$
    else
        $\varphi_{0,-} = \varphi_0$
    end
end
```

The adopted procedure based on the bisection method is reported in pseudo-code in Algorithm 1. Starting from $\varphi_{0,+}$ and $\varphi_{0,-}$, a tentative reference potential φ_0^* is obtained as the midpoint of the interval $[\varphi_{0,-}; \varphi_{0,+}]$. Then, the resulting nonlinear Poisson problem is solved (using φ_0^* as the reference electric potential) using the Newton-Raphson algorithm. The resulting electron distribution yields a total electric charge Q_{t,φ_0^*}. If $Q_{t,\varphi_0^*} > 0$, the φ_0^* becomes the value of $\varphi_{0,+}$ that will be employed at the next iteration of the cycle. Otherwise, if $Q_{t,\varphi_0^*} < 0$, φ_0^* is employed as $\varphi_{0,-}$. The cycle carries on until $\left|Q_{t,\varphi_0^*}\right|$ is lower than the requested tolerance.

Algorithm 2: Prescan - iterative search of reference electric potential

```
Solve linear Poisson $[K]\{\varphi^*\} = (\rho_{ion} - q_e n_{e,0})/\epsilon_0$ to get $\varphi^*$
$\varphi_0 = \varphi_{0,-} = \varphi_{0,+} = \max(\varphi^*)$ ; $\Delta\phi = T_{eV}/5$
Solve NL Poisson
if $Q_{t,\varphi_0} > 0$ then
    while $Q_{t,\varphi_0} > 0$ do
        $\varphi_{0,-} = \varphi_{0,-} - \Delta\varphi$
        Solve NL Poisson
    end
else
    while $Q_{t,\varphi_0} < 0$ do
        $\varphi_{0,+} = \varphi_{0,+} + \Delta\varphi$
        Solve NL Poisson
    end
end
```

Algorithm 2 shows the procedure adopted to obtain the aforementioned starting values for the bisection method, i.e, $\varphi_{0,+}$ and $\varphi_{0,-}$, in pseudo-code. As previously described, in order to provide a starting electric potential distribution (φ^*) for the Newton-Raphson solver, a linear Poisson problem is solved assuming a uniform distribution of the electrons. Then, using φ^* as a starting point, the nonlinear Poisson problem is solved once by setting φ_0 as the maximum value of the previously obtained φ^*. Then, the obtained value of total electric charge Q_{t,φ_0} is compared to zero. If $Q_{t,\varphi_0} > 0$ it means that φ_0 can be used as $\varphi_{0,+}$ for the subsequent bisection cycle, and a value of φ_0 that yields $Q_t < 0$ must be found iteratively. This is performed by progressively lowering φ_0, in steps corresponding to $T_{ev}/5$, where T_{ev} is the electron temperature in electronvolt. The cycle continues until $Q_t < 0$ is obtained, meaning that the employed φ_0 can be used as $\varphi_{0,-}$ in the bisection cycle. Conversely, if the starting value of Q_t is negative, the value of φ_0 yielding a positive Q_t, i.e., $\varphi_{0,+}$, is iteratively found by increasing φ_0 in steps of $T_{ev}/5$.

2.5 Time discretization

This section is concerned with the numerical methodologies employed for the time discretization of the system of differential equations obtained from writing the discrete balance equation Eq. (2.19) for each considered species s. The expression is reported here for the reader's convenience:

$$\frac{dn_{s,i}}{dt} = -\frac{1}{V_i} \sum_{A_p \in \partial V_i} \phi_{A_p}(\mathbf{\Gamma}_s) + \Omega_{s,i}, \tag{2.47}$$

The resulting s equations are coupled, as the electric field driving the drift term of the flux depends from the charge density. In general, two distinct methodologies can be employed to perform a time discretization from the generic time instant $t^{(k)}$ to $t^{(k+1)}$:

- Explicit schemes, where variables at time $t^{(k+1)}$ are evaluated through a direct expression, only using the known values at the preceding instant $t^{(k)}$;
- Implicit schemes, where variables at time $t^{(k+1)}$ are evaluated through a system of equations, where both variables at time instant $t^{(k+1)}$ and $t^{(k)}$ are present.

In this work, an explicit approach was adopted due to two main reasons. First of all, it allows a more straightforward implementation with respect to implicit approaches. Moreover, adopting an explicit approach means that the flux discretization, electric field computation and integration of source terms can be performed independently. This allows experimenting with different methodologies for these three tasks with more freedom.

The number density time derivative in the left hand side of Eq. (2.47) can be expressed through a forward finite difference:

$$\left.\frac{dn_{s,i}}{dt}\right|^{(k)} \approx \frac{n_{s,i}^{(k+1)} - n_{s,i}^{(k)}}{\Delta t^{(k)}}. \tag{2.48}$$

Consequently, the number density of the given species s can be obtained at time instant $t^{(k+1)}$ using an Euler explicit scheme.

$$n_{s,i}^{(k+1)} = n_{s,i}^{(k)} - \frac{\Delta t^{(k)}}{V_i} \sum_{A_p \in \partial V_i} \tilde{\phi}_{A_p}(\mathbf{\Gamma_s}^{(k)}) + \Omega_{s,i}^{(k)} \Delta t^{(k)}. \tag{2.49}$$

In order to grant the numerical stability of the Euler integrator, the time step $\Delta t^{(k)}$ to be employed to time-march from time instant $t^{(k)}$ to $t^{(k+1)}$ is obtained by evaluating the Courant-Friedrichs-Lewy (CFL) condition [65] for each species:

$$\Delta t < min \left[\frac{1}{|\mu_s E/\Delta + |D_s/(2\Delta^2)|} \right], \tag{2.50}$$

with:

$$\Delta = min\left(\Delta_x, \Delta_y\right).$$

The Δ symbol in Eq. (2.50) represent the minimum grid spacing along both dimensions of a generic 2D grid.

2.6 Source terms integration

The CFL stability condition is computed accounting for the convective and diffusive terms of Eq. (2.49). Nevertheless the equation also features a source term due to elementary processes, representing the rate per unit volume at which the particles vary due to the reactions that take place in the plasma.

Source and loss terms due to elementary processes are usually expressed as the product of a rate coefficient multiplied by the number densities of the reactants involved in the process itself. Hence, differently from the diffusive and advective contributions, the analytical expression of the source terms depend on the considered reactions. The *stable* time step $\Delta t^{(k)}$ obtained with the CFL condition has been derived assuming a homogeneous equation, and does not account for the source terms.

In other words, the stability of the method is not guaranteed with respect to the time integration of the source terms. As a matter of fact, the dynamics of the source terms can be very rapid and, if not treated properly, can negatively affect the stability of the solver. For each mesh node, the number density changes due to the source terms in a generic time step $\Delta t^{(k)}$ are computed by employing the semi-implicit approach introduced in [66]. Linearising the source term time behavior at the generic node i, one may write:

$$\boldsymbol{\Omega}_i(t) = \boldsymbol{\Omega}_i^{(k)} + \left[J_i^{(k)}\right] \Delta\mathbf{n}_i(t), \tag{2.51}$$

where $\boldsymbol{\Omega}_i$ indicates the array of the source terms for the considered species at node i. $\left[J_i^{(k)}\right]$ is the local Jacobian matrix of the source terms, evaluated at the $k-$th time instant. The entries of $\left[J_i^{(k)}\right]$ are the derivatives of source terms with respect to the species number densities. The nodal density variation array $\Delta\mathbf{n}_i^{(k)}$ is then found integrating $\boldsymbol{\Omega}_i(t)$ over time and applying the trapezoidal rule:

$$\Delta\mathbf{n}_i^{(k)} = \int_{t^{(k)}}^{t^{(k+1)}} \boldsymbol{\Omega}_i(t) \approx \frac{\boldsymbol{\Omega}_i^{(k)} + \boldsymbol{\Omega}_i^{(k+1)}}{2} \Delta t^{(k)}. \tag{2.52}$$

Then, using Eq. (2.51) to express $\boldsymbol{\Omega}_i^{(k+1)}$, the following expression is obtained:

$$\Delta\mathbf{n}_i^{(k)} = \boldsymbol{\Omega}_i^{(k)} \Delta t^{(k)} + \frac{1}{2}\left[J_i^{(k)}\right] \Delta\mathbf{n}_i^{(k)} \Delta t^{(k)}. \tag{2.53}$$

Rearranging, one obtains an algebraic linear system (the rank of the system is given by the number of considered species) that yields the number density variation at each node due to the reactions $\Delta\mathbf{n}_i^{(k)}$:

$$\left([I] - \frac{1}{2}\left[J_i^{(k)}\right]\right) \Delta\mathbf{n}_i^{(k)} = \boldsymbol{\Omega}_i^{(k)} \Delta t^{(k)}, \tag{2.54}$$

where $[I]$ is the identity matrix.

The Euclidean norm of the matrix $[I] - \frac{1}{2}\left[J_i^{(k)}\right]$ in Eq. (2.54) is checked at the $k-$th time instant using the $\Delta t^{(k)}$ yielded by the CFL condition of Eq. (2.50). The required stability condition is expressed as:

$$\left|\left|\frac{1}{2}\left[J_i^{(k)}\right]\right|\right| < \beta_k, \tag{2.55}$$

with $\beta_k = 0.01$.

If the condition expressed in Eq. (2.55) is not satisfied, the semi-implicit integration is split in the minimum required number of sub-steps to cover $\Delta t^{(k)}$ while still satisfying the aforementioned β_k. The process is schematized in Fig. 2.7, where the sub-cycling of the

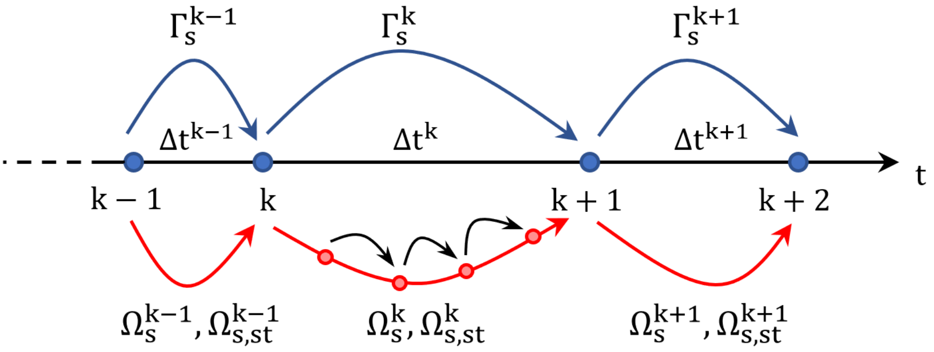

Figure 2.7: Sub-cycling of the semi-implicit solver employed to perform the time-integration of the plasma kinetics source terms

semi-implicit integration is represented against the time steps used in the drift-diffusion integration, yielded by the CFL stability condition.

3 Simulation Results

In this chapter, the results obtained from the numerical simulation of an atmospheric pressure air volumetric DBD reactor are presented. The first part of the chapter is devoted to the description of the developed computer code, based on the theoretical approach discussed in Chapter 2. The developed numerical tool has been used to obtain the presented results. Subsequently, the geometry and the physical properties of the modelled physical configuration are described. Then, the modelling results are discussed, and compared to experimental measurements. Finally, the results and the code performances obtained by including the electrons in the drift-diffusion approach are compared to the ones yielded by the developed alternative description, where the spatial distribution of the electrons is computed using the Boltzmann relation.

3.1 Numerical code description

The developed code can operate with either one or two physical dimensions, and has been implemented in two different programming languages, i.e., MATLAB®and FORTRAN 90. These two languages have been selected for their rather complementary nature, the first being interpreted and the second compiled. The MATLAB®implementation has been employed for the prototyping and code verification. Conversely, the FORTRAN 90 implementation benefits from the execution speeds achievable thanks to the optimization performed at compiler time [67]. Moreover, FORTRAN 90 supports both shared memory and distributed memory parallel communication protocols, such as OpenMP and MPI. While explicit multi-core processing is supported in MATLAB®through the Parallel Computing Toolbox [68], the aforementioned tools available using the FORTRAN language offer more flexibility and higher performances.

In the following sections, the fundamental features of the developed code are described. Notable differences between the MATLAB®and FORTRAN 90 implementations are

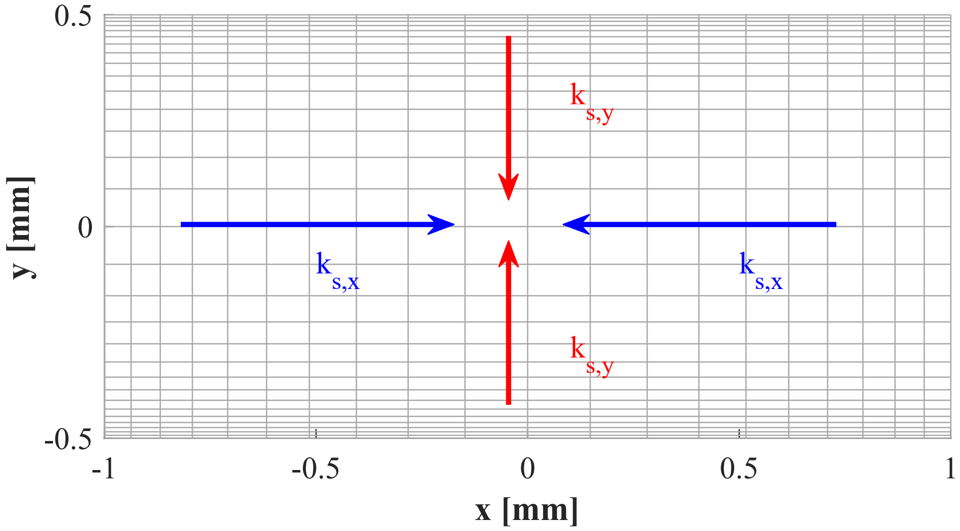

Figure 3.1: Example of a 2D regular non-uniform grid, with a refinement of the spacing towards the boundaries of the discretised domain

pointed out when necessary.

3.1.1 Mesh generation

According to the selected number of nodes and dimensionality, a 1D/2D grid is generated to perform a spatial discretization of the considered domain. The employed grid can either be uniform or non-uniform. In the second case, the grid spacing along the x and y directions is specified by defining – for each direction – the ratio between the length of the given cell k and the next one, $k+1$. In this way, considering e.g. the x direction, $k_{s,x}$ is defined by the following expression:

$$k_{s,x} = \frac{\Delta x_{k+1}}{\Delta x_k}. \tag{3.1}$$

Figure 3.1 shows an example of a non-uniform grid generated by the developed code, with 21 and 31 nodes along the x and y directions, respectively. For the represented example, $k_{s,x}$ and $k_{s,y} = 1.2$ have been set to 1.1 and 1.2, respectively. Although negative values for $k_{s,x}$ and $k_{s,y}$ are permitted, these would yield a finer grid spacing in the internal part of the mesh. However, considering the specific case of DBD modelling, the highest values of number density are usually found at the edges of the domain, where the different species tend to accumulate as a consequence of the drift induced by the externally applied electric field. The grid spacing is subjected to the requirement of resolving the Debye length:

$$\lambda_d = \sqrt{\frac{\epsilon_0 K_B T_e}{n_e q_e^2}}, \tag{3.2}$$

where ϵ_0 is the vacuum dielectric permittivity, K_B the Boltzmann constant, T_e the electron temperature, n_e the electron density and q_e the elementary charge. Hence, the maximum expected electron density constitutes a criteria for the local grid spacing required for the numerical stability of the numerical model. Since the aforementioned maximum number density is expected to be located at the domain boundaries, the employment of a non-uniform grid spacing allows to meet the minimum spatial resolution defined by Eq. (3.2), while contextually keeping a reasonable number of grid nodes.

The described procedure represents a simpler alternative to more sophisticated approaches based on adaptive mesh refinement (AMR), where the spatial distribution of the grid nodes is dynamically adapted to increase the grid density where the physical properties change sharply and vice versa [69]. In the field of DBD modelling, different variations of this technique have led to performance improvements in several works employing both structured [70, 71] and non-structured meshes [8, 72].

3.1.2 Species initial distribution

Once the computational grid has been generated, a module containing the physical information on the considered gas is loaded. At the present stage, the code can be operated in either atmospheric pressure air or pure helium. However, since the present study focuses on the DBD in atmospheric pressure air, only the *AIR* module will be described in this section.

The heavy species accounted in the drift-diffusion model are $N_2{}^+$, $O_2{}^+$, $O_2{}^-$, O, O^- and O_3. Clearly, the flux density $\mathbf{\Gamma}$ for the neutral species in the above list is only due to diffusion. For what concerns the electrons, these may or may not be included in the drift-diffusion equations, depending on the electron model chosen by the user. Indeed, as introduced in Chapter 2, instead of including the electrons in the drift-diffusion approach the Boltzmann relation (coupled with the Poisson equation for electrostatics) can be employed to obtain the electron spatial distribution.

Table 3.1: Electrical mobility coefficients for ions and electrons in dry air, from [5]; N is the background neutrals density $[\mathrm{m}^{-3}]$, T the heavy ions temperature [K] and T_e the electron temperature [K]

Species	**Mobility** $[\mathrm{m\,V^{-2}\,s^{-1}}]$	**Reference**
$N_2{}^+$	$N^{-1}\min\left(0.84\times10^{23}T^{-1/2}, 2.35\times10^{12}\left(\frac{E}{N}\right)^{-1/2}\right)$	[73]
$O_2{}^+$	$N^{-1}\min\left(0.75\times10^{23}T^{-1/2}, 2.03\times10^{12}\left(\frac{E}{N}\right)^{-1/2}\right)$	[73]
$O_2{}^-$	$N^{-1}\min\left(1.18\times10^{23}T^{-1/2}, 3.61\times10^{12}\left(\frac{E}{N}\right)^{-1/2}\right)$	[74]
e^-	$N^{-1}3.74\times10^{19}\exp\left(33.5\ln(T_e)^{-1/2}\right)$	[75]

Once the operating gas has been selected, an initial number density value for each species is assigned to the generated grid nodes. For the $k-$th considered specie, the initial number density distribution in the gap can be either uniform or Gaussian. In both cases, the initial ratio between $N_2{}^+$ and $O_2{}^+$ is set to $3:1$. The $O_2{}^-$ is set to a $1:8$ ratio with respect to $N_2{}^+$ and the electron density is selected as to ensure the overall electric neutrality. The physical influence of the initial ionization degree and ratios between the charged species will be discussed quantitatively in Sec. 3.4.4.

3.1.3 Macroscopic transport parameters

The electrical mobility of $N_2{}^+$, $O_2{}^+$, $O_2{}^-$ and e^- is computed using the expressions in [5]. These are reported in Table 3.1 for the reader's convenience, along with the associated original reference. The variable N in the expressions represents the background neutrals density, expressed in m^{-3} while T and T_e are the ionic and electronic temperatures in Kelvin.

The electrical mobility coefficient values are plotted as a function of the electric field (from 10×10^{-3} Td to 5×10^{2} Td) in Fig. 3.2a, assuming that $T = 400\,\mathrm{K}$ and $T_e = 2\,\mathrm{eV}$. As expected, the electrons show considerably higher electrical mobility values throughout the whole considered range of applied electric field. This leads to the correspondingly higher drift velocities shown in Fig. 3.2b.

Once the mobility coefficient is obtained with the above described procedure, the diffusion coefficient is derived from the Einstein relation:

$$\frac{D}{\mu} = \frac{k_B T}{e}, \tag{3.3}$$

where e is the elementary charge, k_B the Boltzmann constant and T the temperature in K.

3.1.4 Drift-diffusion fluxes integration

The macroscopic transport parameters obtained with the procedure described in Sec. 3.1.3 are employed to compute the number density (integral) fluxes in the continuity equation, i.e., Eq. (5.5).

Whether the code operates in one or two dimensions, the species number densities are stored in a single 2D array, where each column correspond to a different species. A single array is employed for the storage of all the considered species, because it allows the vectorization of the fluxes integration. In both MATLAB®and FORTRAN languages, vectorized operations are automatically distributed among the available CPU threads by the compiler, and – in general – offer substantial time savings over explicit iteration constructs. The choice of using the rows (instead of the columns) of the employed 2D array to store the nodal number density of a given specie is due to the column-wise nature of both employed languages [67]. Indeed, the number of species is largely inferior to the number of employed grid nodes, and the integration of the fluxes does not involve and dependence between nodal values of different species. Hence, devoting each column to a different specie maximizes the data contiguity. The above reasoning also applies to the species velocity.

The temporal and spatial discretization process of the continuity equation (expressed in drift-diffusion form) for the number density has been described in Chapter 2. In the developed code, the described numerical procedures are applied to a dimensionless version of the drift and diffusion equation. The latter is reported here in its dimensional form for the reader's convenience:

$$\frac{\partial n}{\partial t} = \boldsymbol{\nabla} \cdot (D \boldsymbol{\nabla} n) - \boldsymbol{\nabla} \cdot (n\mathbf{u}) + \Omega, \tag{3.4}$$

where $\mathbf{u} = \mu\mathbf{E}$ is the drift velocity due to the electric field. In order to obtain a dimensionless version of Eq. (3.4) , some *reference* quantities must be defined. These

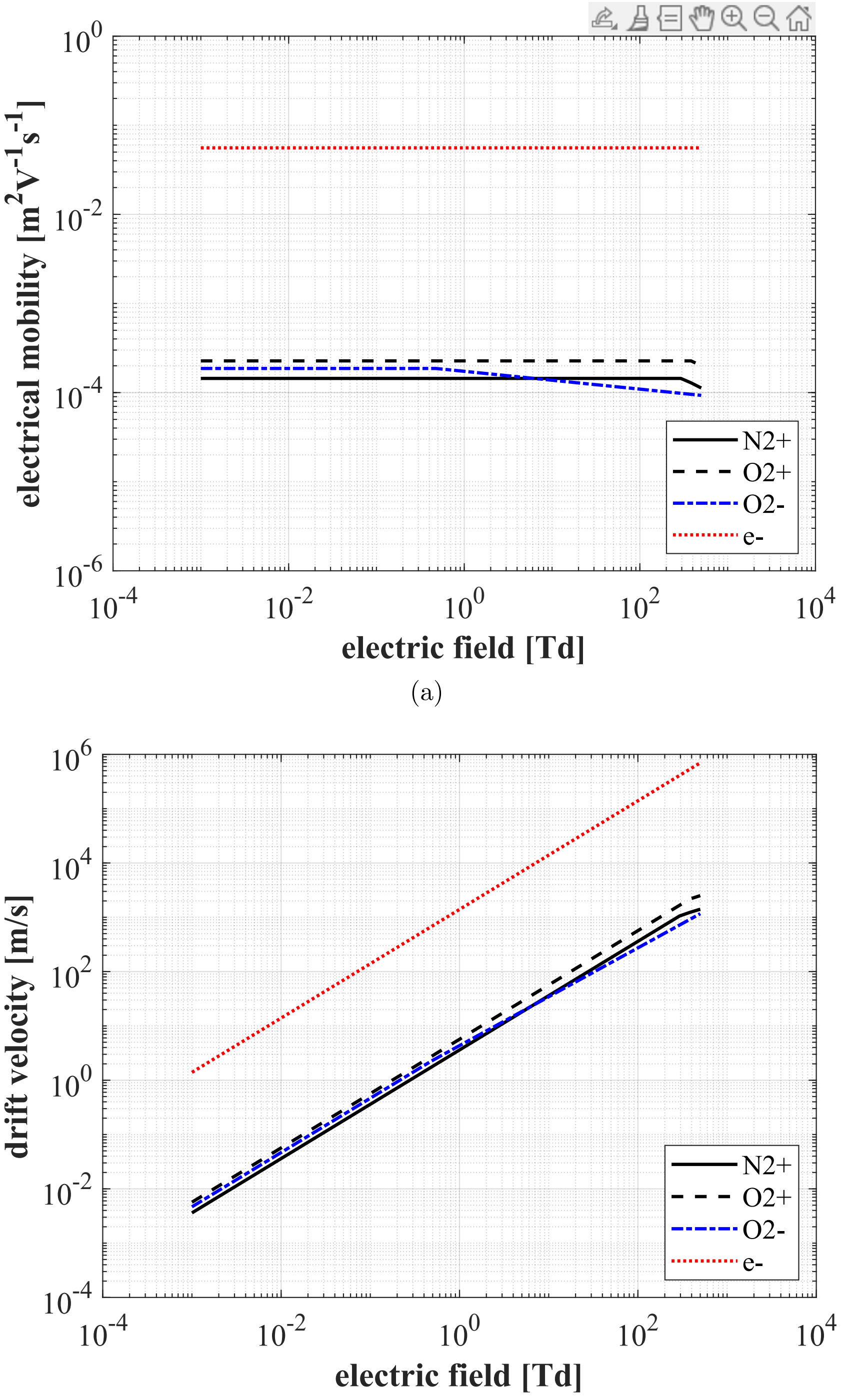

(a)

(b)

Figure 3.2: Electrical mobility for ions and electrons in atmospheric pressure dry air computed with the expressions in Table 3.1 for $T = 400\,\mathrm{K}$ and $T_e = 2\,\mathrm{eV}$ (a), and corresponding drift velocity (b)

are the reference length (L_0) time (t_0), number density (n_0) and macroscopic diffusion coefficient (D_0). A reference value for the velocity (u_0) can be conveniently obtained from L_0 and t_0. Using the obtained reference values, the quantities in Eq. (3.4) can be normalized, such that:

$$L^* = \frac{L}{L_0}; t^* = \frac{t}{t_0}; n^* = \frac{n}{n_0}; u^* = \frac{u}{u_0}; D^* = \frac{D}{D_0}. \tag{3.5}$$

The spatial and temporal derivatives are are also expressed in the same way:

$$\frac{\partial}{\partial t^*} = t_0 \frac{\partial}{\partial t}; \boldsymbol{\nabla}^* = L_0 \boldsymbol{\nabla}. \tag{3.6}$$

Hence, the time derivative in the left-hand side of Eq. (3.4) can be expressed as:

$$\frac{\partial n}{\partial t} = \frac{n_0}{t_0} \frac{\partial n^*}{\partial t^*}. \tag{3.7}$$

The two components of the integral flux are:

$$\boldsymbol{\nabla} \cdot (D \boldsymbol{\nabla} n) = \frac{D_0}{L_0^2} n_0 \boldsymbol{\nabla}^* \cdot (D^* \boldsymbol{\nabla}^* n^*) \tag{3.8}$$

$$\boldsymbol{\nabla} \cdot (n \mathbf{u}) = \frac{n_0}{t_0} \boldsymbol{\nabla}^* \cdot (n^* \mathbf{u}^*). \tag{3.9}$$

The source terms are then expressed as:

$$\Omega = \frac{n_0}{t_0} \Omega^*. \tag{3.10}$$

Finally, substituting the four different obtained terms in Eq. (3.5), the dimensionless continuity expression is obtained:

$$\frac{\partial n^*}{\partial t^*} = \frac{D_0}{L_0 u_0} \boldsymbol{\nabla}^* \cdot (D^* \boldsymbol{\nabla}^* n^*) - \boldsymbol{\nabla}^* \cdot (n^* \mathbf{u}^*) + \Omega^* \tag{3.11}$$

Finally, it should be highlighted that the coefficient multiplying the diffusive term in Eq. (3.11) represent the inverse of the Peclet number:

$$\frac{D_0}{L_0 u_0} = \frac{1}{\mathrm{Pe}}, \tag{3.12}$$

The Peclet number, representing the ratio of the advective and diffusive transport of the number density [76].

The use of a dimensionless form grants two practical advantages in the context of numerical modeling:

1. The number of computer operations is reduced, speeding up the computation time. This is particularly relevant when considering time-critical operations that are executed multiple times, such as the fluxes integration process under exam;
2. The round-off errors, inherent to the use of a finite number of digits in the floating point computer representation of numbers, are minimized. This is particularly relevant in the context of high-pressure plasma modeling, since the number densities can span over several orders of magnitude.

3.1.5 Linear and non-linear Poisson solvers

Coherently to the procedure adopted for the continuity equation in Sec. 3.1.4, the discretization process described in Chapter 2 is applied to a dimensionless version of Poisson's equation. Starting from the dimensional form of the equation:

$$\boldsymbol{\nabla} \cdot (\epsilon_r \boldsymbol{\nabla} \varphi) = -\frac{\rho}{\epsilon_0}, \tag{3.13}$$

the reference length L_0, charge density ρ_0 and electric potential ϕ_0 are defined so that:

$$L^* = \frac{L}{L_0}; \rho^* = \frac{\rho}{\rho_0}; \varphi^* = \frac{\varphi}{\phi_0}; \boldsymbol{\nabla}^* = L_0 \boldsymbol{\nabla}. \tag{3.14}$$

Substituting the defined dimensionless quantities in Eq. , a dimensionless Poisson equation is obtained:

$$\frac{\varphi_0 \epsilon_0}{\rho_0 L_0^2} \boldsymbol{\nabla}^* \cdot (\epsilon_r \boldsymbol{\nabla}^* \varphi^*) = -\rho^*. \tag{3.15}$$

When Eq. (3.15) is discretized on a one-dimensional domain, the employed Finite Volume approach yields a tridiagonal matrix $[K]$. In the FORTRAN 90 implementation of the code, the matrix $[K]$ is stored in three column arrays dd_u, dd and dd_l representing the matrix' upper, main and lower diagonals. In order to solve the corresponding linear system, the Intel Math Kernel Library (MKL) implementation of the *gtsv LAPACK* routine is employed in double precision. The *dgtsv* routine performs a Gaussian elimination with partial pivoting [77].

Differently from the 1-D case, in 2 dimensions the Poisson's problem finite volume discretization yields a pentadiagonal coefficient matrix $[K]$. The matrix is largely sparse, since the matrix has rank equal to the number of grid nodes, with at most 5 non-null entries on each row. Hence, some kind of compression must be employed to store only the non-null entries of the coefficient matrix. In the developed code, the three-array variation of the Compressed Sparse Row (CSR) format is employed to perform this task. In this work, the Intel MKL Parallel Direct Sparse Solver Interface (PARDISO) library is employed [78] for the task of solving the sparse linear system. The PARDISO routine benefits from a parallel implementation, and can be employed both in shared and distributed memory modes. Given the limited amount of considered nodes, in this work only the parallel shared memory functionality has been employed.

3.1.6 Plasma kinetics

The focus of this present work is the development of a numerical tool for the study of the plasma dynamics and charge deposition mechanisms in DBD reactors in atmospheric pressure air. The kinetic processes are essential to this process, constituting the source for the observed charged species populations. A detailed assessment of the kinetic processes in atmospheric air plasma would require to assess a large amount of reactions, especially if the neutral species are taken into account [7]. Because of the heavy computational burden associated with such an approach, detailed kinetic models of this kind are hardly applicable to one and two dimensional codes devoted to the solution of the species transport equations. Hence, simplified air kinetic models are commonly employed in drift-diffusion models [80–85].

The developed numerical code implements the kinetic model in [5], which can be optionally expanded to include several ozone production kinetic channels, from [79]. The considered elementary processes that have been modelled in this work are listed in Table 3.2. The employed reaction rates can be found in [5] or [79], as indicated the right column of the table.

Table 3.2: List of considered kinetic processes, along with the relevant reference

Process	**Reactants**		**Products**	**Source**
Ionization	$N_2 + e^-$	$\longrightarrow$	$N_2^+ + 2\,e^-$	[5]
	$O_2 + e^-$	$\longrightarrow$	$O_2^+ + 2\,e^-$	[5]
Recombination	$N_2^+ + e^-$	$\longrightarrow$	N_2	[5]
	$O_2^+ + e^-$	$\longrightarrow$	O_2	[5]
	$N_2^+ + O_2^-$	$\longrightarrow$	$N_2 + O_2$	[5]
	$O_2^+ + O_2^-$	$\longrightarrow$	$2\,O_2$	[5]
	$N_2 + N_2^+ + O_2^-$	$\longrightarrow$	$2\,N_2 + O_2$	[5]
	$N_2 + O_2^+ + O_2^-$	$\longrightarrow$	$N_2 + 2\,O_2$	[5]
	$O_2 + N_2^+ + O_2^-$	$\longrightarrow$	$N_2 + O_2 + O_2$	[5]
	$O_2 + O_2^+ + O_2^-$	$\longrightarrow$	$O_2 + O_2 + O_2$	[5]
Attachment	$N_2 + O_2 + e^-$	$\longrightarrow$	$N_2 + O_2^-$	[5]
	$O_2 + O_2 + e^-$	$\longrightarrow$	$O_2 + O_2^-$	[5]
	$O_2 + O + e^-$	$\longrightarrow$	$O_2 + O^-$	[79]
	$O_3 + e^-$	$\longrightarrow$	$O_2 + O^-$	[79]
	$O_3 + e^-$	$\longrightarrow$	$O_2^- + O$	[79]
Detachment	$O_2 + O_2^-$	$\longrightarrow$	$O_2 + O_2 + e^-$	[5]
	$O_2 + O^-$	$\longrightarrow$	$O_3 + e^-$	[79]
Dissociation	$O_2 + e^-$	$\longrightarrow$	$O + O + e^-$	[79]
	$O_3 + e^-$	$\longrightarrow$	$O_2 + O + e^-$	[79]
O_3 formation	$O + O_2 + N_2$	$\longrightarrow$	$O_3 + N_2$	[79]
	$O + O_2 + O_2$	$\longrightarrow$	$O_3 + O_2$	[79]

Numerical validation the semi-implicit integration scheme

The developed semi-implicit scheme employed for the integration of the source terms in the right-hand side of Eq. (3.4) has been tested against the well established TR-BDF2 scheme. The TR-BDF2 method is an implicit scheme, employing a combination of a trapezoidal rule and backwards differentiation [3, 4]. The considered reactions are the ones corresponding to reference [5] in Table 3.2. A constant electric field of 160 Td has been applied during a time-span of 0.05 µs. The results of the comparison are summarized in Fig. 3.3. As can be noticed, the employed time span is considerably larger than the usual time-steps employed in the simulations performed for this work. This choice was purposely made to test the numerical methodology under more restrictive conditions than those actually encountered in the results that will be presented and discussed in the following sections. The initial number densities at time $t_0 = 0\,\mathrm{s}$ of the considered species are ${\mathrm{N_2}^+}\big|_{t_0} = 0.75{\cdot}n_0$, ${\mathrm{O_2}^+}\big|_{t_0} = 0.25{\cdot}n_0$, ${\mathrm{O_2}^-}\big|_{t_0} = 0.09{\cdot}n_0$, $\mathrm{e}^-\big|_{t_0} = 0.91{\cdot}n_0$, where $n_0 = 1 \times 10^{16}\,\mathrm{m^{-3}}$. For what concerns the neutral species, their initial number densities have been set to $\mathrm{N_2}\big|_{t_0} = 0.75 \cdot 2.686 \times 10^{25}\,\mathrm{m^{-3}}$ and $\mathrm{O_2}\big|_{t_0} = 0.25 \cdot 2.686 \times 10^{25}\,\mathrm{m^{-3}}$, respectively.

The results of the described comparison are shown in Fig. 3.3. Continuous lines are employed in the picture to indicate the results obtained with the semi-implicit methodology, while markers of matching colours are used for the TR-BDF2 method. The comparison shows that the results obtained using the semi-implicit technique are well compatible with the results yielded by the TR-BDF2 routine. The highest relative percent difference between the two approaches, obtained for the ${\mathrm{O_2}^-}\big|$ density, is 1.03 %.

An important requirement that must be respected in the source terms integration process is the conservation the total electric charge. With reference to the test depicted in Fig. 3.3, the initial number densities have been selected to yields a null initial electric charge density ($\rho_0 = 0$). The latter can be obtained summing the product of each species number density and charge, as:

$$\rho = \sum_{s}^{N_s} n_s q_s, \tag{3.16}$$

where N_s is the total number of considered species. The net charge densities (normalized to n_0 and the elementary charge q_e) obtained at the end of the integration time with the semi-implicit methodology is $\rho^*_{s-i} = 2.6 \times 10^{-13}$. The same quantity, obtained at

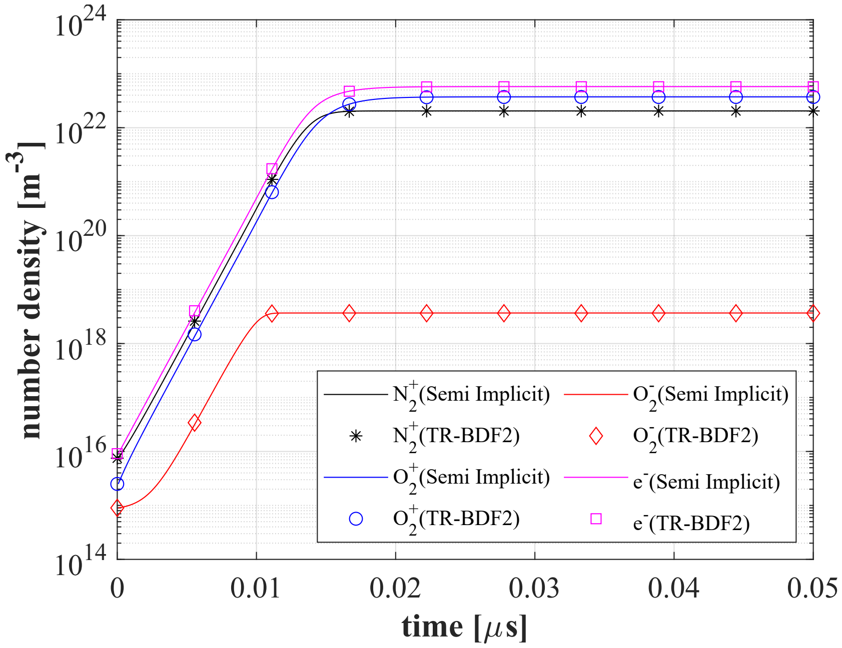

Figure 3.3: Comparison between the described semi-implicit numerical scheme and the TR-BDF2 [3, 4] integration method; Time evolution of the charged species considered in [5], with $|E| = 200\,\mathrm{Td}$

.

the end of the adopted time-span with the TR-BDF2 was $\rho^*_{s-i} = -1.76 \times 10^{-5}$. Hence, the proposed semi-implicit methodology appears to better preserve the global charge neutrality of the species involved in the kinetic processes.

3.1.7 Plasma-wall interaction

The time rate change of surface charge density on a dielectric layer due to an incident flux of particles belonging to the charged specie s is given by the following expression:

$$\frac{\mathrm{d}\rho_{\Sigma,s}}{\mathrm{d}t} = q_s |u_s n_s| \gamma, \tag{3.17}$$

where q_s is the electric charge associated with the specie s, u_s the specie velocity and n_s its number density evaluated at the grid node adjacent to the dielectric layer. If the incident particle is a positive ion, the quantity γ represents the dielectric layer secondary emission coefficient γ_{SEE}. The secondary emission coefficient is defined as the average number of electrons emitted per incident ion. Conversely, if the impacting

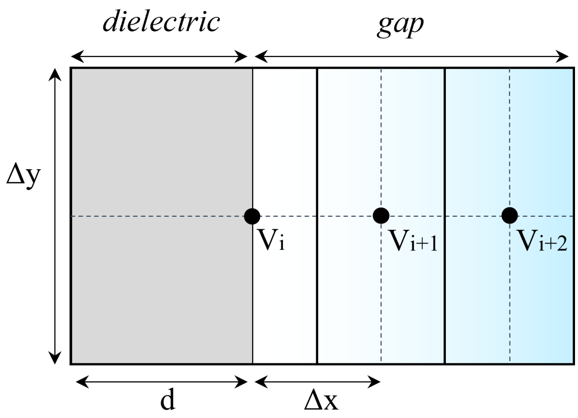

Figure 3.4: Sketch of the control volume V_i, shared between the generic dielectric layer and the gap; Δy and d are the dielectric layer width and thickness, respectively; the spacing between the nodes in the gap is Δx

species is negative, and if the considered dielectric layer is positively charged, γ represents a recombination coefficient. Otherwise, if the dielectric layer is not charged, or charged with a negative ρ_Σ, γ represents an attachment coefficient.

Positive charge fluxes

When positive ions impact a dielectric layer, providing a positive contribution to the deposited ρ_Σ, the electrons number density in the node adjacent to the dielectric layer is correspondingly increased to account for the secondary electron emission phenomena. With reference to the schematic representation of Fig. 3.4, the electron number density to be injected in the gap (due to secondary emission) can be determined by equating the variation of electric charge in the dielectric layer and in the control volume V_i:

$$\Delta\rho_\Sigma = 1/2\Delta\rho\Delta x. \tag{3.18}$$

In Eq. (3.18), ρ is the electric charge density in the control volume V_i. The total charge in V_i is obtained multiplying by $1/2\Delta x$, since the control volume is shared between and gap and the dielectric layer. The (electron) number density to be injected in in V_i at a given time step is then computed as:

$$\Delta n_e = \frac{2\Delta\rho_\Sigma}{\Delta x q_e}. \tag{3.19}$$

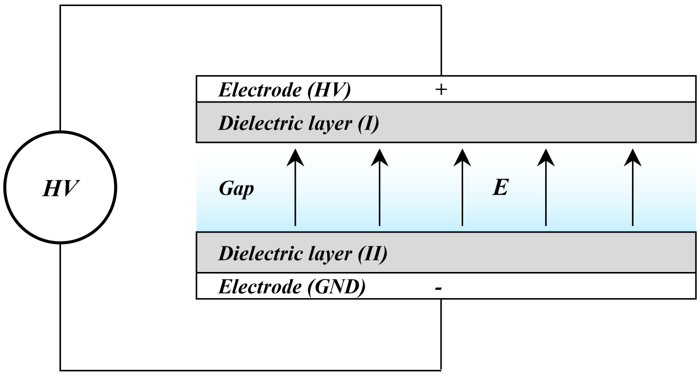

Figure 3.5: Schematic representation of the modeled Dielectric Barrier Discharge reactor volumetric reactor

Negative charge fluxes

When a flux of negative ions or electrons is directed towards a dielectric layer, the latter is subjected to a $\Delta\rho_{\Sigma} < 0$. In contrast to the case of positive charge fluxes, no secondary emission phenomena has been considered when a dielectric layer is subjected to a negative charge flux. Nevertheless, in order to grant the electrical neutrality of the modeled system, the total electric charge transferred to the layer at each time step must be removed from the gap. This is performed analogously to the above described case of positive charge fluxes, computing the Δn corresponding to the accumulated surface charge with Eq. (3.19), and then subtracting it from the control volume V_i.

3.2 Simulation of a DBD volumetric reactor

In this section, the numerical simulation of a volumetric DBD reactor is carried out using the code described in Sec. 3.1. After a description of the physical characteristics of the modeled reactor, the temporal trend of the voltage and accumulated surface charge density are discussed. Then, the obtained spatial distribution of the species number density is shown and discussed at several time instants during a cycle of the externally applied voltage.

Table 3.3: Physical characteristics of the modeled Dielectric Barrier Discharge reactor

Quantity	Value	Unit measure
Gap - thickness	4.0×10^{-4}	m
Dielectric layer - thickness	2.0×10^{-4}	m
Dielectric layer - surface	1.6×10^{-3}	m^2
Dielectric layer - ϵ_r	3.4	[–]
External voltage - amplitude	4.8	kV
External voltage - frequency	15	kHz
Temperature - ions	400	K
Temperature - electrons	2	eV

3.2.1 DBD reactor description

The modelled device – sketched in Fig. 3.5 – consists of a symmetric DBD reactor, constituted by two parallel metal electrodes separated one from each other by and air gap and two Kapton dielectric layers. The thickness of the air gap is $4 \times 10^{-4}\,\mathrm{m}$, while each of the two dielectric layers has a thickness of $2 \times 10^{-4}\,\mathrm{m}$ and a $1.6 \times 10^{-3}\,\mathrm{m}^2$ surface. The configuration is assumed to be powered by a 4.8 kV sinusoidal voltage, operated at a frequency of 15 kHz. The temperature of all ionic species is set to 400 K, while the electron temperature is assumed to be 2 eV. The discussed characteristics of the simulated configuration are summarized in Sec. 3.3.

With reference to Fig. 3.5, the gap thickness is considerably shorter than the width of the electrodes. Hence, at least in the central part of the gap, it is reasonable to assume that the electric field lines (directed from the positive to the negative electrode) are straight. For this reason, the one dimensional version of the code described in Sec. 3.1 has been employed to obtain the results that will be discussed in this section.

3.2.2 Applied voltage and surface charge density

Figure 3.6 shows the externally applied voltage (V_{ext}), alongside the computed electric potential difference over the gap during the simulation ($\Delta\phi_{gap}$). With reference to Fig. 3.5, V_{ext} is enforced between the two electrodes, marked respectively as HV and GND. $\Delta\phi_{gap}$ is computed as the difference between the electric potential (yielded by Poisson's equation) on the first and last nodes of the grid. Hence, if the nodes are numbered from

1 to n, the gap voltage is defined as:

$$\Delta\phi_{gap} = \phi_1 - \phi_n. \tag{3.20}$$

From a physical standpoint, $\Delta\phi_{gap}$ represent the voltage to which the air gap is effectively subjected. This is in general different from the externally applied voltage, because of three distinct physical mechanisms:

1. Each dielectric layer causes a voltage drop, determined by its thickness and relative permittivity ($\epsilon_{r,d}$);
2. The charged species in the gap are free charges, subjected to drift caused by the presence of external electric fields. The local electric field generated by such volumetric charge densities opposes the external field;
3. Analogously to the physical role played by free charges in the gap, the (bound) charges accumulated in the dielectric layers also contribute to screen the gap from the electric field generated by the high-voltage source.

In Fig. 3.6, the combination of the three listed mechanisms causes $\Delta\phi_{gap}$ to reach a maximum value of 475 V during the first quarter of the (first) cycle, after 2.5 µs from the beginning of the simulation. Then, while V_{ext} continues to increase, $\Delta\phi_{gap}$ starts to progressively decrease, reaching a null value in the second quarter.

During the first half of the cycle, a positive voltage is enforced on the HV electrode, adjacent to dielectric layer I. An electric field is consequently generated in the gap, causing the negative charges (negative ions and free electrons) to drift towards the anode (the HV electrode). Similarly, the positive ions are pushed towards the GND electrode, which acts as the cathode. Hence, the two dielectric layers I and II are subjected to a flux of negative and positive charges, respectively.

The surface charge accumulated in the dielectric layers during the considered two cycles of the external waveform is depicted in Fig. 3.7. As one can see by comparing Figs. 3.6 and 3.7, both dielectrics start to accumulate charges (of opposite sign) as soon as a voltage is applied to the reactor. With reference to Fig. 3.7, the first *charging front* ends at 16.8 µs, when the external voltage reaches its maximum value. At this point, as can be verified in Fig. 3.6, the external voltage has been almost completely screened

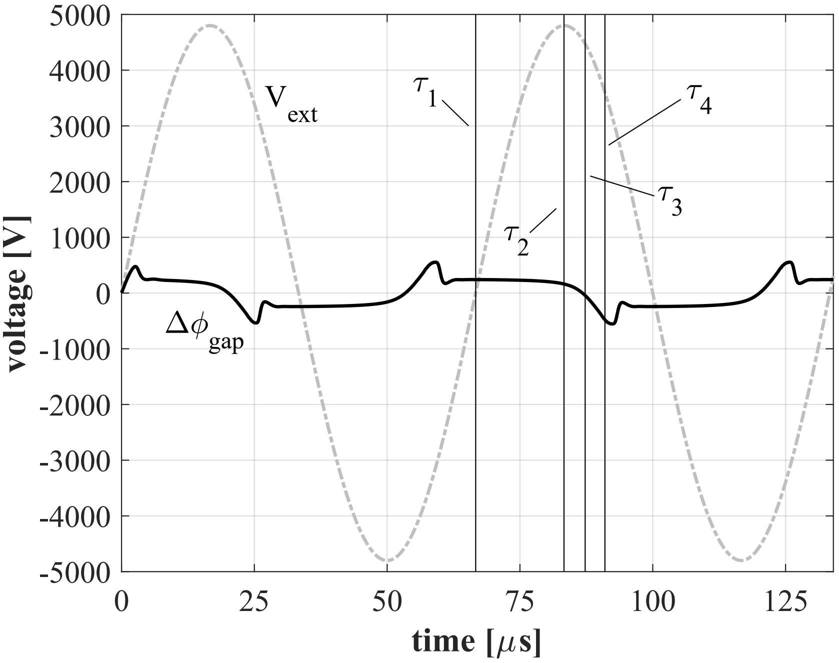

Figure 3.6: Electric potential difference over the gap ($\Delta\phi_{gap}$) during the first two cycles of the externally applied voltage (V_{ext}); The spatial distribution of the species number densities and electric potential is discussed at time-instants τ_{1-4}

out by the surface charge. The reversal of the gap voltage during the second quarter of the external voltage (after 20 µs) is caused by the surface charge, which retains its (maximum) value when V_{ext} starts to decrease after its peak at 16.8 µs.

One peculiarity that can be observed in Fig. 3.7 is that the charging process of the two dielectric layers is almost symmetrical. This fact might seem surprising, since the described model for the charge accumulation process (in Sec. 3.1.7) depends on the velocity of the incident species. While the electrons have a markedly higher mobility with respect to positive ions, the charging process of the two dielectric layers appears to take place approximately at the same rate. This physical behavior can be explained considering the combination of two factors.

Firstly, the surface charge deposition process due to ionic species is markedly faster than the considered rate of change of the external voltage. In order to verify this, a series of parametric simulations has been performed, progressively raising the high voltage source frequency. The conducted test showed that only above frequencies in the MHz range the charge deposition effect due to the positive ions was not fast enough to

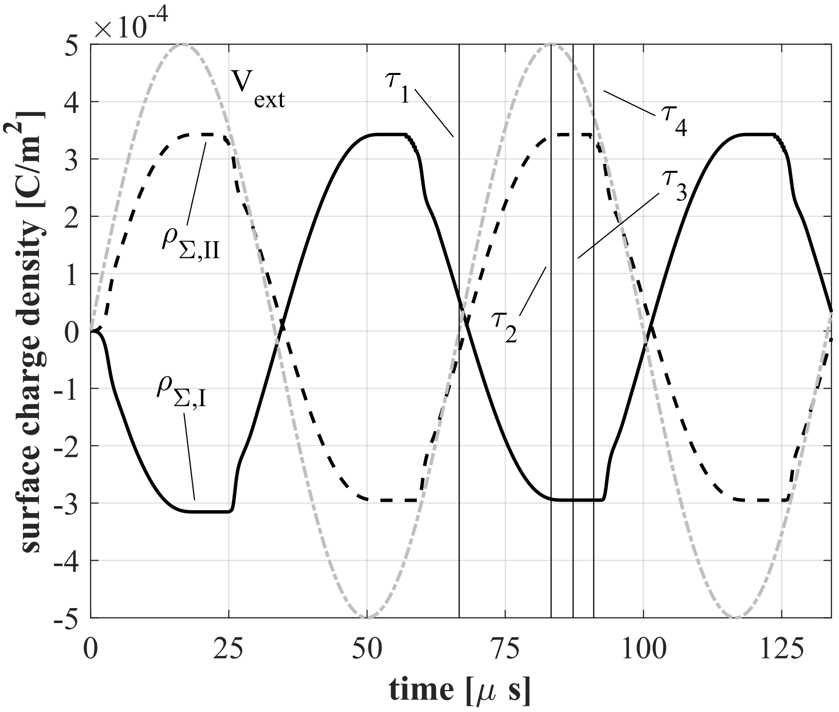

Figure 3.7: Surface charge density deposited onto dielectric layers I and II (see Fig. 3.5), over two cycles of the externally applied voltage (V_{ext})

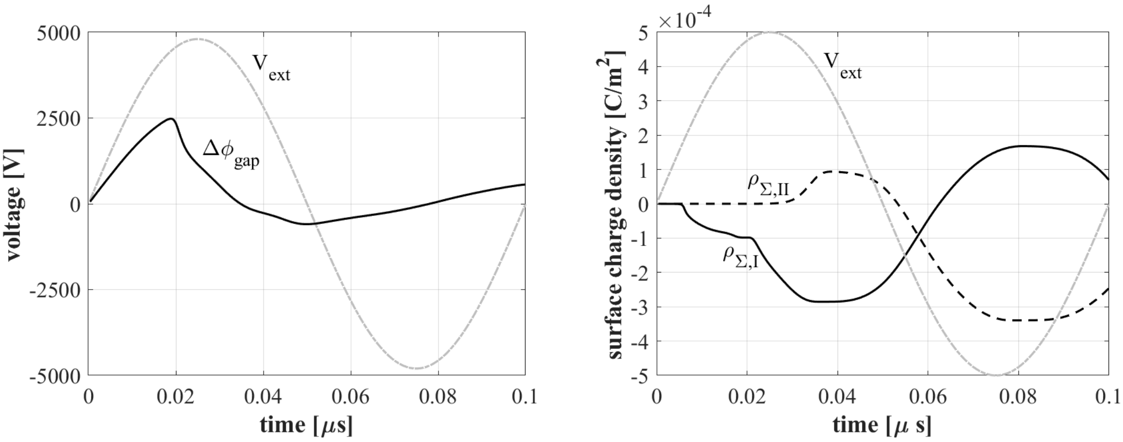

(a) (b)

Figure 3.8: Electric potential difference over the gap (a) and surface charge accumulated on the dielectric layers (b) when a a frequency of 10 MHz is employed

follow the dynamics of the external voltage. As an example of this, Fig. 3.8 shows the obtained potential difference over the gap and the deposited charge over one period of the external voltage at 1 MHz. As can be observed, at this higher frequency the rate of charge deposition due to the ions is not sufficiently fast to follow the dynamics of the externally applied voltage. This results both in an asymmetric charge accumulation profile over time (with respect to the contribution of the electrons) and in a marked increase of $\Delta\phi_{gap}$.

Secondly, while the effect of the surface charge is to screen the plasma from the external electric field, the latter is also the *driver* of the charge accumulation. Hence, at least for applied voltages in the kHz range, the surface charge accumulation acts as a negative feedback mechanism with respect to the externally applied electric field.

3.2.3 Spatial distribution of the charged species

The distribution of three charged species, i.e., $N_2{}^+$, $O_2{}^-$ and e^-, is shown and discussed at four specific time instants of the described simulation. These time instants, denoted as τ_{1-4} are marked in Fig. 3.6.

The reason for selecting τ_{1-4} in the second cycle is that – from that moment – the dynamics of the charged species reach a periodic regime, which is consistently repeated

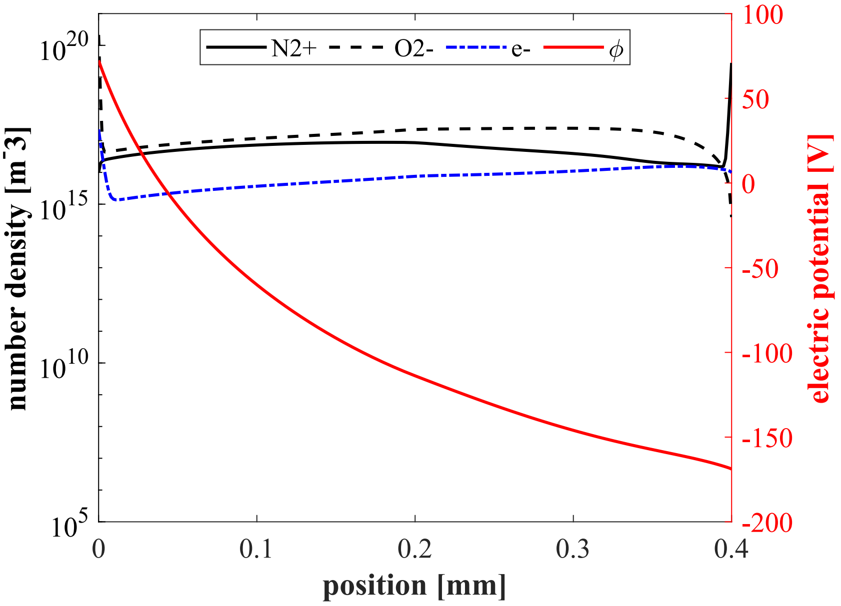

Figure 3.9: (τ_1) - number density and electric potential over the air gap after 67 µs since the beginning of the simulation

in the following cycles. Hence, the charged species distribution in τ_{1-4} is not influenced by the transient phenomena taking place during the first cycle.

Figure 3.9 shows the number densities of N_2^+, O_2^- and e^- at τ_1, i.e., at the beginning of the second cycle of the externally applied voltage V_{ext}. While at τ_1 the externally applied voltage is 0 V, the gap is subjected to a $\Delta\phi_{gap}$ of 241 V. The reason for this can be observed in Fig. 3.7: at 67 µs, part of the charge accumulated on the dielectric layers' surfaces during the firs cycle is still present. That ρ_Σ has been accumulated during the third quarter of the first cycle, to screen out the gap from the negative V_{ext}, and only partially removed during the fourth quarter. Hence, in τ_1, the positive electric field created by the negative gradient of $\Delta\phi_{gap}$ causing a drift of the negative species towards dielectric I, in the left side of the represented domain. Conversely, both N_2^+ and O_2^+ (not shown in Fig. 3.9) are pushed towards the cathode, adjacent to dielectric II. Since a null flux boundary condition has been enforced on the edges of the physical domain, positive and negative charges are accumulated on both ends of the gap. Because of this, while quasi-neutrality is achieved in the central part sheaths of opposite polarity are formed at the two ends of the gap.

The second among the instants highlighted in Fig. 3.6, τ_2 takes place after a quarter of cycle from τ_1, i.e., when V_{ext} reaches its peak value, 4.8 kV. The results obtained in τ_2 are shown in Fig. 3.10. Comparing the latter to Fig. 3.9, a few aspects can be pointed out. Despite the fact that the external voltage increased from 0 to 4.8 kV during between τ_1 and τ_2, $\Delta\phi_{gap}$ progressively decreased from 241 to 162 V. Once again, this shows the *negative feedback* excerpted by the surface charge density deposited in the dielectric layers. The surface charge deposited on layer I at τ_1 was $\rho_{\Sigma,I}\big|_{\tau_1} = 5.5 \times 10^{-5}\,\mathrm{C\,m^{-2}}$. During the time between τ_1 and τ_2, $\rho_{\Sigma,I}$ changed sign because of the negative flux of electrons and ${O_2}^-$ ions directed against layer I. The deposited charge in τ_2 reaches its maximum (negative) value of $\rho_{\Sigma,I}\big|_{\tau_2} = -2.9 \times 10^{-4}\,\mathrm{C\,m^{-2}}$. In a dual way, the same process takes place at the cathodic side of the gap due to a flux of positive charges. An interesting difference that can be noticed comparing the results in τ_1 and τ_2 is that, while the maximum value of ${N_2}^+$ number density did not change significantly, the electron density decreased during the observed quarter of cycle. The main phenomena causing the observed reduction of e^- at the left side of the gap is the attachment of electrons to O_2 molecules, forming ${O_2}^-$ ions. Another mechanism that contributes to the observed decrease is constituted by the losses of electrons associated with the surface charge deposition discussed in Sec. 3.1.7. Conversely, on the cathodic side of the gap, the number density of electrons is higher than ${O_2}^-$ thanks to the secondary emission due to the incident flux of ${N_2}^+$ ions.

The next considered time-instant, τ_3, takes place during the second quarter of the second cycle, at 87 µs. At this point, the external voltage has decreased from its peak value (τ_2) to 4.47 kV. τ_3 corresponds to the moment when $\Delta\phi_{gap}$, shown in Fig. 3.11, changes its sign. While the external voltage is still relatively close to the its peak value, the *memory* effect created by the surface charge accumulated during the first quarter of the second cycle causes the observed gap voltage inversion. Because of this, the charged species start to drift in the opposite direction with respect to Fig. 3.10. Another mechanism that is worth highlighting consist in the marked reduction of electron density throughout the whole gap taking place in the relatively short time between τ_2 and τ_3. This is due to a reduction of the maximum local electric field value in the gap between the considered two time instants. Indeed while the maximum value of the electric field ($E_{max,gap}$) during the first quarter of the second cycle always remains above 100 Td, $E_{max,gap}$ drops to nearly one quarter of that value between τ_2 and τ_3, when the sign of $\Delta\phi_{gap}$ changes. The local electric field constitutes the main source of free electrons, via

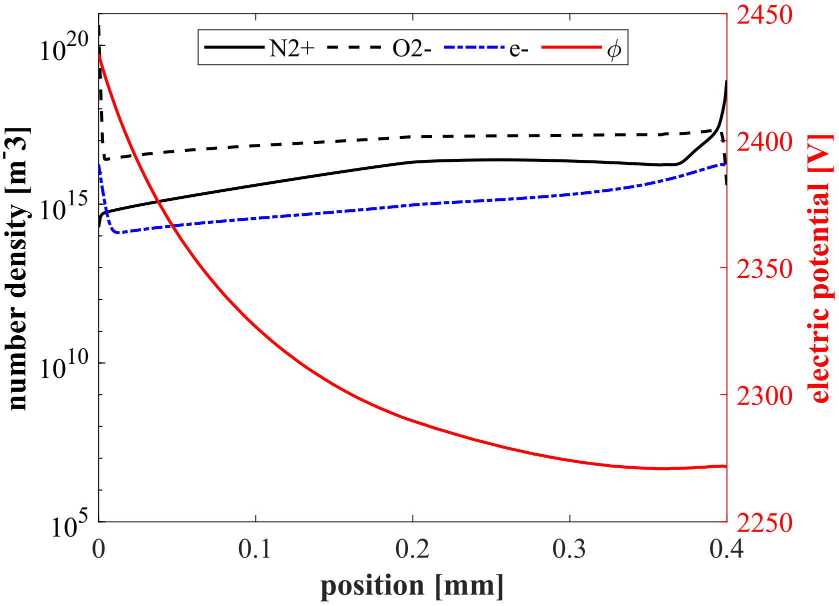

Figure 3.10: (τ_2) - number density and electric potential over the air gap after 83 µs since the beginning of the simulation

the ionization processes reported in Table 3.2. In the absence of a sufficiently intense electric field, the ionization stops, while the recombination and electron attachment processes still take place, causing the observed depletion of e^- density.

The last of the four considered time instants, τ_4, corresponds to 90 µs from the beginning of the simulation. With respect to the value at τ_3, the external voltage is further reduced in Fig. 3.12 , reaching 3.6 kV. Conversely, as can be verified form Fig. 3.7, the surface charge deposited in the dielectric did not significantly change from the peak level reached in τ_2 and τ_3. This is due to the very low number density – at the gap edges – of the actors involved in the charge deposition mechanism, i.e., the positive ions and the electrons. Therefore, the negative electric potential difference applied to the gap (previously, -43 V in τ_3) reached in τ_4 is -480 V. Together with $\Delta\phi_{gap}$, the maximum electric field increases too, up to a peak value of 165 Td near the positive electrode, adjacent to dielectric layer II. The localized intense electric field triggers the observed fast generation of electrons (until this moment almost disappeared from the gap) at the anode. The newly generated number density of electrons, combined with the intense local electric field results in the marked generation of ${N_2}^+$ ions towards the anode that can be observed in Fig. 3.12 (through ionization). The fast production of electrons and positive ions at the anode takes place multiple times, generating a series of *waves*

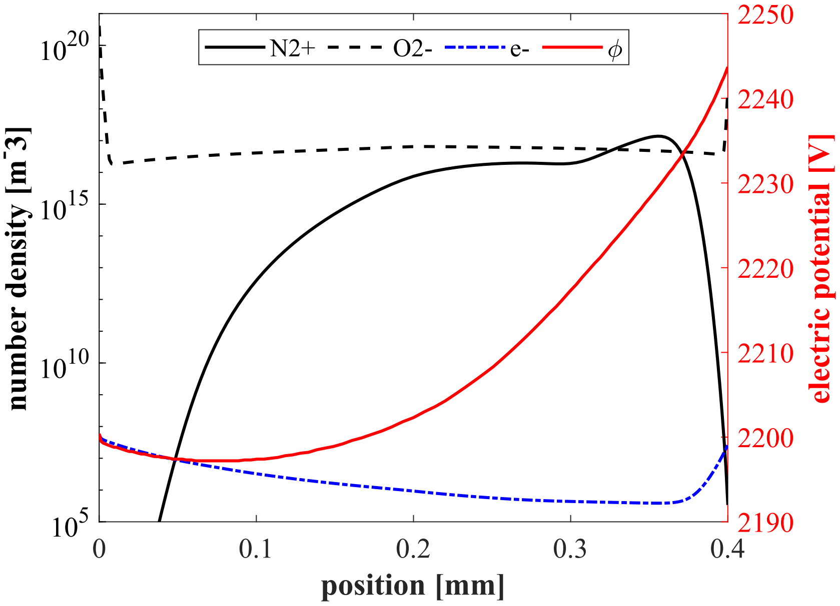

Figure 3.11: (τ_3) - number density and electric potential over the air gap after 87 µs from the beginning of the simulation

of ${N_2}^+$ travelling from the anode to the cathode. Three ${N_2}^+$ peaks generated by this mechanism can be observed in Fig. 3.12. The observed repetitive fast generation of ions at the anode eventually stops when a sufficiently large flux of positive ions reaches the cathode, causing the fast change in $\rho_{\Sigma,I}$ and $\rho_{\Sigma,II}$ that can be observed starting from 95 µs onward.

Figure 3.13 shows the computed current density in the midpoint of the gap during the performed simulation. The current density, J, has been obtained as the sum of the conduction and displacement currents:

$$J = J_c + \frac{\partial D}{\partial t}. \tag{3.21}$$

In Eq. (3.21), the conduction current J_c is obtained by summing the local fluxes of the charged species:

$$J_c = \sum_{s}^{N_s} q_s n_s u_s, \tag{3.22}$$

where N_s is the number of considered charged species, while n_s and u_s are the local number density and velocity of the given specie s.

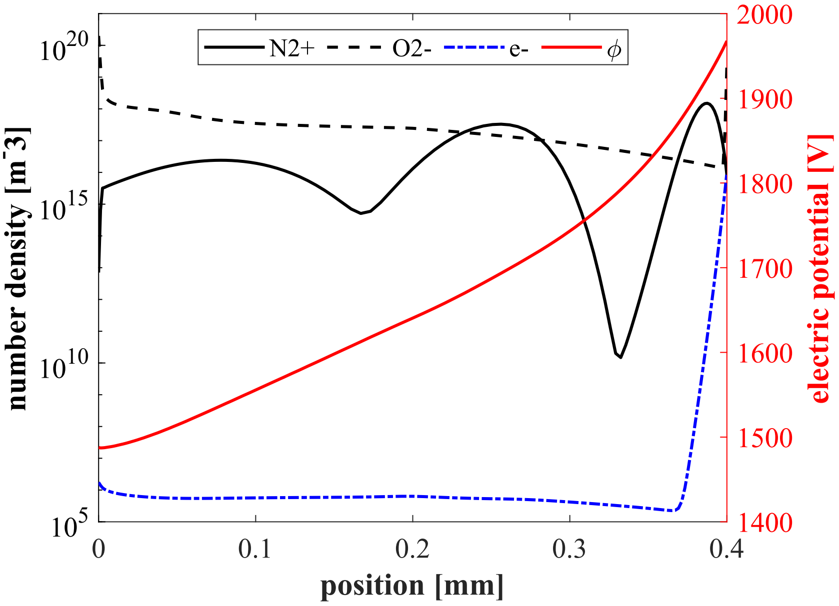

Figure 3.12: (τ_4) - number density and electric potential over the air gap after 90 µs from the beginning of the simulation

For what concerns the displacement current term in Eq. (3.21), this is obtained from the electric field at a generic time instant k and the electric field at $k-1$, divided by the Δt between the two considered instants:

$$\left.\frac{\partial D}{\partial t}\right|_k = \epsilon_0 \frac{E_k - E_{k-1}}{\Delta t_{k,k-1}}. \tag{3.23}$$

Alternatively, the total current can also be computed using the total displacement current over one of the dielectric layers. Considering e.g. dielectric layer I, the total displacement current over the layer can be obtained using Eq. (3.23), where the displacement vector is evaluated with the following expression:

$$D_I = \epsilon_0 \epsilon_{r,d} \frac{V_{ext} - \phi_i}{d}, \tag{3.24}$$

where (using the notation of Fig. 3.4) ϕ_i is defined as the electric potential of the grid node adjacent to the dielectric layer, and d is the thickness of dielectric layer I.

The spikes in the temporal profile of J depicted in Fig. 3.13 correspond to events analogous to the multiple ionic *avalanche-like* events discussed in the description of Fig. 3.12. Overall, the obtained values of current density are compatible with usual ranges

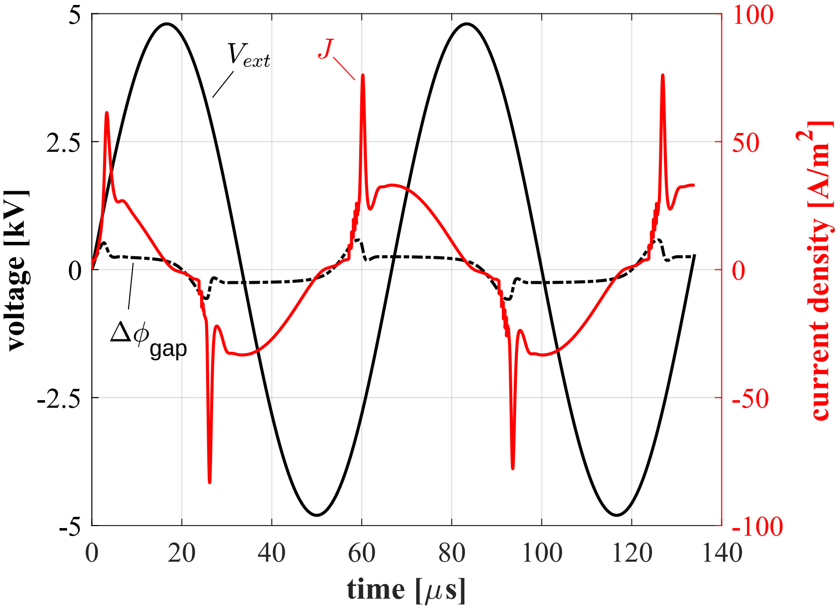

Figure 3.13: Total current density (J) computed at the midpoint of the gap during the first two cycles of the performed simulation, plotted against the externally applied voltage (V_{ext}) and the electric potential difference applied to the gap ($\Delta\phi_{gap}$)

typical of atmospheric pressure dielectric barrier discharges [80].

3.3 Comparison between different electron models

The results discussed in the previous section have been obtained using the first among the two different numerical approaches presented in Chapter 2. This approach, denominated here onwards *Full Drift-Diffusion* (FDD) for the sake of simplicity, consists in solving the transport of electrons in with the same technique employed for the ions. In this way, a drift-diffusion equation is written for each charged species, and the local volumetric electric charge density resulting from the dynamics of the species is employed at each time step as the source term for a (linear) electrostatic Poisson equation.

The second approach described in Chapter 2 has been developed to overcome the main drawback of the above described FDD methodology, i.e., the low time-steps ($\approx 1 \times 10^{-13}$ s) yielded by the CFL stability condition when the explicit time integration process is required to follow the dynamics of the electrons. The proposed *Boltzmann Drift-Diffusion* (BDD) methodology is based on exploiting the Boltzmann relation to relate the electron

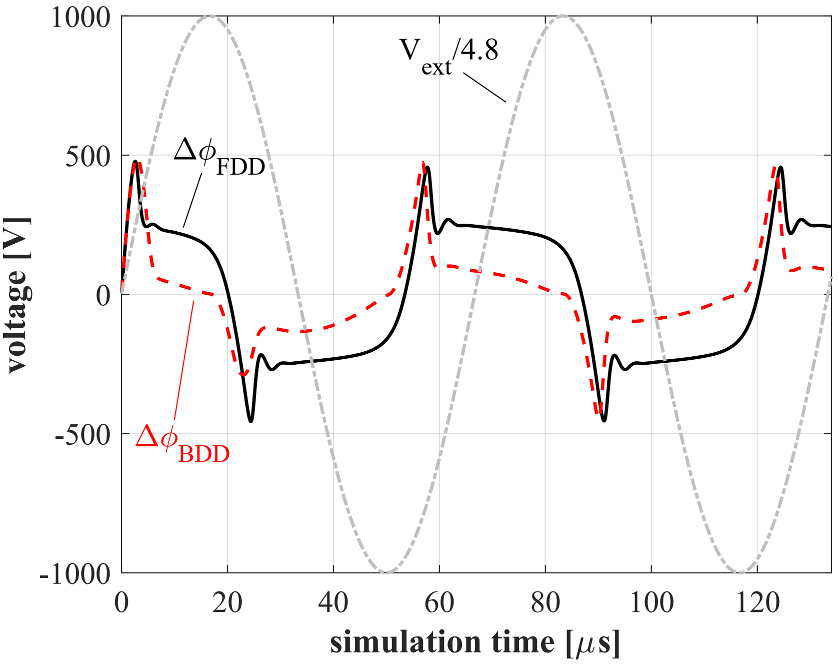

Figure 3.14: Simulation of the volumetric Dielectric Barrier Discharge reactor described in Sec. 3.2 with two different numerical methodologies; Comparison between the gap voltage obtained with the *Full Drift-Diffusion* (FDD) and *Boltzmann Drift-Diffusion* (BDD) approaches

density to the local electric potential. In this way, at each time-instant of the simulation, a drift diffusion equation is solved for each charged species except the electrons. The resulting charge density, only due to the (heavy) ionic species, is then employed to define a non-linear Poisson problem, such as the one in Eq. (2.14). In this way, the electrons are assumed to instantaneously react to the electric fields produced by external sources and the ions.

In this section, the results obtained using the developed *Boltzmann Drift-Diffusion* (BDD) methodology are compared to the ones yielded by the *Full Drift-Diffusion* (FDD) approach, discussed in Sec. 3.2. The same physical configuration described in Sec. 3.2, with the geometric and electric parameters listed in Table 3.3, has been simulated using the BDD methodology. Using this numerical technique the minimum length of the employed time-steps is typically increased of $2-3$ orders of magnitude. Because of this, multi-dimensional simulations of relatively long time-scales (such as multiple periods of applied voltages in the kHz range) can be carried out in reasonable times [86]. While Sec. 3.4 will deal with a 2D application of the developed BDD methodology, the comparison with the FDD technique is carried out in 1D.

Figure 3.14 shows the gap voltage ($\Delta\phi_{gap}$) during the first two cycles of the power supply waveform (V_{ext}), using the two methodologies. The results marked as FDD are the same reported in 3.6, discussed in 3.2. In this case, the applied external voltage has been normalized to highlight the differences yielded by the two approaches. As one can see, the two methodologies yield a qualitatively compatible trend of the gap voltage over time. In particular, once past the first half cycle, the amplitude of the $\Delta\phi_{gap}$ peaks are approximately coincident. Nevertheless, from the second quarter of the first cycle onward, the peaks of $\Delta\phi_{gap}$ obtained with the FDD method show a time delay of approximately 1 µs with respect to the results yielded by the BDD method. This is due to the assumption of the electrons instantaneously adapt their spatial distribution according to the Boltzmann relation, as a reaction to the external electric field and changes in the ions number density. Besides the small temporal shift between the two gap voltage trends, the main difference between the two approaches appears to be constituted by the lower $\Delta\phi_{gap}$ obtained when the BDD methodology is employed. This means that the mechanism by which the charged species spontaneously screen out the externally applied electric field is not exactly equal in the two examined cases.

As previously discussed, the most influential among the different physical mechanisms

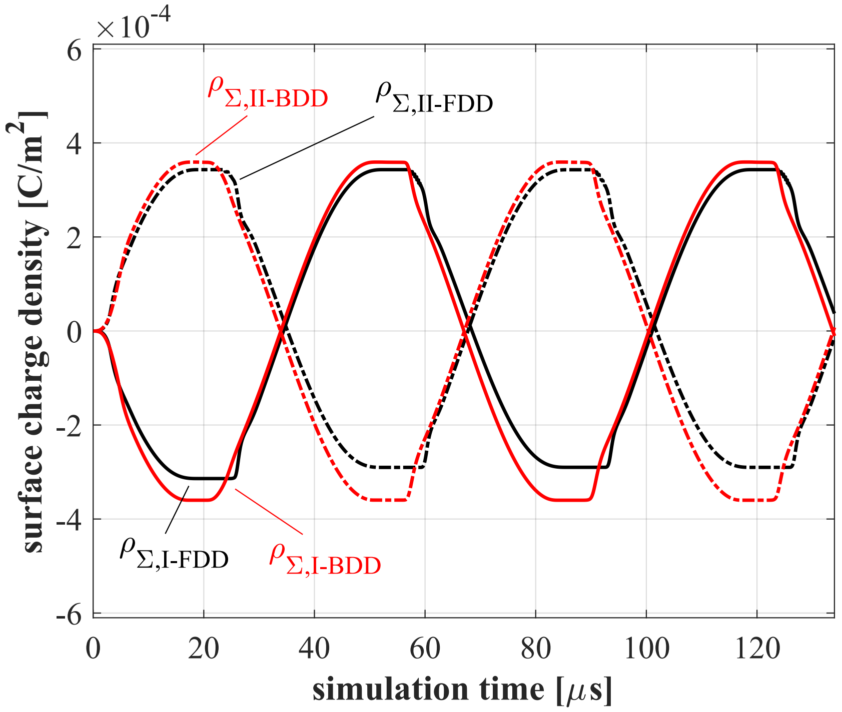

Figure 3.15: Surface charge density deposited onto dielectric layers I and II (see Fig. 3.5), over two cycles of the externally applied voltage; Comparison between the *Full Drift-Diffusion* (FDD, black line) and *Boltzmann Drift-Diffusion* (BDD, red line) approaches

determining the difference between the applied voltage and the potential difference applied to the air gap is the electric charge deposition onto the surfaces of the dielectric layers covering the powered electrodes. Figure 3.15 shows the surface charge accumulated onto the two considered dielectric over two cycles of the 15 kHz applied sinusoidal voltage, obtained with the two approaches. While, overall, the results yielded by the two approaches are in good qualitative agreement, a difference can be noticed in the negative charging process, mainly due to electrons. Indeed, as previously pointed out in Sec. 3.2, the positive and negative charging fronts yielded by the FDD methodology are slightly asymmetric. Conversely, the positive and negative surface charge deposition dynamics appear to be completely symmetric when the electrons are excluded from the drift-diffusion approach (BDD). As a result of this, a higher amount of negative charge is stored in the dielectric layers in this way, exerting a stronger screening effect with respect to the externally applied field, causing the lower shown in Fig. 3.14.

Finally, the number density distribution over the gas gap yielded by the two considered methodologies after 57.7 µs from the beginning of the simulation is shown in Fig. 3.16. The results corresponding to the *Boltzmann Drift-Diffusion* approach have been shifted 0.9 µs forward in time to compensate for the time-lag shown in Fig. 3.14. As one can see, the obtained distribution of heavy ions is comparable over the whole gap. A more apparent difference can be observed in the computed electrons number density, which drops below $1 \times 10^5\,\mathrm{m}^{-3}$ in the quasi-neutral bulk of the gas gap when the BDD approach is employed. Nevertheless, for both species, the obtained values in the sheaths at the edges of the domain are well compatible. In particular, the values of ${N_2}^+$ number density at the right-edge of the domain (cathodic side) are ${N_2}^+\big|_{FDD} = 2.43 \times 10^{18}\,\mathrm{m}^{-3}$ and ${N_2}^+\big|_{BDD} = 2.24 \times 10^{18}\,\mathrm{m}^{-3}$. Similarly, the obtained values for the electron number density et the left-edge (anodic side) of the gap are $e^-\big|_{FDD} = 1.44 \times 10^{17}\,\mathrm{m}^{-3}$ and $e^-\big|_{BDD} = 1.41 \times 10^{17}\,\mathrm{m}^{-3}$. This agreement is particularly relevant, since – for both considered species – the number density values at the two edges of the gap are orders of magnitude higher than in the bulk. In addition, as already discussed in Sec. 3.1, the charged species fluxes directed towards the walls – responsible for the surface charge accumulation process – are computed using the number density in the control volumes shared between the dielectric layers and the gap, i.e., first and last nodes of a 1D grid. Hence, the discussed agreement between the computed number densities is coherent with the compatibility shown by the surface charge trends over time in Fig. 3.15. In order

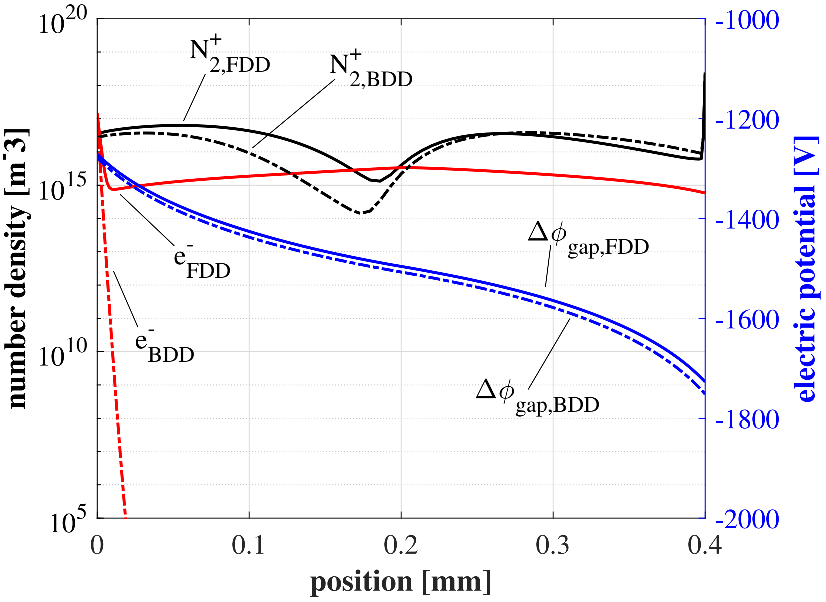

Figure 3.16: Spatial distribution of $N_2{}^+$ and e^- (left) and electric potential (right) yielded by the *Full Drift-Diffusion* (FDD, solid lines) and *Boltzmann Drift-Diffusion* (BDD, dashed lines) approaches at τ =57 µs

to have similar incident wall fluxes, a similar electric field at the gap edges must also be present. The right axis in Fig. 3.16 shows the obtained electric potential using the two methodologies. The electric potential obtained with the *Boltzmann Drift-Diffusion* methodology (which depends on the reference electric potential ϕ_0) has been increased by a constant value of 410 V, in order to allow its comparison to ϕ_{FDD}. The two obtained electric potentials are well compatible in the whole gap, satisfying the aforementioned condition on the electric field at the gap's edges.

3.4 Surface charge density experimental measurements

This section constitutes an attempt to provide a numerical validation of the developed approach. The latter has been described in Chapter 2 and employed to obtain the results presented in Sec. 3.2. A volumetric DBD reactor with the same geometrical shape and employed materials as the one modelled in Sec. 3.2 has been built and operated, aiming to measure the charge deposited by the charged species on the surface of the dielectric layers [87].

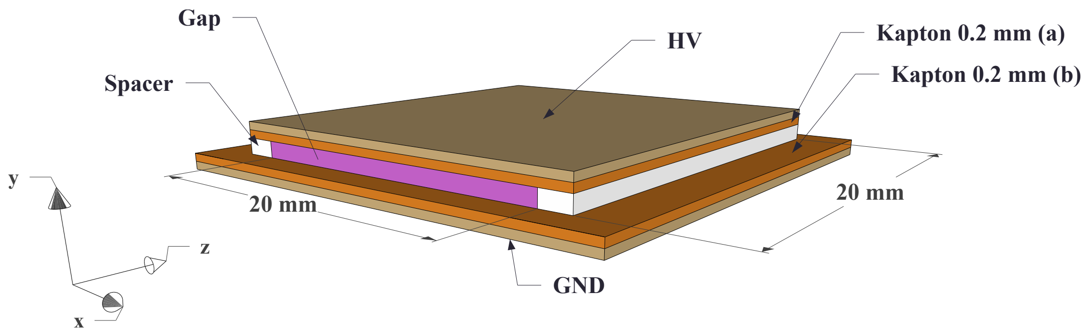

Figure 3.17: Geometry of the employed Dielectric Barrier Discharge reactor

A sketch of the considered DBD reactor geometry is reported in Fig. 3.17. The device is constituted by two parallel plane electrodes, connected to a high-voltage power source. The HV and GND electrodes are covered by two 0.2 mm thick Kapton layers. As can be noticed in Fig. 3.17, two insulating spacers create an air gap between the two dielectric surfaces. The air gap has a thickness of 0.4 mm. With reference to the geometrical measurements given in Fig. 3.17, the volume of the air gap is $20 \times 20 \times 0.4$ mm^3.

As already anticipated, the aim of the performed experiment is to measure the charge deposited by the charged species in a configuration close to the one presented in Sec. 3.2, in order to compare the measured charge density with the values predicted using the developed code. As highlighted in the Sec. 3.2, the sign and quantity of electric charge density deposited onto a dielectric layer depends on both the magnitude and the phase of the applied external voltage. For this reason – in order to obtain replicable experimental results – the applied waveform must be turned off in proximity of the zero crossing, avoiding uncontrolled oscillations of the electric field in the gap that could alter the charge deposition mechanism.

3.4.1 High-voltage multilevel generator

Conventional power supplies employed in the context of operating DBD-based devices are either power amplifiers with high voltage transformers or resonant switching converters. In general, high voltage transformers that can be used to power a DBD device are originally built for high power applications. Hence, these technologies are often inefficient when coupled with capacitive loads. On the other hand, resonant converters require to be tuned in order to achieve reasonable performances. The optimum operating frequency is fixed by the impedance of the load that – when dealing with a DBD device – can significantly change during operation. For the aforementioned reasons, together the fact that none of the two different technologies allow to directly control the generated waveform, conventional high voltage power supplies are not suitable for the purpose of measuring the charge deposited on the surface of the dielectric layers of a DBD reactor.

In order to meet the previously discussed technical requirements, the high-voltage high-frequency multilevel voltage generator described in [88–90] has been employed to power the DBD reactor employed to perform the described experimental measurements.

The high-voltage generator is realized by cascading 24 H-bridge modules, individually supplied by insulated flyback converters. The generator can deliver 49 output voltage levels. Each individual H-bridge module has a 600 V DC supply, powered by a flyback converter fed from a 12 V DC battery, allowing a maximum output voltage of ±14.4 kV (600 V×24) with frequencies up to 20 kHz. The voltage generator can then produce arbitrary voltage waveforms. This topology allows the applied voltage to be stopped at a desired value, avoiding the presence of oscillations that could produce changes in the amount of deposited surface charge density leading to inaccurate measurements.

3.4.2 Surface charge density measurement procedure

The electric potential induced by the electric charge charge density accumulated on the surface of the dielectric layers is measured with an electrostatic 341B 20 kV TREK voltage probe, with the following procedure:

1. 10 cycles of a 4.8 kV (pseudo) sinusoidal waveform at 15 kHz are applied between the HV and GND electrodes of the DBD device. At the end of the 10 cycles burst, the applied voltage is stopped upon reaching 0 V, both after a positive and negative half-cycle. These two situations correspond to a 0-crossing with negative and positive time-derivative of the applied voltage, respectively;

2. After the discharge extinction, the HV electrode is removed and the electrostatic probe depicted in Fig. 3.18 is moved along the z-direction over the dielectric surface (while being held at a constant vertical distance of 2 mm). In this way, the electric potential induced by the electrostatic surface charge density accumulated on the dielectric is measured;

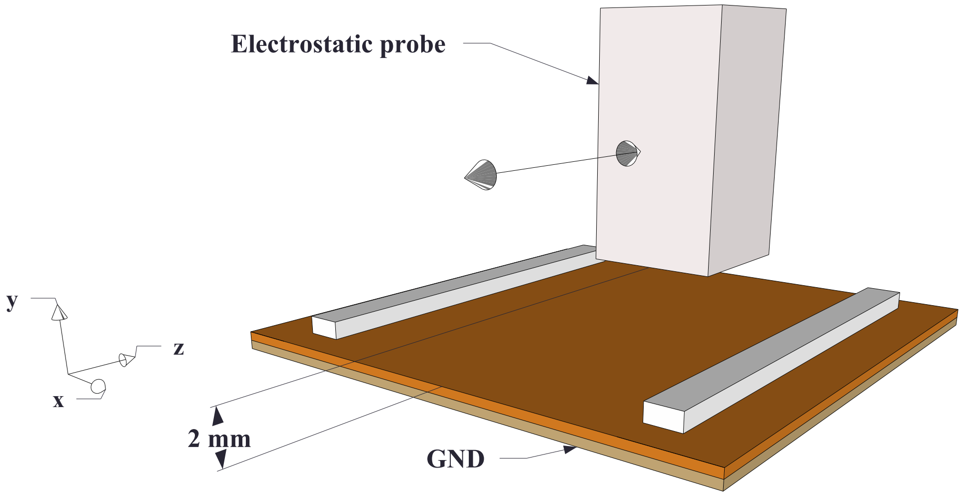

Figure 3.18: Handling of the electrostatic probe employed to perform the described measurements of deposited charge on surfaces of the dielectric layers

3. The surface of the dielectric layer is wiped and heated to eliminate possible traces of humidity;
4. The potential probe is once again used to check the absence of stored charges on the dielectric layer.

3.4.3 Comparison between simulations and experimental results

Following the procedure described in Sec. 3.4.2, two different tests have been carried out. In Test I, a symmetric configuration with both the HV and GND electrodes covered by dielectric layers has been considered. Conversely, Test II focused on an asymmetric configuration with only the HV electrode covered by a dielectric layer, leaving the GND electrode exposed to the plasma in the air gap.

The observed potential distribution presents a uniform region of about 1.5 cm, corresponding to the inner part of the air gap volume. The measured electric potential in that region of space, averaged on 5 different measurements, has been reported in Table 3.4 for both Test I and Test II.

The numerical simulation of the considered DBD configuration has been performed using the described *Boltzmann Drift-Diffusion* (BDD) methodology. The numerical technique has been applied to a bidimensional domain, where a structured non-uniform

Table 3.4: Measurements of the electrostatic potential induced by the surface charge deposited on the dielectric layers of a symmetric (Test I) and asymmetric (Test II) Dielectric Barrier Discharge volumetric reactor

Test	**Configuration**	**$dV/dt\|_{V=0}$**	**Electric potential [V]**	**Standard deviation**
I	Symmetric	> 0	-800	$< 10\,\%$
	Symmetric	< 0	800	$< 10\,\%$
II	Asymmetric	> 0	-1250	$< 10\,\%$
	Asymmetric	< 0	1250	$< 10\,\%$

grid of the same kind as the one shown in Fig. 3.1. The numerical values of the main physical quantities considered in the code are listed in Table 3.3. For what concerns atmospheric air plasma kinetics, all the reactions listed in Table 3.1.6 have been considered. In contrast, only the process marked with reference [5] have been considered to obtain the results discussed in Sec. 3.1.5.

The developed BDD methodology has been employed to simulate both the symmetric and asymmetric configurations corresponding to Test I and Test II in Table 3.4. The employed grid for the 2D domain finite volume discretization consisted of 111 nodes in the $y-$direction, corresponding to the air gap, and 41 nodes in the $x-$direction. A non-uniform grid spacing has been enforced along the $y-$direction, so that the spacing between nodes gradually increased from the gap ends (4 µm) to the gap central region (12 µm). Since the experiments have been conducted in atmospheric pressure air, the number densities of neutral molecular nitrogen and oxygen have been initially set to $1.88 \times 10^{25}\,\mathrm{m}^{-3}$ and $0.63 \times 10^{25}\,\mathrm{m}^{-3}$, respectively. For what concerns the ionic species and the electrons, the simulation was started with a uniform distribution of the charged species in the whole gap, with a ionization rate of 1×10^{-9}.

Figure 3.19 shows one cycle of the externally applied voltage (black, solid line), the electric potential difference $\Delta\phi_{gap}$ across the gap (black, dotted line) and the surface charge density accumulated on dielectrics I and II. As in Fig. 3.5, dielectric layer I and II cover the HV and GND electrodes, respectively. The HV electrode is located at the left edge of Fig. 3.19. Coherently with the results yielded by the application of the BDD methodology on a one-dimensional domain in Fig. 3.15, the computed positive and negative surface charging trends are symmetric, i.e., the same peak values surface charge are yielded by positive and negative charge fluxes against the dielectric layers. In order to compare the simulation results to the experimental measurements reported in Table 3.4, the electrical potential produced by the charge deposited onto the surface of the dielectric layers (ϕ_d) was computed at the zero-crossings of the external voltage, taking place at $\tau_1 = 33.3\,\mu\text{s}$ and $\tau_2 = 67.7\,\mu\text{s}$. Since the external voltage is positive before τ_1, $dV/dt\big|_{\tau_1} > 0$, while (for the opposite reason) $dV/dt\big|_{\tau_2} < 0$. The values of ϕ_d in τ_1 and τ_2 were inferred from the computed surface density using the following expression:

$$\phi_d = \frac{\rho_\Sigma d}{\epsilon_0 \epsilon_{r,d}}, \tag{3.25}$$

where d is the thickness of the layer, and $\epsilon_{r,d}$ the relative permittivity of the employed dielectric material, i.e., Kapton.

The obtained results $\phi_d\big|_{\tau_1}$ (positive time-derivative of the external voltage) and $\phi_d\big|_{\tau_2}$ (negative derivative) are 638 V and 716 V, respectively. These results, obtained using the *Boltzmann Drift-Diffusion* methodology, exhibit a reasonable agreement with the experimental measurements (reported in Table 3.4), obtained by scanning the electric potential on the dielectric surface of the specimen. Another interesting feature that can be found in both experimental and numerical results is the symmetry between the maximum (positive and negative) surface charge values. This is notable, since – in reason of the different transport parameters and coefficients regulating the charge deposition mechanisms – one could expect the positive and negative charging processes to be completely different one from the other. The highlighted symmetry is a further evidence that the charge accumulation process on the dielectric layers should be regarded as a negative feedback mechanism exerted by the charged species.

Figure 3.20 shows the results obtained from the numerical simulation of the physical configuration employed to perform Test II. All the electrical and geometrical quantities employed for the analysis of Test I have been retained, with the exception of dielectric II, which has been removed. The results depicted in Fig. 3.20 show that, analogously to what has been observed in Test I, the charge deposited onto the dielectric layer surface strongly influences the difference between the external voltage and the electric potential difference which the gap is subjected to. As in the previously discussed symmetric (1D and 2D) cases, this deposited surface charge is responsible for reducing $\Delta\phi_{gap}$ in the first quarter of the external waveform cycle. Indeed, the electrostatic potential ϕ_d due to the charge deposited during the first quarter has the same polarity of the exposed electrode, located located on the opposite side of the gap. Then, after reaching the peak

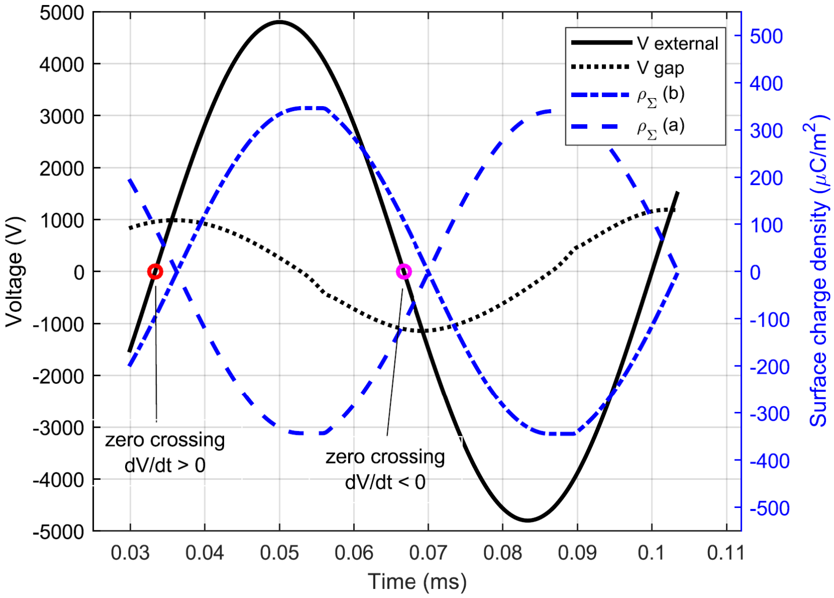

Figure 3.19: Numerical results for Test I, configuration with two dielectrics; Externally applied voltage, gap voltage and surface charge deposited on the dielectric layers obtained with the *Boltzmann drift-diffusion* methodology

value of V_{ext}, the delay in the neutralization of the deposited charge (also discussed for a symmetric configuration in Sec. 3.2) is responsible for the observed polarity inversion, since V_{ext} decreases faster than ϕ_d. It should be highlighted that the obtained $\Delta\phi_{gap}$ profile reflects the asymmetry of this considered configuration. Indeed, now the charge deposition (during each quarter) is due to either the heavy positive ions or the electrons, allowing their different physical properties and macroscopic transport parameters to be reflected in the charge deposition mechanism. Moreover, it is worth noticing that the maximum and minimum values of ρ_Σ are now approximately doubled with respect to the values obtained in Test I. The computed values of $\rho_\Sigma\big|\tau_1$ and $\rho_\Sigma\big|\tau_2$ correspond to 493 V and −241 V, respectively. Hence, unfortunately, the agreement with the experimental results is not as satisfactory as the one observed for Test I. Possible reasons for this can be an inadequate modeling of the plasma-electrode interaction, leading to inaccuracies in the charge deposition dynamics.

Finally, as an example of the spatial number distributions yielded by the BDD code in two dimensions is provided in Fig. 3.21. The figure shows the ozone number density obtained in Test I, after 86 µs of simulation, computed using the set of reactions listed in Table 3.2. As one can see, the peaks of ozone number density are found at the domain's

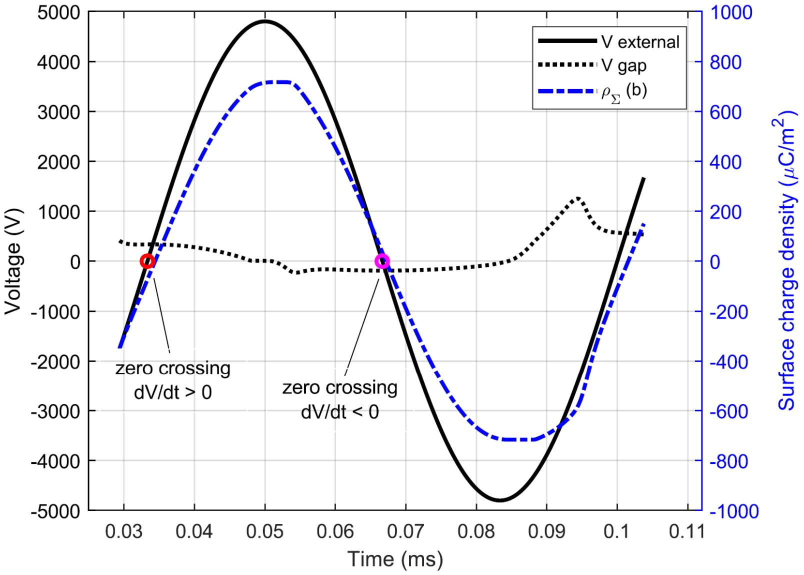

Figure 3.20: Numerical results for Test II, configuration with one dielectric (covering the HV electrode); Externally applied voltage, gap voltage and surface charge deposited on the dielectric layer obtained with the *Boltzmann drift-diffusion* methodology

edges, diffusing towards the gap bulk. This is caused by the highest values of reduced electric field and number densities of the species (involved in the ozone creation kinetic mechanism) taking place in the (positive or negative) sheaths at the edges of the gap.

3.4.4 Influence of the initial ionization degree

Finally, a parametric test is conducted in this section, in order to assess the influence of different initial ionization degrees on the dynamics of the charged species. The same configuration employed in the previous sections has been simulated – using the *Full Drift-Diffusion* approach – for a range of different values of n_0. The constant n_0 is employed to define the initial number densities injected in the domain, with the ratios described in Sec. 3.1.2. In this way, e.g., if $n_0 = 1 \times 10^{16}\,\mathrm{m}^{-3}$ the initial distribution of ${N_2}^+$ and ${O_2}^+$ is set to $0.75 \times 10^{16}\,\mathrm{m}^{-3}$ and $0.25 \times 10^{16}\,\mathrm{m}^{-3}$, respectively.

Figure 3.22 depicts the temporal evolution of the average number density of ${N_2}^+$, ${O_2}^+$ and e^- over one period of the external voltage, starting from two different values of the above defined n_0 parameter. The external voltage frequency is set to 15 kHz, and the two employed values of n_0 are $10 \times 10^{14}\,\mathrm{m}^{-3}$ in Fig. 3.22a and $10 \times 10^{18}\,\mathrm{m}^{-3}$

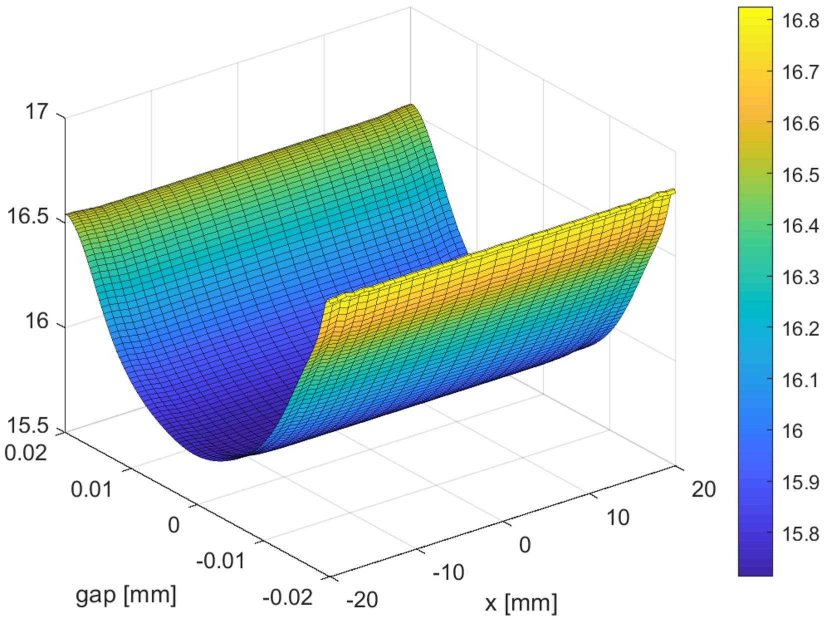

Figure 3.21: Distribution of O3 number density ($\log(n_{03})$) obtained from the simulation of the symmetric configuration corresponding to Test I, after 86 µs

Fig. 3.22b. In this way, the same configuration is simulated starting from two markedly different levels of gas ionization. The obtained results show that – regardless of the considered initial ionization degree – the considered number densities (averaged over the gap) reach the same values within the first 6 µs from the beginning of the simulation. Afterwards, a periodic regime is established, consistently retained in the following cycles of the externally applied voltage. The right axes in Fig. 3.22 shows the maximum value (over the gap) of the electric field over time. The electric field constitutes the main *driver* of the kinetic processes that lead to the observed regime of the number densities. Indeed, comparing the two presented cases, the rapid initial growth of the number densities in Fig. 3.22a is associated to a corresponding intense electric field, over 200 Td.

Finally, it is worth specifying that – although only two different cases have been shown here – n_0 was changed from $1 \times 10^{10}\,\mathrm{m}^{-3}$ to $1 \times 10^{18}\,\mathrm{m}^{-3}$. The results are quantitatively consistent with the above described trend over the whole considered range of initial number densities. This means that the results shown in the previous sections (including the experimental validation) have a weak dependence on the initial conditions enforced on the number species, and show a good consistency of the proposed modeling approach.

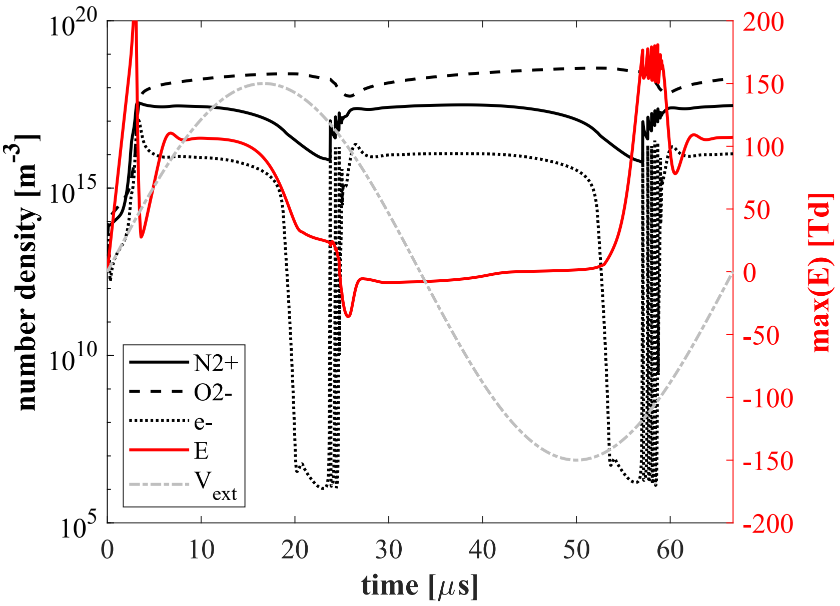

(a) $n_0 = 1 \times 10^{14}\,\mathrm{m}^{-3}$

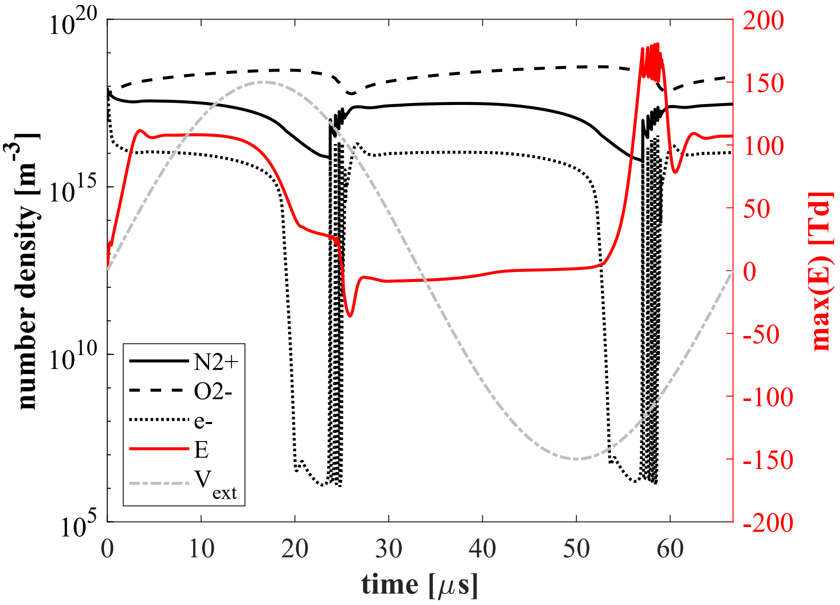

(b) $n_0 = 1 \times 10^{18}\,\mathrm{m}^{-3}$

Figure 3.22: Left Axis: temporal evolution over one period at 15 kHz of the average number density in the gap, starting from two different initial ionization rates; Right Axis: maximum electric field in the gap during the same time interval.

4 Particle Modelling

The fluid approach presented in the previous chapter provides a macroscopic physical description of a plasma. The main hypothesis behind such kind of approach is that the (charged) gas under analysis behaves like a continuum, and hence can be represented as a fluid. This characteristic is closely related to how frequently the gas particles are subjected to collisions. Indeed, collisions tend to thermalize the gas, driving the species velocity distribution function towards a Maxwellian [91].

The Knudsen number relates the particles mean free path λ to the characteristic length L of the physical system under consideration:

$$K_n = \frac{\lambda}{L}, \tag{4.1}$$

where the mean free path $\lambda = 1/(\sigma n)$ is a function of the cross section (σ) and the number density (n). If $K_n \ll 1$, which often happens at high pressures, the particles will undergo a high number of collisions over a distance L. In these cases, the velocity distribution of the gas will likely be Maxwellian and the flow is said to be in continuum. On the other hand, if $K_n \gg 1$ collisions between particles are so infrequent that can be ignored. Such a regime is is commonly referred to as free molecular flow. Finally, if $K_n \approx 1$, the distance between collisions is comparable to the characteristic length. In this case, corresponding to a rarefied gas, the particles velocity distribution function is not guaranteed to be Maxwellian.

While fluid approaches are more frequently employed for the modelling of physical systems characterized by low Knudsen numbers, kinetic models are often employed for cases where $K_n \gg 1$, or in general when a priori knowledge of the velocity distribution function of the particles cannot be assumed.

Through the years, this kind of approach has been applied to a wide spectrum of different applications. In astrophysics, for the study of planetary and stellar magnetosphere [92], as well as solar wind [93, 94]. In the electronics industry, kinetic models are often employed to simulate dynamics of the charge carriers in semiconductor devices [95]. In the nuclear fusion field, kinetic approaches are adopted for modeling negative ion extraction in the context of neutral beam injection [96,97] and high energy particle-surface interactions [98, 99]. Finally, kinetic (and hybrid) models are largely employed in the field of plasma propulsion, both for the study of basic physical phenomena and as a tool for the thrusters design [100].

The core concept of kinetic approaches is to provide a microscopic representation of the ionized gas, composed of a finite number of charged ions, electrons and neutrals. In this spirit, instead of solving a set of differential equations corresponding to the moments of the Boltzmann equation (5.1), particle methods such as Particle-In-Cell employ a finite number of macro-particles to discretize the velocity distribution function for each of the considered species.

$$f(\mathbf{r},\mathbf{v},t) \approx \sum_{p=1}^{N} w_p f_p(\mathbf{r},\mathbf{v},t), \tag{4.2}$$

where N is the number of employed macro-particles, and w_p the statistical weight, i.e., the number of gas particles corresponding to a macro-particle:

$$w_p = \frac{N_{gas}}{N}. \tag{4.3}$$

A proper choice of this quantity is a key point of a particle simulation. In fact, the statistical weight has to be low enough to maintain the number of macro particles reasonable (for performance reasons), while still providing an accurate discretization of the specie distribution function. Indeed, the numerical noise associated with the discretization of the VDF is proportional to $1/\sqrt{N}$, where N is the number of macro-particles [38]. As the charge to mass ratio of the macro-particle is the same as the real particles, their trajectories are the same. A macro-particle with specific weight w_p and charge q_p corresponds to w_p particles per unit of volume when the number density is evaluated. The momentum of the particle p can be computed from its mass (m_p) and velocity v_p, as $w_p m_p v_p$.

It is worth highlighting that, while a a single (uniform) specific weight is assigned to all employed macro-particles, this is not the only possibility. Indeed, employing different weights allows a better resolution of the high-velocity tail of the distribution function. The latter is responsible for several key physical mechanisms, such as ionizations, erosion of walls etc. The disadvantage of such a choice, however, is that it leads to an increased complexity of the code. When variable specific weights are employed, indeed, the injection of particles is less straightforward, and the implementation of particle *joining* and *splitting* algorithms is often required [101] to grant an optimal number (between 10 and 50) of macro-particles per cell [39].

4.1 Electrostatic Particle-in-Cell

The Particle-In-Cell (PIC) method has been developed from the late 50's through the works of Buneman [102] and Dawson [103, 104]. In the following decades, the methodology has been formalized and popularized by Hockney [105], Birdsall [106] and others. In this section, the main features of an Electrostatic (non-relativistic) Particle-in-Cell (ES-PIC) code are presented, as the foundations for the hybrid ES-PIC code employed in Chapter 5 for the study of low-power Hall thrusters.

As outlined in Fig. 4.1, an ES-PIC code is composed of several operations involving the employed macro-particles. These are cyclically repeated over each time-step used to advance the simulation time. Given a set of macro-particles, in the *scatter* phase the electric charge densities due to the distribution of charged species are evaluated at the nodes of a computational grid. Then, the charge density at every grid node is employed to compute the electric field (subjected to the boundary conditions), which is then interpolated (*gathered*) at the macro-particles positions. In this way, the electrostatic force acting on each particle due to external and self electric fields is obtained, and used in the *move* phase to integrate the particles trajectories over a time step, to complete the cycle.

The following sections are devoted to a brief discussion of the above mentioned fundamental parts of an ES-PIC, starting from a collisionless case. Afterwards, the Monte Carlo Collision PIC (MCC-PIC) – a commonly employed extension of the PIC method used to account for plasma kinetic processes – is briefly discussed and compared against a an alternative methodology, i.e., the Direct Simulation Monte Carlo PIC (DSMC-PIC).

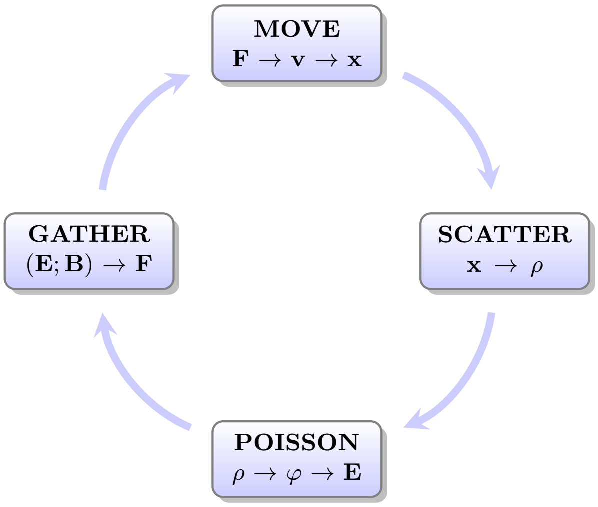

Figure 4.1: Typical scheme of a collisionless electrostatic PIC simulation cycle

4.1.1 Particle Mover

Let's consider a collection of macro-particles, each characterized by a position $\mathbf{r}$ and velocity $\mathbf{v}$. At the $k-$th time instant, assuming that the force $\mathbf{F}_k$ acting on a given macro-particle p is known, the particle position and velocity can be time-integrated over a time-step, Δt by integrating the following two first-order differential equations:

$$m\frac{\mathrm{d}\mathbf{v}}{\mathrm{d}t} = \mathbf{F} \tag{4.4}$$

$$\frac{\mathrm{d}\mathbf{r}}{\mathrm{d}t} = \mathbf{v} \tag{4.5}$$

In this way, $\mathbf{r}^k$ and $\mathbf{v}^k$ are *advanced* to the following time instant $k+1$.

The Leapfrog scheme

Although a simple forward Euler method could theoretically be applied to follow the trajectory of a particle, in practice higher order schemes such as Runge-Kutta methods or the Leapfrog method are employed. Figure 4.2 depicts the conceptual scheme behind the Leapfrog scheme, i.e., the particles positions and velocities are computed at interleaved time-instants, allowing to perform a centred time-discretization (hence the second order accuracy). Starting from the $k-$th time instant, the velocity at $k+1/2$ is computed from the velocity at the previous time instant and $\mathbf{a}_k$, the particle acceleration computed at time k.

$$\mathbf{v}_{k+1/2} = \mathbf{v}_{k-1/2} + \mathbf{a}_k \Delta t, \tag{4.6}$$

where $\mathbf{a}_k$ is obtained from the Lorentz force evaluated at k. Let's assume, for the moment, that no magnetic field is present. Hence, given the considered particle mass m_p and charge q_p, the aforementioned Lorentz force at time instant k writes as:

$$\mathbf{a}_k = \frac{\mathbf{F}_k}{m_p} = \frac{q_p}{m_p}\mathbf{E}. \tag{4.7}$$

Then, the particle position at the $k+1-$th instant is obtained by inserting the computed acceleration in Eq. (4.6), yielding:

$$\mathbf{r}_{k+1} = \mathbf{r}_k + \mathbf{v}_{k+1/2}\Delta t. \tag{4.8}$$

Since the position $\mathbf{x}$ and velocities $\mathbf{v}$ of the particles are not computed at the same time-instant, some sort of *synchronization* must be enforced between the two quantities. This is generally performed at the first execution of the cycle, by *rewinding* the particle velocities by half a time step, from $\mathbf{v}_0$ to $\mathbf{v}_{-1/2}$.

In the Leapfrog scheme, the particles position and velocities are computed using exclusively physical information pertaining to the previous time-step. Hence, the scheme is explicit and its stability is subjected to the Courant-Friedrich-Levy (CFL) condition [107]. The latter has been already discussed in Chapter 2 for the forward Euler integration scheme. In the case of a PIC code, the CFL condition is satisfied when the particles do not travel more than a single grid cell per time step:

$$\Delta t \leq \frac{\Delta x}{|\mathbf{v}|} \tag{4.9}$$

The described Leapfrog scheme presents several advantages over Runge-Kutta methods. Firstly, it is a symplectic integrator, meaning that they cause a bounded energy error [108]. Also, the Leapfrog is more computationally efficient than its corresponding order Runge-Kutta counterpart, and is time-reversible. On the other hand, Runge-Kutta methods can be easily extended to higher order of accuracy (the Leapfrog scheme is second order accurate). Moreover, unlike the Leapfrog, it does not require the time-step to

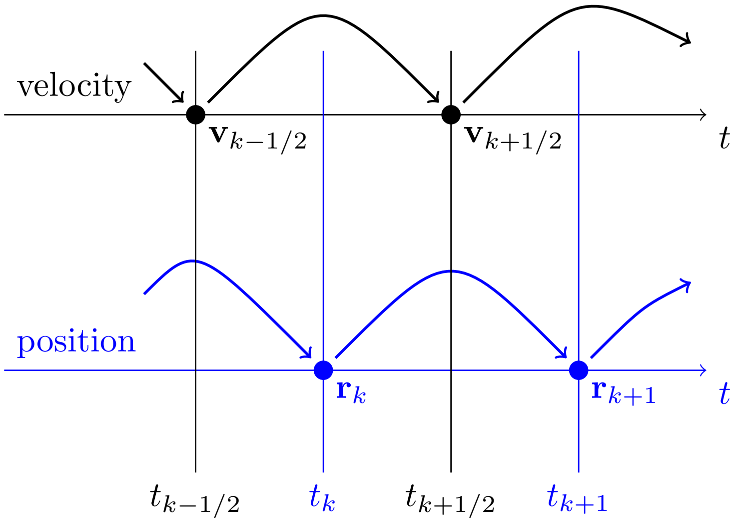

Figure 4.2: Scheme of the Leapfrog integrator

be constant.

The Boris scheme

In order to retain the discussed numerical properties, the provided expressions Eq. (4.8) and Eq. (4.6) for the Leapfrog scheme must be modified when a magnetic field is considered in the Lorentz force:

$$\mathbf{F} = \frac{q}{m}(\mathbf{E} + \mathbf{v} \times \mathbf{B}). \tag{4.10}$$

Under the aforementioned assumption of electrostatic PIC, the contribution of the self-induced magnetic field is neglected in Eq. (4.10). This is justified considering that the current densities produced by the charge carriers are not sufficient to produce a significant magnetic field. Hence, the quantity $\mathbf{B}$ in Eq. (4.10) represents *external* magnetic fields, such as the static radial magnetic field used to magnetically confine the electrons in $\mathbf{E} \times \mathbf{B}$ devices.

When in presence of a sufficiently strong magnetic field, the charged particles are said to be *magnetized*. In this case, the particles describe a helix motion along the magnetic field lines, which can be described with a circular motion around an instantaneous center of gyration (guiding center). The magnitude of the resulting angular velocity is commonly called cyclotron frequency, and writes as:

$$\omega_c = \frac{|q|B}{m}, \tag{4.11}$$

where $|q|$ and m are the considered particle charge and mass, and B the magnetic field magnitude. As can be noticed, ω_c is directly proportional to B, but also depends on the charge to mass ratio of the given particle. Hence, the electrons are more easily magnetized than the ions. The radius of the circular orbit (also known as gyroradius) is given by:

$$r_c = \frac{mv_\perp}{|q|B}, \tag{4.12}$$

where $v_\perp$ is the tangential velocity of the charged particle along the orbit described around the magnetic field lines. If, for a given specie, r_c is considerably larger than the characteristic length of the considered physical domain, i.e., $r_c \gg L_0$, that specie can be considered unmagnetized. The ions in a Hall thruster constitute a classic example of such a physical condition, as the magnetic field intensity is specifically selected to magnetize the electrons, while leaving the ions unmagnetized. From a modeling perspective, the cyclotron frequency is an important parameter, as it yields a criteria that can be used to determine if collisions must be modeled. In general, indeed, the requirement for a *collisionless* plasma is that the average time between collisions must be greater than the cyclotron period [6].

The so-called *Boris* method [109, 110] extends the Leapfrog method for the case of magnetized particles, by splitting the integration in 4 distinct parts. Starting from the particle velocity at time instant $k - 1/2$, the new velocity $\mathbf{v}^-$ resulting from the electric field acceleration over half a time-step is computed as:

$$\mathbf{v}^- = \mathbf{v}_{k-1/2} + \frac{1}{2}\frac{q_p}{m_p}\mathbf{E}\Delta t. \tag{4.13}$$

Then, half of the first half of the rotation due to the magnetic field is added to $\mathbf{v}^-$:

$$\mathbf{v}' = \mathbf{v}^- + \mathbf{v}^- \times \mathbf{t}, \tag{4.14}$$

where $\mathbf{t}$ is the rotation vector, that can be obtained as:

$$\mathbf{t} = \frac{1}{2}\frac{q_p}{m_p}\mathbf{B}. \tag{4.15}$$

So far, only half of the rotation has been computed. Effect of the second half-rotation is directly added to the *half-accelerated* velocity of Eq. (4.13):

$$\mathbf{v}^{+} = \mathbf{v}^{-} + \mathbf{v}' \times \mathbf{s}, \tag{4.16}$$

where $\mathbf{s}$ is obtained from a scaling of the rotation vector $\mathbf{t}$, such that the magnitude of the velocity is preserved:

$$\mathbf{s} = \frac{2\mathbf{t}}{1+\mathbf{t}^2}. \tag{4.17}$$

Finally, the contribution of the second half-acceleration is added to the velocity v^+ obtained with Eq. (4.16):

$$\mathbf{v}^{k+1/2} = \mathbf{v}^{+} + \frac{1}{2}\frac{q_p}{m_p}\mathbf{B}. \tag{4.18}$$

The described procedure allows to extend the aforementioned symplectic properties of the Leapfrog integrator for the case of a magnetized plasma, with the addition of a moderate computational burden.

In this overview, only the practical application of the Boris method has been presented for the sake of conciseness. Further details on its derivation can be found in [91] and [106].

4.1.2 Scattering and Gathering

In the PIC scheme, the particles are followed with a Lagrangian approach, and their position and velocities are are defined in the continuum space. However, for several reasons that will be discussed in this section and the following ones, the use of a spatial grid has become customarily in this kind of computer codes. While the particles move freely in the cells, the macroscopic quantities at the grid nodes (computed from the particles positions and velocities) are employed for the evaluation of fields and particle interactions.

In particular, charge densities at the grid nodes are employed as the source term for the Poisson equation, yielding the electric field at each grid node. This is has two main advantages over calculating the Coulombian interaction between each pair of macro-particles. The first is computational efficiency, reducing the order of computer operations to be performed at each step from N^2 to $N\log(N)$ [105], where N is employed the number of macro-particles. Moreover, the interactions at small separation distances are automatically *smoothed*, eliminating the problems arising from the divergent character of the Coulomb interaction.

Weighting schemes

In order to compute the number density at each grid node, a criteria must be selected to *distribute* the particle quantities (such as their number, charge or speed) among the nodes bounding the cells in which the particles are located at a given time instant.

The first *weighting* technique that has historically been employed in this kind of simulations is the so-called *Nearest-Grid-Point* (NGP) weighting. With reference to Fig. 4.3a, macro-particles located within $\pm\Delta x/2$ from a $j-$th node are counted, and *scattered* (assigned) to the grid node. All macro-particles are multiplied by a unity weight. Hence, if N_j is the counted number of macro-particles, the nodal number density is obtained as:

$$n_j = \sum_{p=1}^{N_j} w_p/V_j, \tag{4.19}$$

where w_p is the $p-$th macro-particle specific weight and V_j is the $j-$th cell volume. For what concerns the *gathering* operation, the same electric field $\mathbf{E}_j$ computed at the $j-$th grid point is assigned to all particles within the cell.

The main advantage of this technique consists is its simplicity and computational efficiency, requiring no interpolation. However, referencing again to Fig. 4.3a, a particle traveling from cell $j-$ to cell $j+1$ causes an instantaneous jump in n_j and n_{j+1}. This behavior generates noise in the spatial and temporal distribution of the computed number densities and electric fields.

In order to overcome the discussed limitations of the NGP weighting scheme, a fist-order interpolation technique called *Cloud-In-Cell* (CIC) is commonly implemented in modern PIC codes. When employing the CIC technique, summarized in 4.3b, each particle contributes to the grid quantities of the two nearest nodes at its left and right, respectively. The physical value assigned to the nodes j and $j+1$ is proportional to the distance of the macro-particle from j and $j+1$. Hence, e.g., the density assigned to node j from an ensemble of N_j particles $\in [x_j, x_{j+1}]$ is:

$$n_j = \sum_{p=1}^{N_j} w_p d_p / V_j, \tag{4.20}$$

where d_p is defined as the distance separating the macro-particle p form the $j-$th grid node, normalized to the grid spacing:

$$d_p = \frac{x_p - x_j}{\Delta x}. \tag{4.21}$$

The CIC scheme offers substantial advantages with respect to the described zero-order NGP technique, yielding smoother densities and forces. This result in a reduction of the artificial *heating* of the particles that inevitably takes place due to the charge density discontinuities created by the particles traveling between the grid cells.

As already mentioned, the weighting operation must also be performed to compute the force excerpted by the (electric and magnetic) fields on each particle. Both NGP and CIC schemes - as well as higher order schemes - can be used, under the condition that the same scheme is employed for both the scattering and gathering operations.

More details on the mentioned weighting schemes and a generalization to two and three dimensions can be found in [106] and [111].

4.1.3 Field Solution

As previously mentioned, one of the main parts of an electrostatic PIC code is constituted by the electric field solver. Indeed, the electrostatic assumption grants that the electric field is irrotational:

$$\boldsymbol{\nabla} \times \mathbf{E} = 0, \tag{4.22}$$

allowing to express the electric field by means of a scalar potential φ, defined such that $\boldsymbol{\nabla}\varphi$. In this way a Poisson problem is defined, whose solution yields the spatial distribution of the electric scalar potential at a given time-instant:

$$\boldsymbol{\nabla} \cdot (\epsilon_r \boldsymbol{\nabla}\varphi) = -\frac{\rho}{\epsilon_0} \tag{4.23}$$

The electric field $\mathbf{E}$, derived from the scalar potential, can then be interpolated at each particle position – together with the magnetic field $\mathbf{B}$ – to compute the Newton-Lorentz

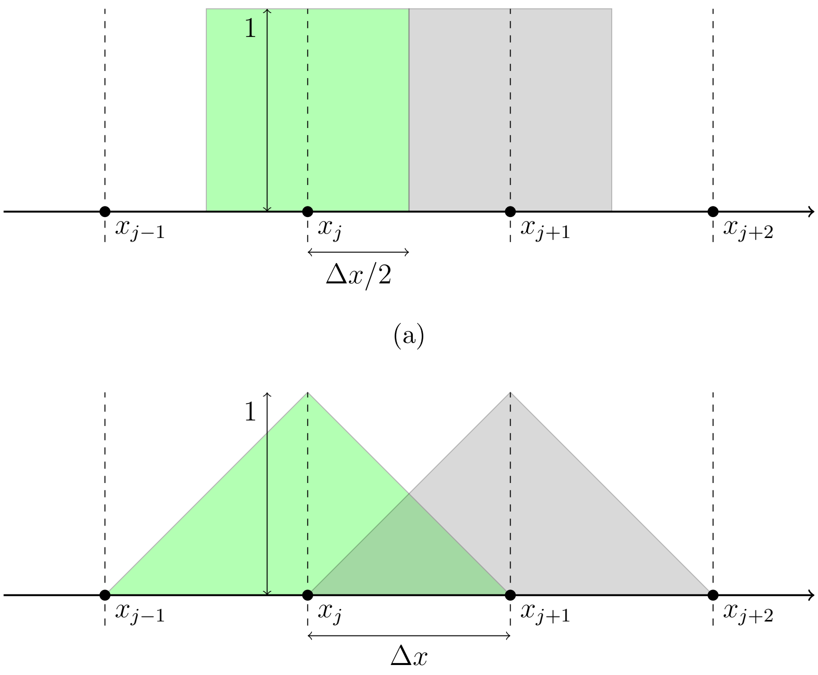

(a)

(b)

Figure 4.3: Schematic representation of the NGP (a) and CIC (b) weighting schemes, applied to a 1D spatial grid

force acting on each particle using Eq. (4.10).

The electrostatic problem defined in Eq. (4.23) can be solved performing a discretization of the Laplacian operator, leading to a (sparse) linear system of equations such as Eq. (2.37), described in Chapter 2.

The finite differences discretization of the Laplace operator in 1D yields a tridiagonal matrix, which can be efficiently solved with $\mathcal{O}(n)$ operations using the direct Thomas tridiagonal algorithm [112]. When 2D and 3D domains are considered, either direct or iterative solvers might be the most appropriate choice, depending on the problem size. Indeed, while direct solvers based on lower-upper (LU) decomposition or fast Fourier transform (FFT) are generally faster, they require more memory. Conversely, the performances of sparse methods such as the successive overrelaxation method (SOR) or the generalized minimal residual method (GMRES) are heavily affected by the choice of the employed pre-conditioner [113]. Nevertheless, iterative solvers can be particularly useful in the context of PIC codes, since the solution obtained at the $k-$th time-step can be used as the initial estimate of the new solution at instant $k + 1$ [114]. The benefits of this, however, strongly depend on fluctuations of the density evolving from one time-instant to the other [115].

Hybrid PIC codes

Alternatively to the previously described approach – based on the representation of both ions and electrons with super-particles – the kinetic approach can be restricted to the ions, while a fluid model can be employed for the electrons. Indeed, as discussed in Chapter 2, the fast dynamics of the electrons – under appropriate physical conditions – allow to assume that the electrons are thermalized and instantaneously respond to the electric potential changes caused by external sources or ions. These considerations allow to relate the spatial distribution of electron number density to the local electric potential via the Boltzmann relation (2.12), which results in a nonlinear Poisson problem described by the same formalism employed in Chapter 2. Since PIC codes are often applied to low-pressure physical scenarios, the resulting lower number densities (and voltages required to ignite the discharges) are extremely beneficial in the context of numerically solving the aforementioned nonlinear Poisson problem.

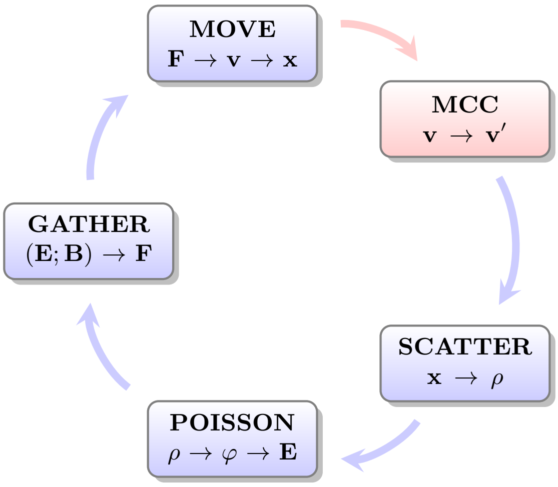

Figure 4.4: Typical scheme of a an electrostatic Particle-In-Cell code including a Monte Carlo Collision (MCC) module

4.1.4 Collisions

Up to this point, the provided description of the Particle-In-Cell methodology has been carried out assuming the absence of collisional phenomena. Nevertheless, many of the actual physical situations that can be modeled trough a particle approach are collision dominated. From the perspective of a PIC code, the collisional processes (appearing in the right-hand side of the Boltzmann equation) change the particle velocities and act as a source or sink for the different species. The different phenomena that must be modeled in this context are collisions between neutrals and both electrons (elastic scattering, excitation, ionization) and ions (scattering, charge exchange), as well as collisions between charged particles (Coulombian). In the case of molecular gases, such as air, electron-ion recombination can also significantly influence the considered plasma dynamics. The two main methodologies that are commonly implemented to account for collisions are the Monte Carlo Collision (MCC) and the Direct Simulation Monte Carlo (DSMC). Here only the first method – applied for the first times to the PIC method in [116,117] and later formalized in [118–121] – will be discussed, since it is employed in the code that will be described in Chapter 5.

The MCC method consist in providing a statistical description (in contrast with the rather deterministic nature of the PIC algorithm) of the collisional phenomena. As outlined in Fig 4.4, It is usually integrated in PIC codes before the evaluation of the nodal number densities. For a given particle p, the probability of undergoing a collisional event during the time Δt is obtained from the total collisional cross section σ_t (which depends on the incident particle kinetic energy ϵ_i), the target number density n_t and the relative velocity of the incident particle with respect to the target $v_{i,t}$:

$$P_p = 1 - \exp(-n_t \sigma_k(\epsilon_i) v_{i,t} \Delta t), \tag{4.24}$$

where ϵ_i is computed using the incident particle velocity, v_i, as:

$$\epsilon_i = \frac{1}{2} m v_i^2. \tag{4.25}$$

Since the considered macro-particle p can be involved in h different collisional process, the total collisional cross section σ_t appearing in Eq. (4.24) is obtained by summing the different cross sections associated to the h considered collisional processes:

$$\sigma_t = \sum_{j}^{h} \sigma_j(\epsilon_i). \tag{4.26}$$

Once the collision probability P_p is evaluated for each considered macro-particle, the number of collisions taking place during the selected Δt is obtained by comparing P_p with a random number, R_1. For the macro-particles having $P_p > R_1$, the comparison with a second random number R_2 is employed to determine which of the considered h collisional phenomena takes place, based on the relative weight of the partial cross section σ_t with respect to the total cross section σ_t. Finally, the incident species velocities and number densities are updated depending on the given collisional process (further details can be found in [121]), and the PIC cycle is continued using the post-collision physical values.

At this point, it is useful to remark that in the MCC approach the incident particles are assumed to collide with a target *cloud*, at least in its original formulation. Indeed – except from the number density – the properties of the target specie are not accounted in Eq. (4.24). This one of the main differences between the MCC and the aforementioned DSMC approach, in which the incident particles collide with the actual target population. The main consequence of this feature of the MCC is that the total momentum cannot be conserved. Conversely, the employment of the MCC over the DSMC allows to substantial savings in terms of computational performances.

5 Numerical simulations of a 20 W annular Hall thruster

5.1 Chapter Overview

This chapter is devoted to the description of the numerical simulation of two different operational modes of a 20W miniaturized Hall thruster, developed by the Gas Discharge Physics Laboratory of the Korea Advanced Institute of Science and Technology (KAIST). In the first section, a brief description of the hybrid Particle-In-Cell code employed for the simulations is provided. The main features and limitations of the employed numerical tools are described, focusing on the physical treatment of the anomalous cross-field electron transport. In the following section, the considered thruster geometry and global performances are discussed, together with the thruster simulation process performed with the *HALLIS* code. In particular, the results obtained from the application of two different methodologies for the modeling of electron anomalous cross-field anomalous transport are presented and compared with the measured thruster performances.

5.2 Numerical Methodology

HALLIS is a 2D axially symmetric code, developed by the GREPHE group at the LAPLACE laboratory (Toulouse, FR) for the simulation of Hall thrusters [122–125]. The numerical methodology implemented in *HALLIS* is a hybrid, i.e., a different approach is employed for the modelling of electrons and the heavy (neutral and ionic) species.

5.2.1 Ions and neutrals

The transport of the heavy species (neutrals, singly and doubly charged ions) is assessed using the Particle-In-Cell (PIC) methodology. As discussed in Chapter 4, the adoption of a kinetic approach (instead of a fluid one) for the ionic and neutral species presents the fundamental advantage of requiring no assumptions on the species velocity distribution function (VDF) $f = f(\mathbf{r}, \mathbf{b}, t)$ in the Boltzmann equation:

$$\frac{\partial f_s}{\partial t} + \mathbf{v} \cdot \nabla_{\mathbf{r}} f_s + \frac{\mathbf{F}}{m} \cdot \nabla_{\mathbf{v}} f_s = \left(\frac{\partial f_s}{\partial t} \right)_c , \tag{5.1}$$

Indeed, each employed macro-particle is characterized by a position $\mathbf{r}^*$ and a velocity $\mathbf{v}^*$ at the given time instant τ. Therefore, a macro-particle can also be seen both as an ensemble of real particles and as a single sample of the VDF (of the considered specie) in the phase space. In this spirit, an appropriate number of macro-particles can be used to provide an discrete representation of $f = f(\mathbf{r}, \mathbf{b}, t)$:

$$f(\mathbf{r}, \mathbf{b}, t) \approx \sum_p f_p(\mathbf{r}, \mathbf{b}, t) \tag{5.2}$$

The right-hand side of Eq. (5.1) represents the effect of collisions on the VDF. The modelled collisional phenomena include collisions between ions and neutrals - computed with with a Monte Carlo Collision (MCC-PIC) approach - as well as interactions with the thruster walls.

At each cycle of the PIC algorithm, neutral atoms are generated with random radial position between the internal and external radiuses of the thruster anode. The VDF of the neutrals is supposed to be Maxwellian, at a temperature of 500 K. While travelling towards the channel exit, the injected neutral atoms can collide against the thruster walls. *HALLIS* allows two different treatments of this phenomena, i.e., assuming specular or isotropic reflections of the neutrals. Modeling the reflections as specular correspond to assuming that the walls are perfectly smooth. In contrast, perfectly rough walls yield isotropic reflection. In both models, the magnitude of the particle speed is unchanged by the collision (differently from the angle). It is worth pointing out that the isotropic model allows the neutral particles to diffuse towards the anode, hence increasing the residence time of the gas propellant in the discharge channel. Throughout this work, only the isotropic model has been employed.

5.2.2 Electrons

Conversely, *HALLIS* employs a fluid approach for the physical description of the electrons. The main physical assumption justifying the adoption of a fluid description of electrons is that their VDF is Maxwellian along each magnetic field line. This is reasonable, as the electrons mean free path λ_{el} in Hall thrusters is considerably less than the characteristic length L_0 of these devices, thanks to the magnetic confinement. Assuming that the magnetic field is static[1], a scalar function λ can be defined from the magnetic field spatial distribution with the following expressions:

$$\frac{\partial \lambda}{\partial x} = rB_r, \tag{5.3}$$

$$\frac{\partial \lambda}{\partial x} = -rB_x \tag{5.4}$$

where B_r and B_x are the radial and axial magnetic field components, respectively.

The function λ monotonically increases from the anode until reaching the magnetic field line intersecting the cathode and can be used to define a quasi-1D grid such as the one shown in Fig. 5.1.

The first three moments of Eq. (5.1), i.e., the conservation equations for mass, momentum and energy are solved for the electrons, under the hypothesis of quasi-neutrality. Hence, the ionic and electronic number densities are equal in every point of the domain, except in the sheaths. The continuity equation is then expressed by means of the following expression:

$$\boldsymbol{\nabla} \cdot \boldsymbol{\Gamma}_e = Nnk_i - \frac{\partial n}{\partial t} = \boldsymbol{\nabla} \cdot \boldsymbol{\Gamma}_i, \tag{5.5}$$

where $\boldsymbol{\Gamma}_e$ and $\boldsymbol{\Gamma}_i$ represent electron and ion fluxes, the latter of which is known at each time step thanks to the kinetic treatment of the heavy particles. In Eq. (5.5), N and n represent the neutrals and charged species number densities, respectively; k_i is the ionization rate coefficient, which depends on the mean electron energy ϵ. The product of these three terms gives the number of ions generated per unit of volume and time. At each time step, this physical contribution is modelled by introducing in the

---

[1] The current densities due to motion of the charged species are low enough to assume that the magnetic field coincides with the one produced by the external magnetic circuit.

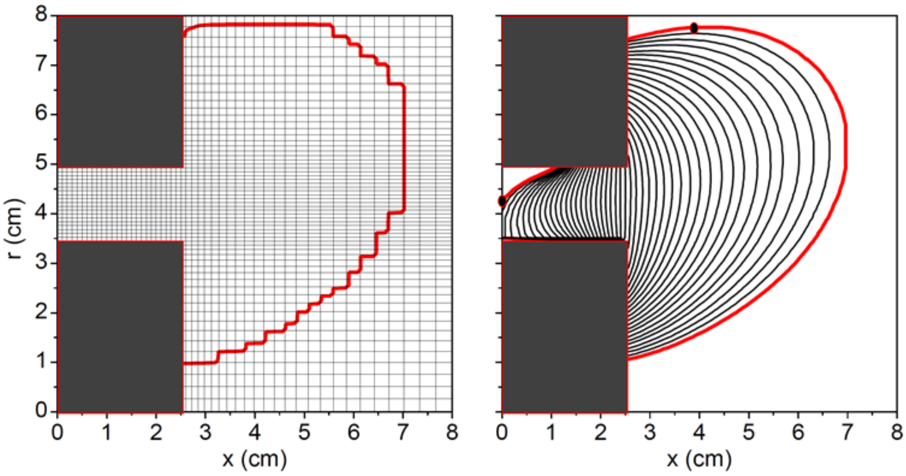

Figure 5.1: 2D (r-z) example of grid for ions and neutrals (left) and 1D (λ) grid for the electrons, from [6]. Both grids are delimited by the anode position and the magnetic field line intersecting the cathode

computational domain a corresponding number of macro particles representative of the generated ions.

The considered kinetic channels for the production of singly and doubly charged ions are depicted in Fig. 5.2a, along with the associated cross sections. These are the single [126] and double [127] ionization from the ground state, and the stepwise ionization of singly charged ions [128]. The generic ionization reaction rate k_i, representing the number of reactions per unit of time and volume associated with the given kinetic process, is obtained from the following expression:

$$k_i = \int_{-\infty}^{+\infty} f(v)\sigma v_r dv, \tag{5.6}$$

where $f(v)$ is the electrons velocity distribution function (supposedly Maxwellian), σ the cross section associated to the given kinetic process, and v_r the relative velocity of the electrons with respect to the ions. The latter is safely assumed to be coincident with the electron velocity, given the markedly lower dynamics of the heavy species. The obtained reaction rates are shown in Fig. 5.2b in the same energy range of the cross sections.

The first-order moment of the Boltzmann equation, i.e., the momentum continuity

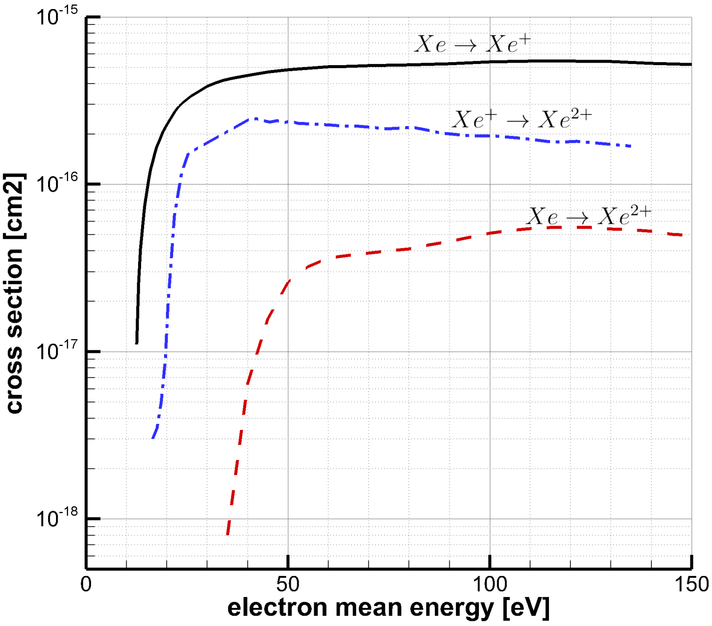

(a)

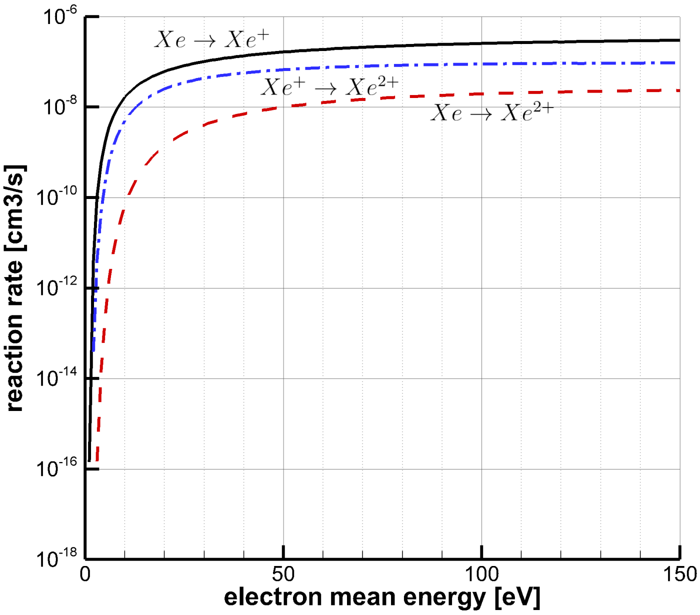

(b)

Figure 5.2: Singly and doubly charged Xe ions electron impact cross sections (a); corresponding rate coefficients (b)

equation, is expressed as:

$$\mathbf{\Gamma}_e = \mu \mathbf{E} n - \frac{2}{3e}\mu \nabla (n\epsilon), \tag{5.7}$$

where μ, $\mathbf{E}$ and ϵ represent the electron mobility, the electric field and the electron mean energy, respectively. As it can be noticed, this equation is written in a drift and diffusion form, meaning that changes of electron momentum are due to the force per unit of charge excerpted by an electric field (drift term) and gradients of electron mean energy (diffusion).

Finally, the second-order moment, i.e., the electron energy conservation, is expressed as:

$$\frac{\partial (n\epsilon)}{\partial t} + \frac{5}{3}\nabla \cdot (\mathbf{\Gamma}_e \epsilon) + \nabla \cdot \mathbf{q}_e = -e\mathbf{E} \cdot \mathbf{\Gamma}_e - Nn\kappa - nW, \tag{5.8}$$

where $\mathbf{q}_e$ is the heat flux. In the right-hand side of the energy equation, the first term represents the electron energy gain due to the electric field, while the two coefficients $\kappa = \kappa(\epsilon)$ and $W = W(\epsilon)$ multiplying the following terms represent electron energy losses due to collisions with neutrals and with walls.

Following Morozov's thermalized potential approximation, the force exerted by the electric field and the electron pressure gradient in Eq. (5.7) are assumed to be balanced along the magnetic field lines, giving:

$$\mu E n = \frac{2}{3e}\mu \nabla (n\epsilon) \tag{5.9}$$

Hence, under the assumption that the electron mean energy remains constant along the magnetic field lines, the integration of the previous expression along a magnetic field line yields a constant electric potential:

$$V^*(\lambda) = V(z,) - \frac{2}{3e}\epsilon(\lambda) \ln\left(\frac{n(z,r)}{n_0}\right). \tag{5.10}$$

This relation allows to obtain the electric potential at each point of the grid as a function of the electric potential $V^*(\lambda)$ and the electron mean energy $\epsilon(\lambda)$ along a given magnetic field line. These two quantities are constant (along a given line) and depend only on the scalar function λ.

Regarding the electric field computation, as anticipated *HALLIS* employs a quasi-neutral plasma model, i.e., the electric field is obtained from the current continuity equation $\nabla \cdot (\Gamma_i - \Gamma_e) = 0$ coupled with the electrons momentum conservation equation rather than the Poisson equation, and the physical effects of the sheaths are accounted by employing an analytical sheath model.

The adoption of a fluid approach for the physical description of the electrons grants a substantial advantage in terms of the code computational performances. Indeed, at each code iteration, the time step required for the stability of the macro-particles trajectories integration is no longer limited by the fast dynamics of the electrons. This allows to simulate relatively large time scales (up to milliseconds) in reasonable times using a sequential code implementation on a standard workstation. The drawback of such an approach is that appropriate expressions for the collisional phenomena appearing in the electron continuity and energy equations Eq. (5.7) and Eq. (5.8) must be provided.

5.2.3 Anomalous transport

Accurate modeling of the axial electron transport in the direction perpendicular to the magnetic field is a challenging task when fluid models are employed. The classical expression for the axial electron conductivity is defined as:

$$\mu_\perp = \frac{e}{m} \frac{\nu}{\nu^2 + \Omega_{ce}^2}, \tag{5.11}$$

where ν is the total electron momentum-exchange collision frequency and Ω_{ce} the electron cyclotron frequency. Unfortunately, this expression does not yield results in accordance with experimental measurements if the electron-neutral and electron-ion collisions are took into account exclusively [48]. In particular, the main discrepancies between simulations and experiments are found in the computed electron energy and in the electronic contribution to the discharge current. For these reasons, an equivalent electron collision frequency accounting for additional physical effects is employed instead of the classical one in *HALLIS*, defined as:

$$\nu = \nu_{e-n} + \nu_C + \nu_B + \nu_w, \tag{5.12}$$

where ν_{e-n} and ν_C are the electron-neutral and electron-ion Coulomb momentum exchange collision frequencies, respectively; ν_B accounts for instabilities and turbulence outside of the channel while ν_w represents the effects of interactions between walls and electrons. Regarding the anomalous contributions to the electron collision frequency, two different approaches are implemented in *HALLIS*.

The first among the two available approaches consist in using empirical expressions to obtain ν_B and ν_w. Inside the thruster channel, one of the main mechanisms responsible for the anomalous cross-field transport of electrons is the momentum-transfer collisions between the electrons and the thruster walls [129, 129, 130]. Sufficiently energetic electrons can pass the potential barrier created by the sheaths, colliding against the walls and losing a fraction of their kinetic energy, causing in turn a transport towards the anode. This collision frequency is estimated with the following expression:

$$\nu_w = \alpha 10^7 s^{-1}, \tag{5.13}$$

yielding the following associated electron mobility:

$$\mu_\alpha = \frac{m_e}{eB^2}\nu_\alpha. \tag{5.14}$$

The range of usual values for the empirical coefficient α is discussed in the following section.

Outside the thruster channel, the experimentally observed anomalous transport phenomena are usually associated with the so-called *anomalous Bohm diffusion*, where the cross-field transport is considered due to plasma fluctuations. The anomalous collision frequency associated with the Bohm diffusion is written as:

$$\nu_B = \frac{eB}{m_e}\frac{k}{16}, \tag{5.15}$$

leading to the following anomalous contribution to the electron mobility:

$$\mu_k = \frac{m_e}{eB^2}\nu_k. \tag{5.16}$$

Other physical mechanisms invoked as possible explanations to the observed transport outside the thruster channel include azimuthal plasma waves [131] and azimuthal turbulence phenomena [132].

As an alternative to the above presented approach based on empirical parameters, *HALLIS* allows to manually enforce the anomalous collision frequency along the axis of the thruster. This can be useful when experimental data on the considered thruster is available, allowing to adjust the anomalous frequency profile to match the measured physical quantities of interest.

The electron-wall collisions play a relevant physical effect on the electron momentum and mean energy losses. These effects are modelled by means of the methodology introduced in [133], based on a semi-analytical description of the sheath and the electron-sheath interactions.

5.2.4 Magnetic field calculation

The static magnetic field distribution produced by the thruster external magnetic circuit is computed using a freely available software, Finite Element Method Magnetic (FEMM) [134]. FEMM allows to define magnetostatic axisymmetric problems, solved using the Finite Element Method (FEM).

Considering the Ampère-Maxwell law:

$$\mathbf{\nabla} \times \mathbf{H} = \mathbf{J} + \frac{\partial \mathbf{D}}{\partial t}, \tag{5.17}$$

a magnetostatic problem is obtained by retaining the sole conduction current distribution, and using the constitutive relation $B = \mu H$:

$$\mathbf{\nabla} \times \mathbf{B} = \mu \mathbf{J}, \tag{5.18}$$

where μ is the magnetic permeability of the considered material. Thanks to the solenoidal nature of $\mathbf{B}$, the magnetic field can be expressed as the curl of a (magnetic) vector potential $\mathbf{A}$:

$$\mathbf{B} = \mathbf{\nabla} \times \mathbf{A}, \tag{5.19}$$

and the magnetic field distribution produced by the current density $\mathbf{J}$ can be obtained by solving the diffusion equation for the magnetic vector potential (MVP) over the considered physical domain:

$$\mathbf{\nabla} \times \left(\frac{1}{\mu} \mathbf{\nabla} \times \mathbf{A} \right) = \mathbf{J}. \tag{5.20}$$

It is worth highlighting that the azimuthal MVP component yielded by FEMM, A_θ, is scaled with respect to the radius in the following way:

$$A_s = 2\pi r A_\theta. \tag{5.21}$$

In *HALLIS*, the axial and radial components of the magnetic field are obtained from the following expressions, employed for the axial and radial components, respectively:

$$B_z = \frac{1}{2\pi r}\frac{\partial A_s}{\partial r}, \tag{5.22}$$

$$B_r = -\frac{1}{2\pi r}\frac{\partial A_s}{\partial x}. \tag{5.23}$$

Figure 5.3 shows the magnetic field obtained for the KmHT-20 thruster. A few relevant features of this magnetic configuration can be noticed. Firstly, the magnetic field is mostly radial, with maximum value in in correspondence with the thruster channel exit. Also, the magnetic field lines are convex in the internal part of the thruster, forming a so-called convex-lens structure. This, along with the previously mentioned predominance of the radial magnetic field component, is a distinctive characteristic of annular thrusters [100]. The shape of the magnetic field lines in proximity of the channel is particularly relevant as these latter are approximately coincident with the electric potential iso-lines. Because of this, the described convex property of the magnetic field lines indirectly ensures that the electric field will excerpt a focalizing effect towards the positively charged ions exiting from the channel.

As can be observed in Fig. 5.3d, the magnetic field starts to increase after 10 mm from the closed end of the thruster channel. For this reason, the anode position for all the performed simulation has been displaced 10 mm towards the channel exit, under the assumption that no relevant gas ionization can take place without the electron confinement excerpted by the magnetic field.

5.3 Simulation Results

This section is concerned with the numerical simulation of the KmHT-20 annular Hall thruster. Depending on the gas flow rate and the anode voltage, two different operational modes have been observed [135], that will be referred to as mode A and mode B, respectively.

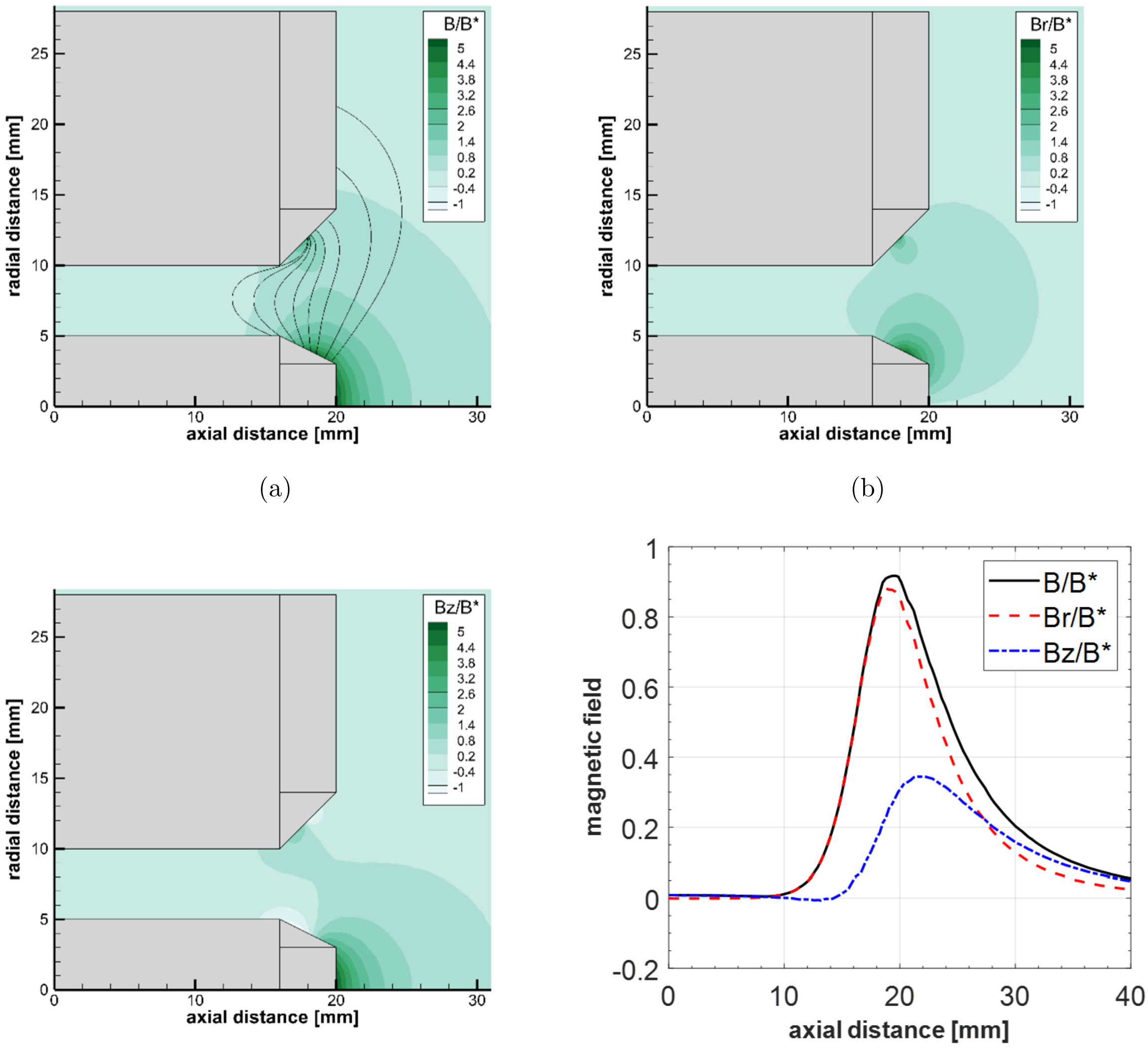

(a) (b)

(c) (d)

Figure 5.3: KmHT-20 magnetic field; (a) magnetic field magnitude and magnetic field lines in proximity of the channel exit; (b) magnetic field radial component; (c) magnetic field axial component; (d) magnetic field along the channel axis

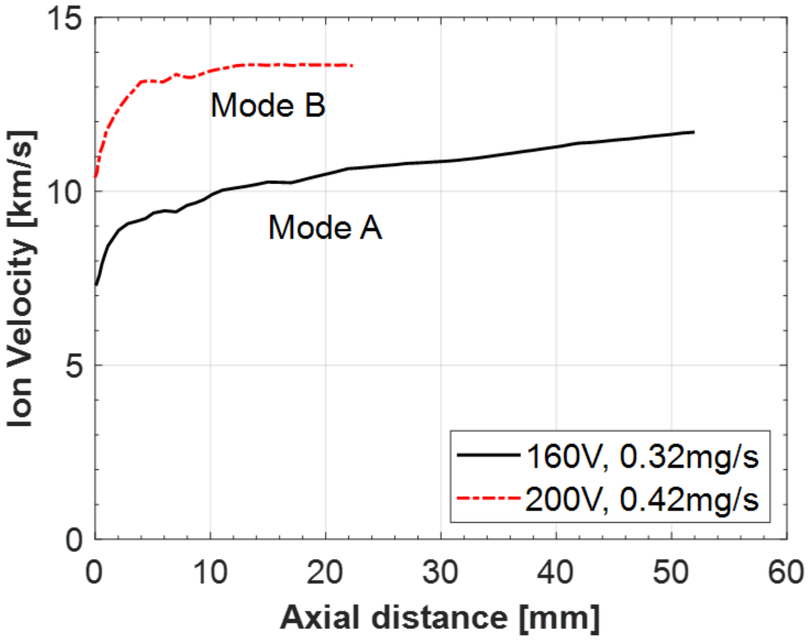

Figure 5.4: Mean ion velocity outside the KmHT-20 channel exit, obtained with LIF measurements (courtesy of KEPL research group)

The operational mode A is observed when low gas flow rates ($\dot{m}$ <0.37 mg s^{-1}) are employed. With respect to mode B, mode A is associated with higher values of plume divergence +18 % and discharge current. Specifically, the observed increase in the discharge current is mainly due the electronic current component +30 % , while the ionic current increase is only +5 %. Hence, when the thruster is operated in mode A significantly lower values of anode efficiency are obtained.

In addition, higher fractions of multiply charged Xe ions are observed in mode A +30 % with respect to mode B (+15 %). The measured Ion Energy Distribution Function (IEDF) in mode A exhibits a larger Full Width at Half Maximum (FWHM) and, as can be observed in Fig. 5.4, the ions acceleration outside the channel exit takes place over a considerably longer region.

Based on the available experimental data, two flow rate/anodic voltage settings have been selected as representative of the two observed operational modes. In particular, a Xe injection of 0.32 mg s^{-1}with anode voltage set to 160 V corresponds to mode A, while operational mode B is observed when the flow rate is increased to 0.42 mg s^{-1}, and the anode voltage to 200 V.

Table 5.1: Target experimental results for Mode A and Mode B

Mode	**[mg/s]**	**[V]**	**P [W]**	**$\mathbf{I_d}$[A]**	**T [N]**	**Isp [s]**	**Anode Eff [-]**
A	0.32	160	58.4	0.365	3.10E-03	820	0.21
B	0.42	200	58	0.27	3.30E-03	840	0.22

Table 5.2: Settings employed for the performed simulations

Physical quantity	**Value**	**Unit of measurement**
Anode Voltage	160/200	V
Xe flow rate	0.32/0.42	$\mathrm{mg\,s^{-1}}$
Backpressure	1×10^{-3}	Pa
Neutral gas temperature	500	K
Neutrals/Walls collision model	Isotropic	-
Electron energy at anode	2	eV
Electron energy at cathode	5	eV

For each of the two selected flow rate/anodic voltage configurations, several target thruster macroscopic performances have been selected from the experimental data, to be compared with the ones yielded by the *HALLIS* code. These include the discharge current (given by the sum of the ionic and electronic currents, $I_d = I_e + I_i$), the thrust, the specific impulse and the anode efficiency. The considered figures of merit, along with their measured values for the two operational modes are reported in Table 5.1.

Table summarizes the physical quantities and the settings that have been employed as input data for the simulations, as well as their numerical value. All the reported quantities have been kept constant throughout the different numerical simulations that will be discussed in the following sections.

5.3.1 Mode B

This section deals with the simulation process of operational mode B. Two different approaches have been adopted, following the two different treatments of the anomalous transport implemented in the *HALLIS* code. Firstly, the results of a parametric analysis performed by exploring a range of different values for the empirical electron transport parameters (described in the previous section) are reported and discussed. Then, the results obtained by manually enforcing the anomalous transport collision frequency for the electrons along the thruster channel axis are shown and compared to the previous approach.

Empirical anomalous collision frequency

Using the *HALLIS* code, several parametric simulations have been carried out to test the computed thruster macroscopic performances for different values of the empirical coefficients α and k_b described in the previous section.

The coefficient α accounts for the electron momentum losses inside the thruster channel. This coefficient was found to be realistic in the range $\alpha \in [0.1 - 1]$ in a previous study on the well-known SPT-100 thruster [136]. In this work, the range of α has been extended to $[0 - 4]$. This is justified by the fact that the KmHT-20 channel has a width of 5mm, while the SPT-100 channel measures 15mm. Because of this, the walls surely play a more prominent physical role for the KmHT-20 thruster geometry. For what concerns ν_B – the anomalous collision frequency outside the channel due to turbulent effects – the coefficient k_b in the expression for ν_B (Eq. (5.12)) was varied in the range $[0 - 1]$.

Figure 5.5 shows the computed thrust (a), discharge current (b) and anode efficiency (c) obtained for α and k_b varying in the discussed ranges, respectively. For all the performed simulations, the anode voltage has been set to 200 V, and the Xe flow rate to 0.42 $\mathrm{mg\,s^{-1}}$. All the other employed physical quantities, along with the boundary conditions for the voltage and the electron mean energy, can be found in Table 5.2.

Looking at the computed thrust, discharge current and efficiency, it can be noticed that the sharpest variations are obtained when either one of the two empirical parameters α and k_b is increased from 0 to roughly 1/4 or its explored range. Above these values ($\alpha > 1,\ k_b > 0.2$), the thruster performance dependence on the empirical transport parameters decreases significantly. This finding is consistent with the results obtained in previous studies performed on the consolidated SPT-100 geometry [136], and shows that – once a sufficiently large cross-field electron transport is reached – the macroscopic performances are mainly established by the thruster geometry, magnetic configuration and operational conditions (such as flow rate and anode voltage).

Compared to the thrust and discharge current, the computed anode efficiency exhibits a different behaviour when the anomalous transport associated with the channel walls is increased. Indeed, for $\alpha > 2$ the efficiency starts to progressively decrease. This feature can be explained recalling that the discharge current is constituted by a ionic and an electronic component ($I_d = I_i + I_e$), but only the ionic component contributes to the thrust, i.e., the numerator of the anode efficiency in Eq. (1.4). The results show that, when $\alpha > 2$, the increase in I_e due to the anomalous transport is not accompanied by a corresponding increase of I_i, leading to the observed decrease of the thruster anode efficiency. The described physical behaviour of the two components of the discharge current can be verified in Fig. 5.5d, where the ratio between the ion current and the total current decreases for increasing values of the electron anomalous transport inside and outside the thruster channel.

The macroscopic thruster performances yielded by two different pairs of values for α and k_b (denoted as CASE I and CASE II here onward) are compared to the experimental measurements in Table 5.3. CASE I ($\alpha = 3, k_b = 0.25$) corresponds to the simulation result with the best agreement in terms of computed discharge current (and power). Case II correspond to the result that minimizes the sum of the relative differences in terms of computed discharge current (I_d), thrust (T) and anode efficiency (η) with respect to the measurements:

$$\text{CASE I} = min(\Delta I_d), \tag{5.24}$$

$$\text{CASE II} = \min(\Delta I_d + \Delta T + \Delta \eta), \tag{5.25}$$

where, e.g.:

$$\Delta I_d = \frac{|I_d^* - I_d|}{I_d^*}. \tag{5.26}$$

In the previous expression, I_d^* and I_d are the measured and computed values of discharge current, respectively.

The comparison between the measurements and the results obtained for CASE I and CASE II in Table 5.3 shows a reasonable agreement, particularly for what concerns the thrust (hence specific impulse) and the discharge current. Conversely, a larger disagreement is observed for both considered cases in the obtained values for the anode efficiency. Overall, the global thruster performances obtained with the presented analysis appear to be compatible with the available experimental data.

Nevertheless, the additional information provided by the LIF measurements does not

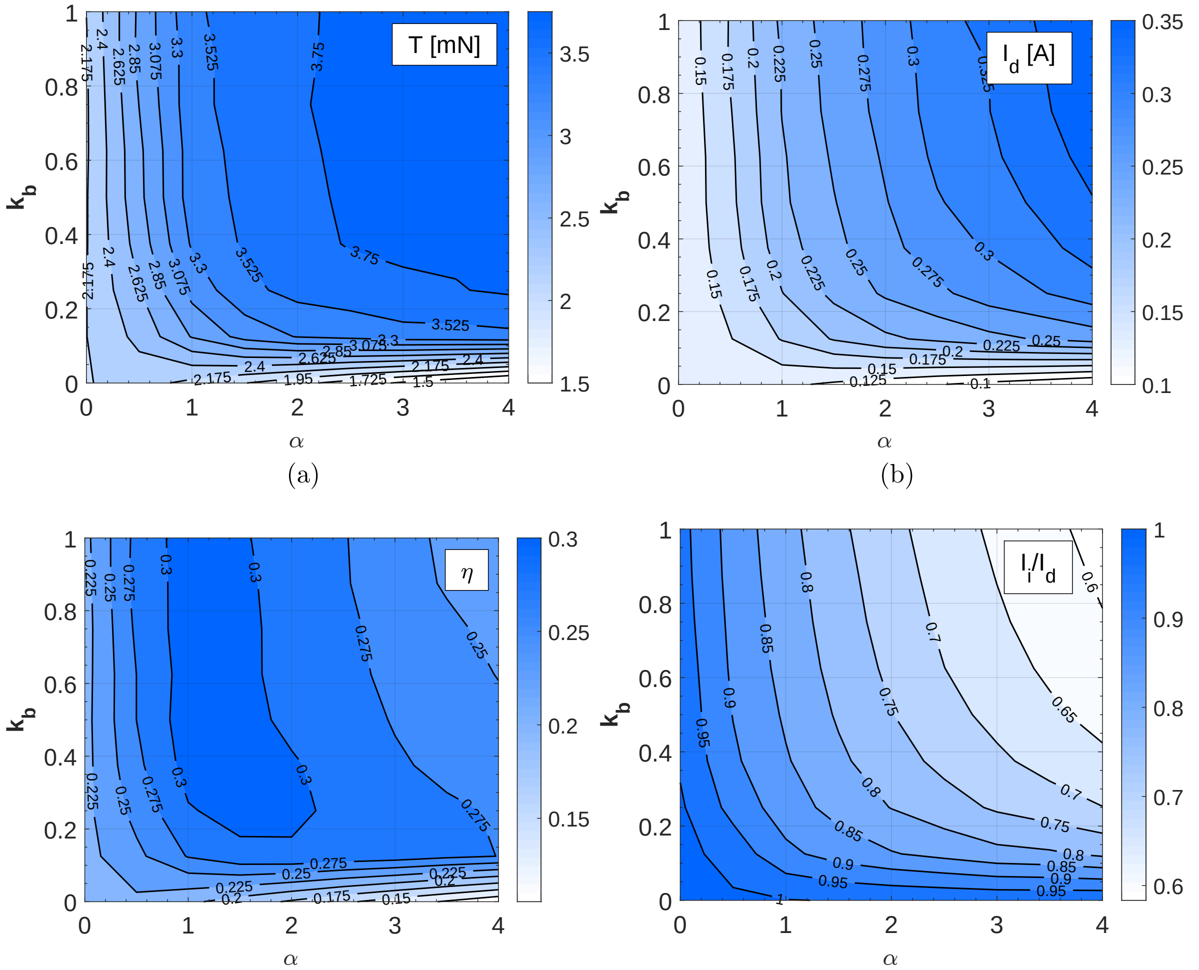

(a) (b) (c) (d)

Figure 5.5: Mode B (200V; 0.42 mg s^{-1}) – computed values of thrust (a), discharge current (b), anode efficiency (c) and ratio between the ion and electron current at the cathode (d) as a function of empirical parameters α (wall momentum losses) and k_b (Bohm anomalous transport)

Table 5.3: Comparison between the measured (EXPER) and computed (*HALLIS*) thruster performances for operational mode B, using empirical parameters for the electron anomalous transport

Mode B	α	$\mathbf{k_b}$	**P [W]**	$\mathbf{I_d}$ **[A]**	**T [mN]**	**Isp [s]**	**Anode Eff [-]**
EXPER	-	-	58	0.29	3.3	840	0.22
HALLIS – CASE I	3	0.25	57.4	0.29	3.74	908	0.29
HALLIS – CASE II	4	0.125	52.3	0.26	3.47	842	0.27

match with the results obtained with the described empirical description of the anomalous collisional phenomena. In order to illustrate this, the measured values of mean ion velocity along the thruster channel centreline ($v_{i,LIF}$) are plotted against the results of CASE I and CASE II in Fig. 5.6a and Fig. 5.6c, respectively. As one can see, in both cases the obtained ion velocity is not compatible with the LIF measurements. The different ion velocities obtained in Figs. 5.6a and Fig. 5.6c are due to a different electric potential distribution along the channel length. Considering CASE I, a larger part of the potential drop takes place inside the channel. This leads to a spatial displacement of the electric field maximum towards the internal part of the thruster, resulting in an increased ions velocity at the thruster exit.

The two different voltage drop profiles observed in CASE I and CASE II are linked to the corresponding electron anomalous collision frequencies, reported in Figs. 5.6b and 5.6d, respectively.

Comparing the two plots, the electron-neutral and electron-ion (Coulomb) frequencies (ν_C) are roughly equal. This result is expected, considering that the neutrals flow rate and backpressure are the same for the two cases. The small differences in the obtained thrust and anode efficiency allow to assume that the achieved ionization rates are similar, justifying the observed similarity in the Coulomb collision distribution along the channel axis. While the Coulomb collisions do not constitute a relevant contribution to the total collision frequency ($\nu_C \ll \nu$), the electron-neutral collisions become predominant in the appurtenances of the anode, where ionization is low.

Conversely, moving from the anode towards the ionization zone and the channel exit, the anomalous terms of the electron collision frequency rapidly become dominant over the described classical effects, due to the progressive decrease of the neutral gas density. With reference to Figure 7 (b) and (d), the total collision frequency ν is substantially different between CASE I and II – especially outside the channel exit – due to the different values of the empirical parameters α and k_b. The ratio α/k_b plays a prominent role, as it directly influences the plasma conductivity discontinuity that generates the potential drop. Decreasing the value of this ratio (such as in CASE I with respect to CASE II) leads to a displacement of the voltage drop inside the channel, ultimately changing the relative positioning of the ionization and acceleration regions. The described dependence of the voltage drop repartition from the α/k_b ratio is consistent with the numerical study performed in [136] for a full-scale SPT-100 Hall thruster, and can be verified in Fig. 5.7

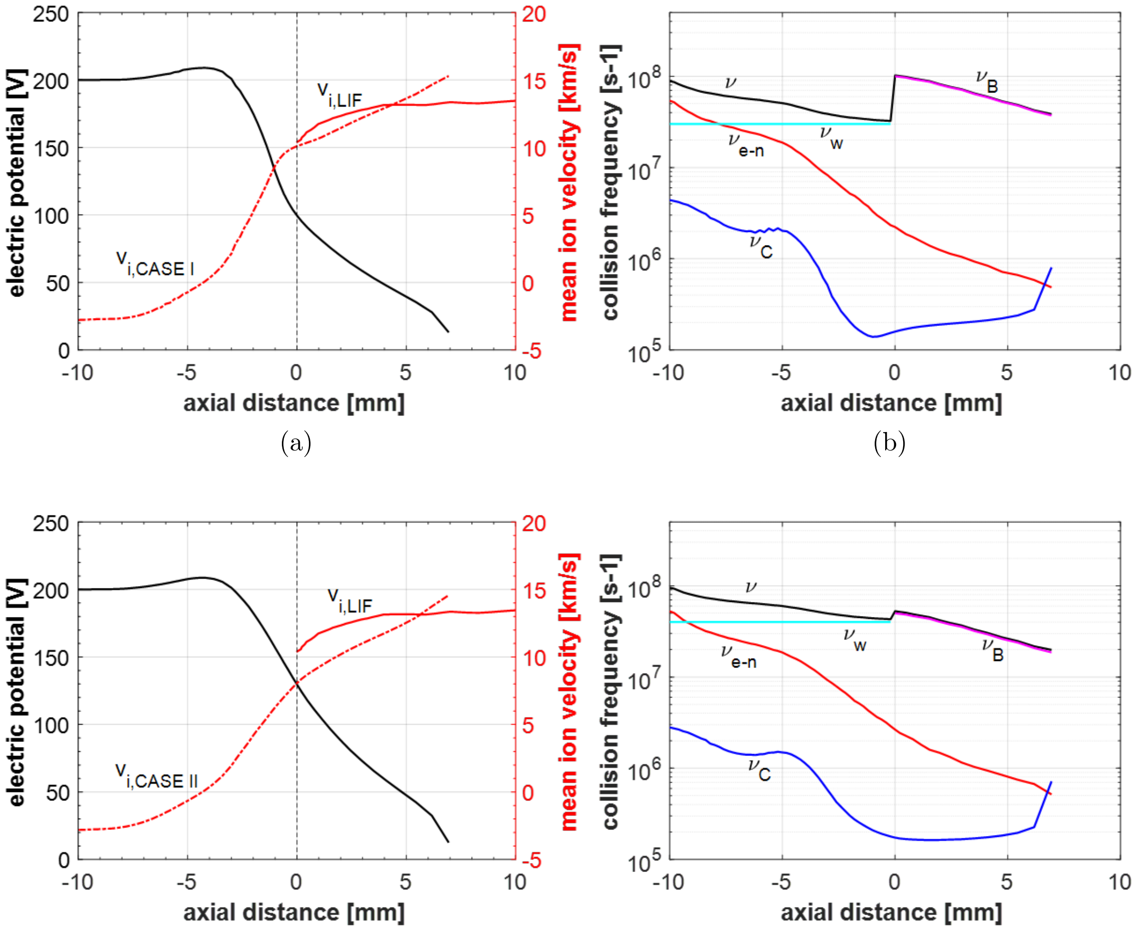

(a) (b)

(c) (d)

Figure 5.6: (a,c) electric potential and mean ion velocity along the thruster channel axis, comparison between the computed velocities and the LIF measurements; (b,d) electron collision frequency along the channel axis; (a,b) refer to CASE I ($\alpha = 3,\ k_b = 0.25$), (c,d) correspond to CASE II ($\alpha = 4, k_b = 0.125$); the black, dashed line in (a) and (c) marks the channel exit

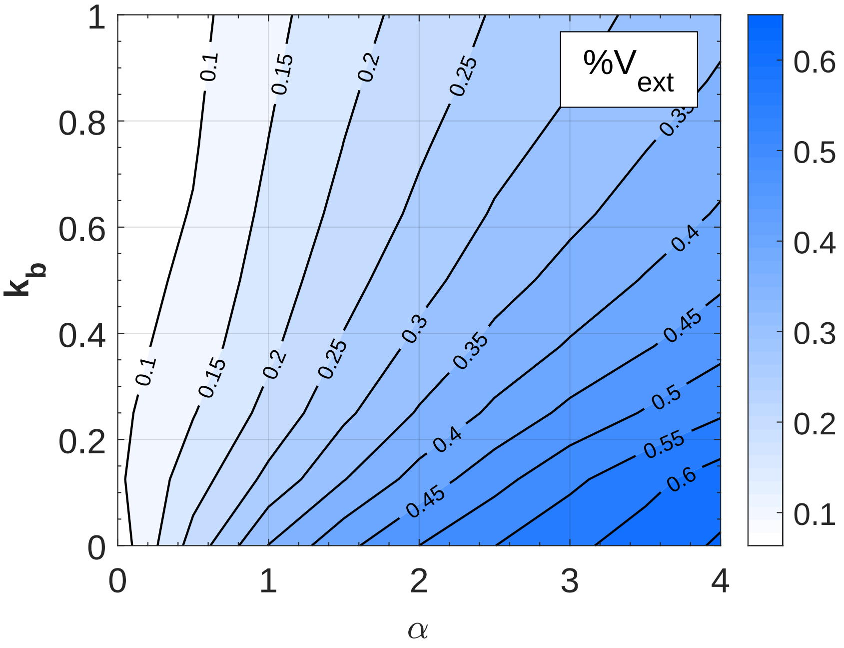

Figure 5.7: Ratio between the voltage drop after the channel exit and the total voltage drop $V_{ext}/(V_{ext} + V_{in})$ as a function of empirical parameters α and k for operational mode B

in the same range of α and k_b employed in Fig. 5.5.

The comparison of the presented results with the LIF measurements leads to the conclusion that, although capable of roughly reproducing the macroscopic thruster performances, the modeling approach employed so far does not allow to fully capture the physical features of the considered thruster (operated in Mode B). In addition, the provided discussion highlights the intimate dependence of the gas ionization and acceleration mechanisms from the anomalous electron collision frequency (and associated mobility). In the following sections a different approach is adopted to account for the effects of the anomalous electron collision frequency.

Enforced anomalous collision frequency profile

In this section, a different methodology has been applied to the study of the same operational mode (B) described in the previous section. The adopted strategy consisted in enforcing the anomalous electron collision frequency profile along the axis of the thruster, aiming to obtain a simulated average velocity profile of the ions (v_i) consistent with the LIF measurements shown in Figure 5. With reference to Eq. (19), the two

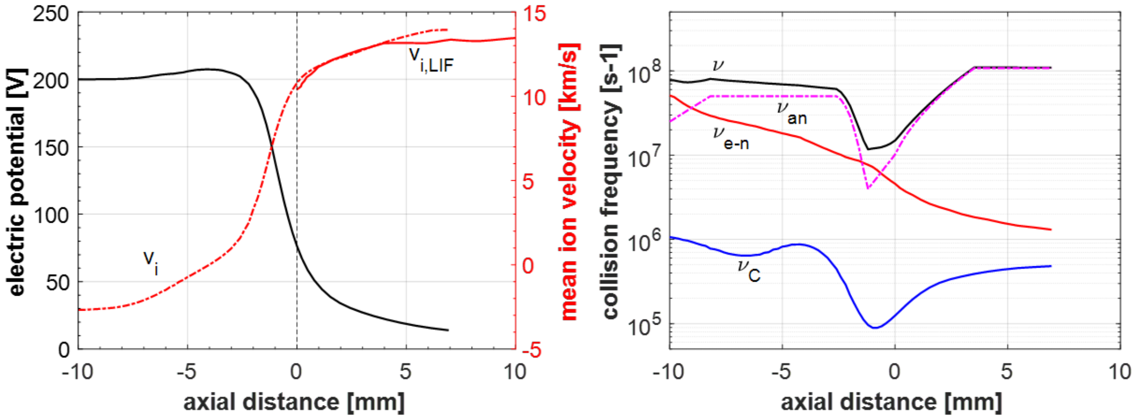

(a) (b)

Figure 5.8: (a) electric potential and mean ion velocity along the thruster channel axis, comparison between the computed velocities and the LIF measurements; (b,d) electron collision frequency enforced along the channel axis

anomalous contributions inside and outside the channel exit (ν_w,ν_B) are unified into a single contribution, denoted here onward as ν_{an}. For the sake of simplicity, the value of ν_{an} enforced at a given point is extended from the channel axis to the walls, so that the anomalous collision frequency depends only on the axial position.

Starting from the best-fitting anomalous collision frequency profile obtained with the methodology based on empirical parameters, the enforced collision frequency has been iteratively changed until a satisfactory agreement with the measured mean ion velocity has been reached. The obtained velocity is plotted against the measurements in Fig. 5.8a, while Fig. 5.8b shows the associated classical and anomalous contributions to the momentum-exchange frequency.

As it can be observed, the enforcement of the anomalous collision frequency profile ν_{an} allowed to accurately match the experimental results, especially in the first 5 mm after the channel exit. The observed discrepancy between the computed mean ion velocity (v_i) and the LIF measurements ($v_{i,LIF}$) after 5 mm from the channel exit is due to an intrinsic limitation of the employed methodology, and will be discussed in more detail in the next section.

As anticipated, Fig. 5.8b shows the different (classic and anomalous) contributions to the total momentum-exchange collision frequency of the electrons (ν). Starting from the classic terms, coherently with the results in Fig. 5.6, the electron-ion momentum exchange collision frequency (ν_C) is at least one order of magnitude lower compared to ν_{e-n} (collisions between electrons and neutrals inside the channel). Hence, ν_{e-n} is the dominant classical contribution to the total collision rate. The same is valid in the anodic zone, where the density of neutrals is particularly intense. Comparing the ν_{e-n} term in 5.8b with the results in Figs. 5.6b and 5.6d, a noticeable increase can be noticed in the results in 5.8b. This feature can be explained considering that – for this latter case – a considerably lower ionization of the neutral gas is achieved, leading to a higher availability of neutral atoms towards the end of the channel, which results in an increase of ν_{e-n}. Nevertheless, the inefficiency of the ionization mechanism ultimately results in a general decrease of the main figures of merit of the thruster.

Focusing on the anomalous contribution ν_{an}, a different trend can be observed comparing Fig. 5.8 to the results of Figs. 5.6 and 5.5, obtained using the empirical parameters α and k_b. Thanks to the manually enforced contribution provided by ν_{an}, the total anomalous frequency in Fig. 5.8b is higher than its counterparts in Figs. 5.6b and 5.6d at each point along the thruster channel axis, except for the appurtenances of the anode and in the high magnetic field region towards the end of the channel. The decrease of anomalous collision frequency in the latter area ensures that the potential drop is not displaced too deeply into the discharge channel due to the gradient of electrical conductivity between the inside and the outside.

Despite the good agreement obtained in Fig. 5.8 between v_i and $v_{i,LIF}$, the achieved performances in terms of thrust, specific impulse, discharge current and anode efficiency are not compliant with the experimental measurement. For this reason, the above described procedure – consisting of enforcing the axial anomalous collision frequency until reaching $v_i = v_{i,LIF}$ – was iteratively repeated with the additional constraint of matching I_d and I_d^*, the computed and measured discharge currents. The results achieved by enforcing ν_{an} such that $v_i = v_{i,LIF}$ and $I_d = I_d^*$ are reported in Fig. 5.9. In addition, a quantitative comparison between the measured thruster performances and the results obtained enforcing ν_{an} with and without the additional constraint on I_d can be found in Table 5.4.

Comparing Fig. 5.8 and Fig. 5.9, a similar axial distribution of the electric voltage drop is obtained by enforcing two different collision frequency profiles. However, except for the high-**B** zone located at the channel end, the anomalous frequency enforced in

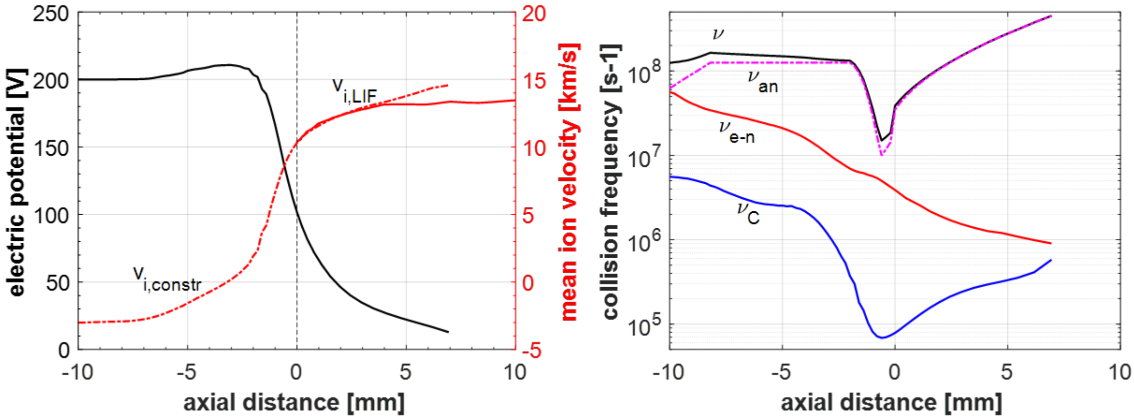

(a) (b)

Figure 5.9: (a) electric potential and mean ion velocity along the thruster channel axis, comparison between the computed velocities and the LIF measurements for the same conditions of Fig. 5.8, with the additional constraint of $I_d = I_d^*$; (b) employed anomalous collision frequency values along the channel axis (ν_{an})

Table 5.4: Thruster performances of the KmHT-20 AHT with V_a =200 V, flow rate = 0.42 mg s^{-1}. The three rows correspond to the experimental results and the *HALLIS* results obtained using the two anomalous collision frequency profiles of Fig. 5.8b and 5.9b, respectively.

Mode B	**[V]**	**P [W]**	$\mathbf{I_d}$ **[A]**	**T [N]**	**Isp [s]**	**Anode Eff [-]**
EXPER	200	58	0.29	3.30E-03	840	0.22
HALLIS	200	22.4	0.11	1.55E-03	377	0.13
HALLIS CONSTR	200	61.0	0.31	3.15E-03	764	0.19

Fig. 5.9b is higher than its counterpart in Figure 9 (b). The increased collisionality inside the channel causes the growth of I_d reported in Table 5.4.

For the above discussed reasons, increasing only the momentum-transfer due to the walls would lead to a displacement of the voltage drop outside the channel. Hence, the increase of ν_{an} inside the channel is balanced by a corresponding increment of ν_{an} outside the thruster open end.

In order to clarify the physical consequences of the different numerical treatment of the anomalous electron collision frequency performed in this section, the ion energy distribution function (IEDF) at the cathode line is shown in Fig. 5.10 for three different cases. The results obtained using the empirical parameters corresponding to CASE I and CASE II (Fig. 5.5) are indicated with a solid black line and a dashed black line, respectively. The two cases feature different values of the α/k_b ratio. For both cases low and high energy peaks can be observed, which can be correlated to the presence of low-frequency oscillations and doubly charged ions, respectively. In addition, another high peak of the IEDF can be noticed close to 200 eV, corresponding to the anode voltage. The full width at half maximum (FWHM) of the distribution is significantly lower for CASE I, where a lower α/k_b ratio is employed. This feature is expected, as in CASE II the voltage drop occurs over a longer distance, generating a lower, extended electric field.

The same reasoning can be applied to the IEDF yielded by the enforced anomalous collision frequency profile of Fig. 5.9b, depicted in green. Indeed, in this case the voltage drop occurs on a shorter distance with respect to CASE I, causing the observed narrowing of the IEDF in proximity of 200 eV.

The thruster performances reported in Table 5.4 show that – along with the discharge current – all the other figures of merit have substantially changed when the additional constraint on I_d has been enforced. The simulated values of thrust, Isp, and anode efficiency are well compatible with the corresponding measures performed on the KmHT-20 thruster. This also means that, thanks to the increased electron momentum losses, a larger fraction of propellant is ionized inside the channel, generating a population of singly and doubly charged Xe ions. Fig. 5.11a shows the spatial evolution of the ionization term along the thruster channel axis, along with electron mean energy distribution. The latter exhibits its maximum value at the point where the radial magnetic field is highest, see Fig. 5.3b. The peak of the source term – for both single and double ions —

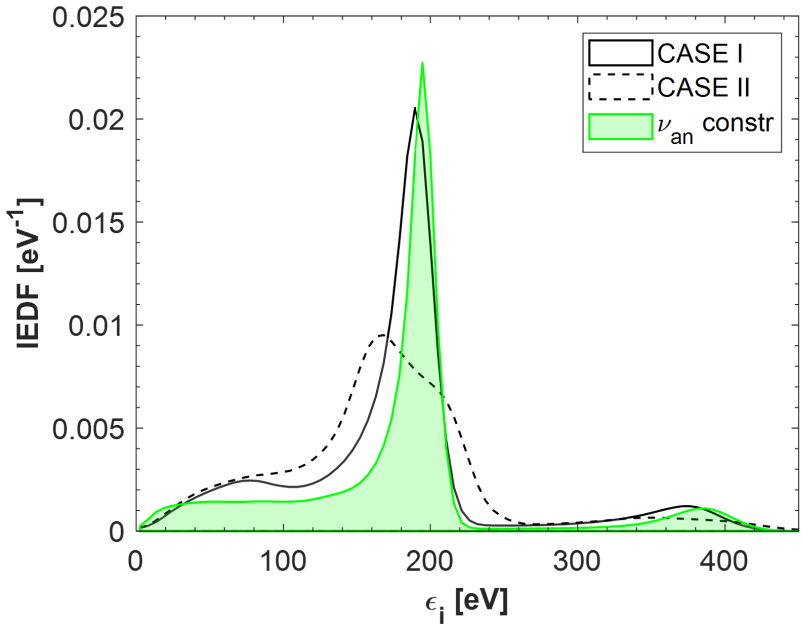

Figure 5.10: Ion energy distribution function computed at the cathode line; the black (solid and dashed) lines have been obtained with the empirical methodology described in the previous section, based on empirical coefficients for the anomalous electron transport; the green line correspond to the manually enforced anomalous frequency profile in Fig 5.9b

is displaced towards the inside of the channel with respect to the electron energy maximum, meaning that a satisfactory separation between the acceleration and ionization zone is reached. As expected, the main contribution to the generation of ionic species is given by single ions. This is due to the lower threshold energy (12eV) compared to processes involving double ions (32eV for $\mathrm{Xe} \longrightarrow \mathrm{Xe}^{++}$, and 21eV for $\mathrm{Xe}^{+} \longrightarrow \mathrm{Xe}^{++}$). For what concerns the multiply charged ions, it can be noticed that – despite a larger threshold energy required to produce a doubly charged ion from the ground state – the two considered kinetic channels yield a comparable contribution. Specifically, 56 % of the doubly charged ions current at the cathode line is produced from $\mathrm{Xe} \longrightarrow \mathrm{Xe}^{++}$ and the remaining percentage from $\mathrm{Xe}^{+} \longrightarrow \mathrm{Xe}^{++}$. This is due to the lower reaction rate of the double ionization from ground state being compensated by a higher availability of neutrals with respect to the Xe^+ ions necessary for the stepwise ionization process. The number density of the heavy species is depicted in Fig. 5.11b along the thruster channel axis.

One of the physical peculiarities associated with this kind of miniaturized thrusters is the presence of a higher doubly charged ions fraction with respect to full scale Hall thruster designs. Using the described numerical methodology, a 10.05 % doubly charged ions fraction current was observed in the results achieved with the additional constraint on I_d. This is compatible with the data reported in [137] for the annular Hall thruster configurations and with the results obtained in [138] for a different low power cylindrical Hall thruster. This means that the simulated kinetic processes and the range of electron mean energies obtained in the simulations are realistic.

Finally, the anomalous frequency profile ν shown in Fig. 5.9b was employed to compute the I-V characteristic of the thruster, by progressively changing the anode voltage from 160 V to 240 V while retaining the same flow rate. The results are depicted in Fig. 5.12, alongside the corresponding measured values for the discharge current. Unfortunately, the I-V characteristic does not show the same trend of the measurements. In particular, the model cannot predict the change of mode (from mode B to mode A) exhibited by the real thruster when a 160 V anode voltage is applied, as well as the decrease of discharge current above 220 V. Nevertheless, the obtained discharge current values are compatible with the measurements if the comparison is restricted to operational mode B, for anode voltages above 160 V.

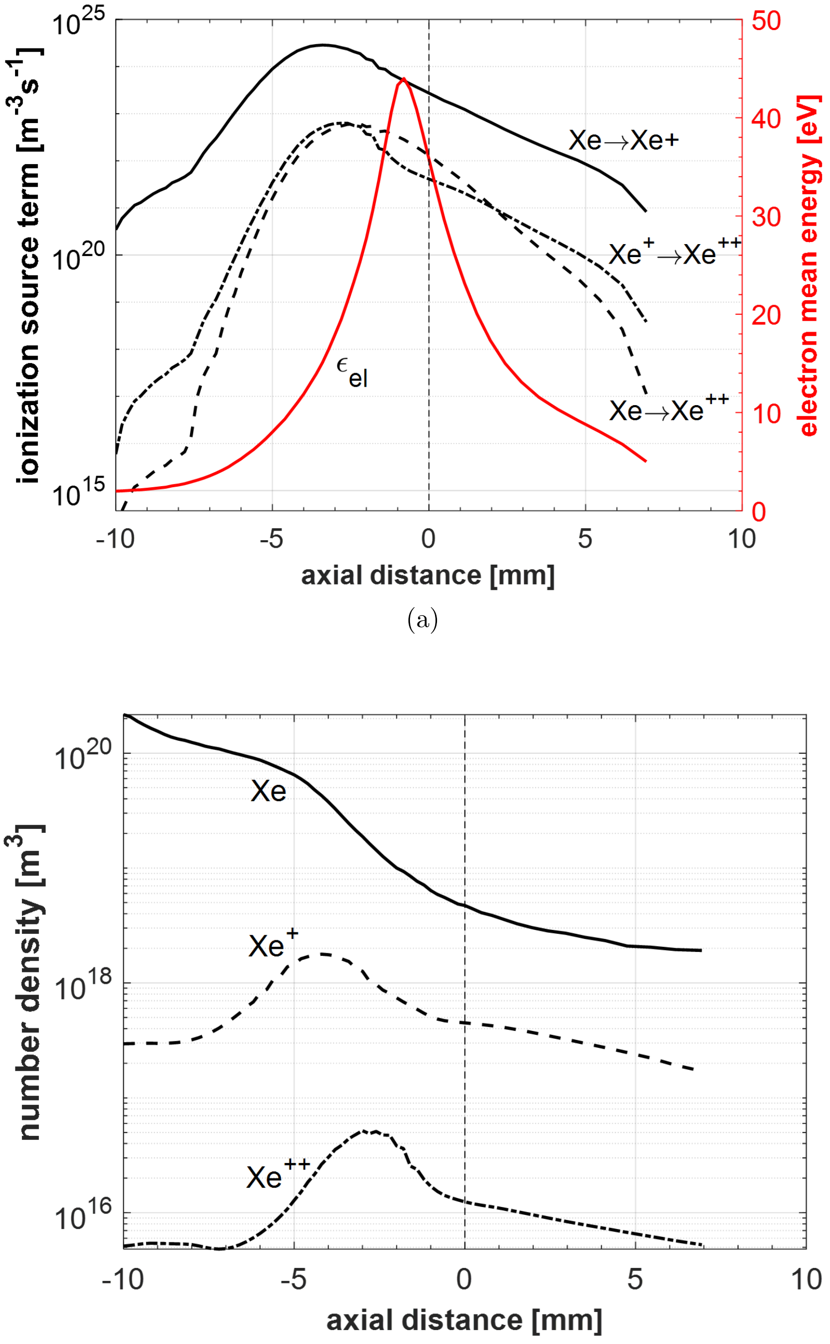

(a)

(b)

Figure 5.11: (a) ionization source terms and mean electron density along the thruster channel axis when the anomalous electron collision frequency in Fig. 5.9b is enforced; (b) corresponding axial distribution of neutral and ionized Xe

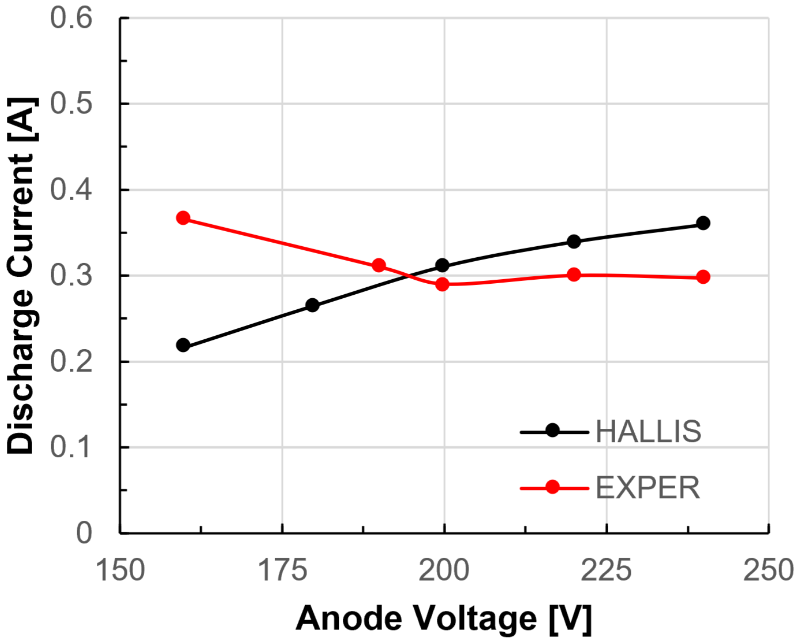

Figure 5.12: Experimental (red) and simulated (black) I-V characteristic for the KmHT-20 annular Hall thruster; The simulated results have been obtained with the anomalous collision frequency profile ν_{an} shown in Fig. 5.9, using a fixed flow rate of 0.42 $\mathrm{mg\,s^{-1}}$

5.3.2 Mode A

Unfortunately, the applicability of *HALLIS* to the simulation of Mode A is strongly limited by an intrinsic feature of the code. As anticipated, *HALLIS* employs the magnetic field line that intersects the cathode as the right end of the quasi-one dimensional grid (λ) used to solve the transport of electrons. Unfortunately, the magnetic topology of the KmHT-20 yields a magnetic field distribution where the cathodic magnetic field line is located close to the channel exit. Thus, the domain end is forcefully located 8 mm after the channel exit. In addition, the electric potential – which must obey to the Dirichlet boundary condition enforced at the cathodic line – starts to exhibit a non-physical behaviour after 6 mm from the channel exit. This explains the discrepancies between the computed and calculated mean ion velocity mentioned in the discussion of Fig. 5.8 and Fig. 5.9.

For the above reasons, the analysis conducted with this thruster magnetic topology is limited to the first millimetres after the channel exit. The LIF measurements provided in Figure 5 show that, while 8 mm from the channel exit are sufficient to capture the majority of the Xe ions acceleration in Mode B, the same cannot be stated for Mode A, where acceleration of the ions takes place over several centimetres from the channel exit. Nevertheless, the same procedure employed for the analysis of the operational mode B was adopted for mode A.

Figure 5.13 shows the global thruster performances as a function of empirical parameters α and k_b for a thruster operated in mode A, i.e., with 160 V anode voltage and 0.32 mg s^{-1}of Xe flow rate. The range for α and k_b is the same that has been discussed and employed in the previous section for the analysis of operational mode B. As one can see from Fig. 5.13a, 5.13b and 5.13c, while the employed range of empirical parameters allowed to reach anode efficiency levels comparable to the measurements, the computed discharge current and thrust are lower than the measurements in Table 5.1.

Analogously to what has been performed in the Mode B analysis, the result that minimizes the sum of the relative differences in terms of computed discharge current (I_d), thrust (T) and anode efficiency (η) with respect to the measurements, is given by $\alpha = 4$ and $k_b = 0.875$. The obtained thrust is 1.94 mN (with Isp=618s), while the discharge current and anode efficiency are 0.20 A and 0.19, respectively.

From the analysis of Fig. 5.13a, 5.13b and 5.13d, the maximum values of I_d ant T are

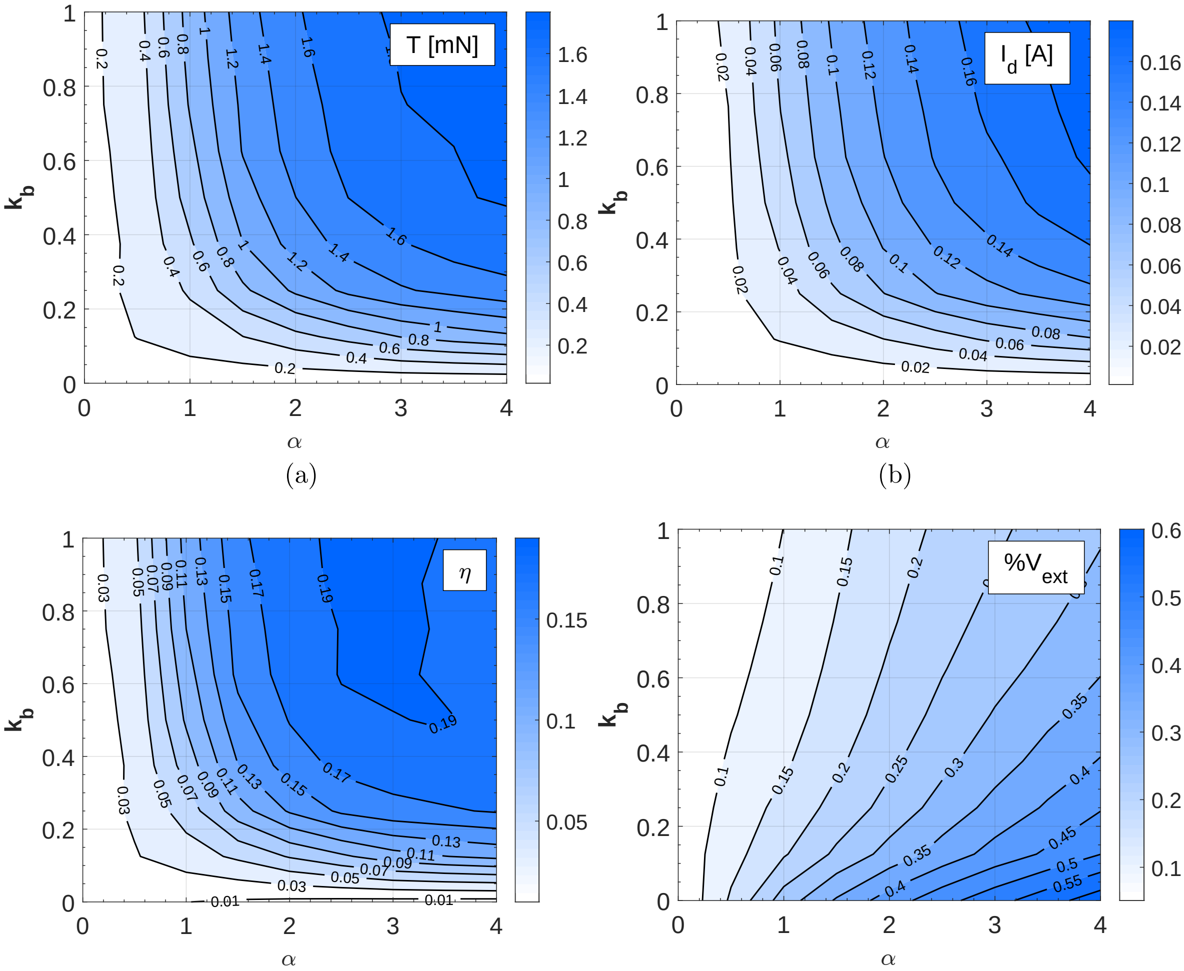

(a)

(b)

(c)

(d)

Figure 5.13: Mode A (160V; 0.32 $\mathrm{mg\,s^{-1}}$) – thrust (a), discharge current (b), efficiency (c) and ratio between the voltage drop after the channel exit and the total voltage drop along the thruster channel axis (d) as a function of empirical parameters α (wall momentum losses) and k_b (Bohm anomalous transport).

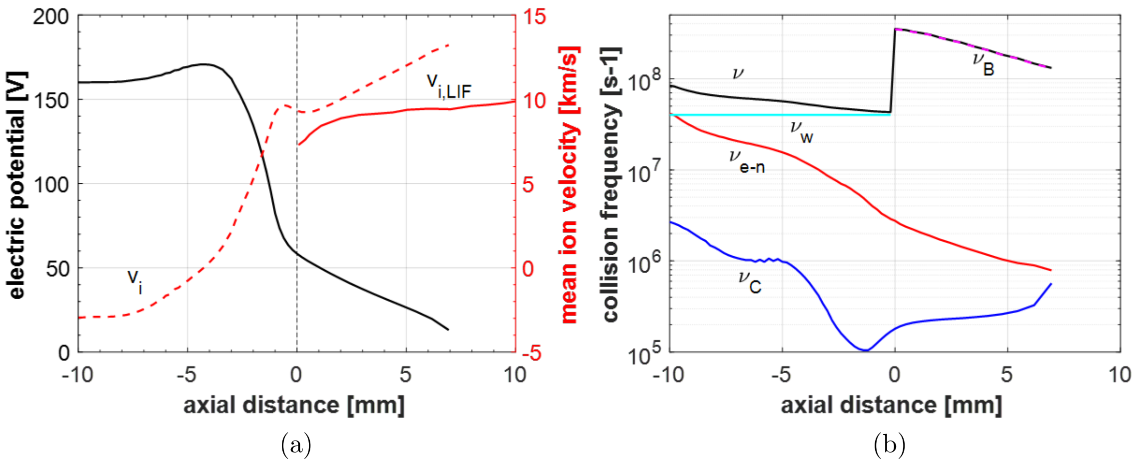

(a) (b)

Figure 5.14: Simulation of mode A using empirical parameters for anomalous electron transport ($\alpha = 4, k_b = 0.875$); (a) electric potential and mean ion velocity along the thruster channel axis, comparison between the computed velocities and the LIF measurements; (b) employed anomalous collision frequency values along the channel axis

found for values of α and k_b causing a consistent part of the voltage drop to take place inside the thruster channel. This, as previously discussed, leads to a high mean ion velocity at the channel exit. Figure 5.14a shows a comparison between the computed and measured ion velocity, along with the momentum-exchange collision frequency in Fig. 5.14b. The latter features a sharp discontinuity between the inner and outer channel collision frequencies, causing the described marked voltage drop inside the channel. Unfortunately, while the best thruster performances are achieved with such an acceleration structure, the obtained v_i profile is not compatible with the measured velocity, which exhibits a more gradual acceleration.

For the sake of completeness, the considered mode A has been also analysed with the second methodology employed for the analysis of mode B in the previous section. The anomalous collision frequency profile depicted in Fig. 5.15b has been enforced along the channel axis in in order to obtain a mean ion velocity compliant with the LIF measurements. The latter is shown Fig. 5.15a, along with the corresponding voltage drop across the thruster exit.

As can be noticed, a reasonable accuracy between the simulated and experimental mean ion velocity axial profiles has been achieved. Nevertheless, it has not been possible

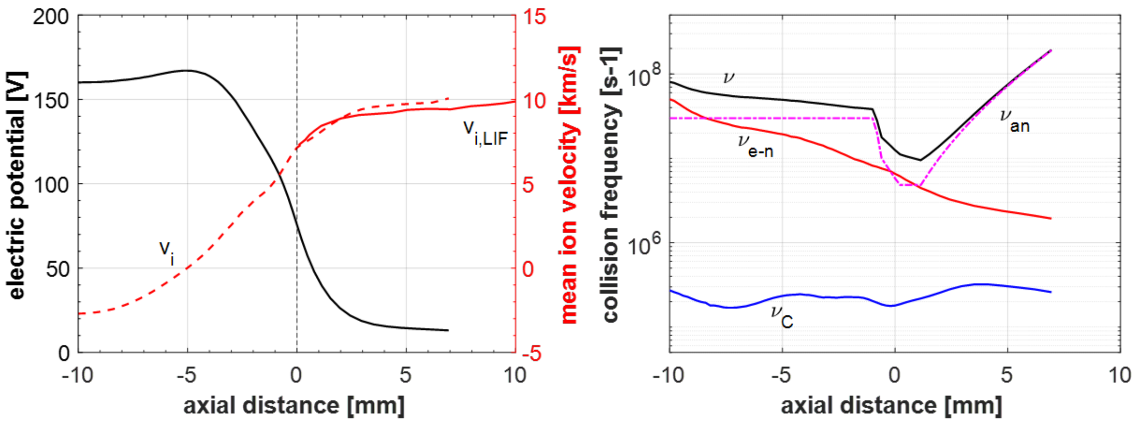

(a) (b)

Figure 5.15: Simulation of mode A enforcing the anomalous collision frequency along the thruster channel axis; (a) electric potential and mean ion velocity along the channel axis, comparison between the computed velocities and the LIF measurements; (b) employed anomalous collision frequency values

Table 5.5: Mode A, comparison between the measured thruster performances and results obtained enforcing the anomalous frequency profileν_{an} depicted in Fig. 5.15b.

Mode A	**[V]**	**P [W]**	**$\mathbf{I_d}$[A]**	**T [N]**	**Isp [s]**	**Anode Eff [-]**
EXPER	160	58.4	0.365	3.10E-03	820	0.21
HALLIS	160	9.87	0.049	6.70E-04	162	0.07

to match the target discharge current I_d^* while respecting the constraint on v_i provided by the LIF measurements. A quantitative overview of the results obtained with the ν_{an} profile depicted in Fig. 5.15b is provided in Table 5.5.

5.4 Summary

In this chapter, two different operational modes of a miniaturized annular Hall thruster have been assessed with the hybrid code *HALLIS*. The analysis has been carried out by comparing the results yielded by two different treatments of the anomalous electron transport with experimental measurements. In particular, the information provided by LIF spectroscopic measurements of the mean ion velocities, combined with the measured thruster performances, has been used to infer the anomalous transport collision frequency along the axis of the thruster. Whenever the limitations on the size of the computational grid employed in the code allowed to capture a substantial part of the acceleration of the (singly and doubly) ions, the simulated results show a satisfactory agreement with the available experimental data. Overall, the study shows that – in the context of modelling this kind of devices with non self-consistent methodologies, i.e., that rely on empirical parameters – the macroscopic information provided by the measurements of the thruster performances is not sufficient to provide an exhaustive representation of the detailed physics involved in such devices. In this spirit, thanks to the microscopic information provided by LIF measurements, the enforcement of the anomalous collision frequency allowed to accurately predict the acceleration structure of the KmHT-20 thruster, as well as the fraction of doubly charged ions produced when the thruster is operated in Mode B. Finally, the respective efficiency of the two kinetic channels (double ionization from the ground state and stepwise ionization) for the doubly charged ions production has been assessed and correlated with the computed spatial distribution of the species.

6 Conclusion

This work focused on the numerical modelling of non-equilibrium plasma devices, through the development of computational codes based on fluid and kinetic approaches.

A fluid model has been developed for the assessment of the plasma dynamics taking place in devices operating at atmospheric pressure. The adopted macroscopic description of the charged species transport allowed to perform simulations over time-lengths in the order of milliseconds. Two different fluid methodologies have been presented. In the Full Drift Diffusion (FDD) approach, the continuity equation for the number density of each specie is solved to obtain the electric charge density distribution. This is in turn employed as the source term of a linear Poisson problem. The solution of the latter yields the electric potential distribution over the considered domain. The fluxes are expressed in the drift-diffusion form and are discretised using the Finite Volume method. Conversely, in the developed Boltzmann Drift Diffusion (BDD) approach, the electrons are assumed to instantaneously adapt to the local electrostatic field caused by external applied voltages and the motion of the heavy ions. The electrons are therefore excluded from the drift-diffusion approach, and their spatial distribution is computed using the Boltzmann relation, leading to a non-linear electrostatic Poisson problem. In both approaches, the contribution of the chemical kinetic processes in the continuity equation is computed using a semi-implicit methodology. The latter has been validated against a well-known implicit numerical integrator.

The developed computational code implementing the FDD and BDD approaches has been applied to the simulation of a Dielectric Barrier Discharge (DBD) volumetric reactor, operating with atmospheric pressure air. The results yielded by the FDD approach over several cycles of the applied high-voltage waveform showed how the overall physics taking place in the gas gap is dominated by the electric charge deposition phenomena. A charge density distribution can indeed be deposited on the of the surfaces of the dielectric layers covering the electrodes, due to incident fluxes of the different charged species. The BDD approach allows a dramatic reduction of the computational burden associated with the explicit integration of the electron transport dynamics. The comparison between the simulation results yielded by the two (BDD and FDD) methodologies shows that the two approaches are in reasonable agreement. Furthermore, the electric surface charge density accumulated on the dielectric layers computed with the proposed BDD approach has been positively compared with experimental measurements. These latter have been performed by measuring the electric potential induced on the dielectric layers with an electrostatic probe. Finally, while in this work the developed fluid model has been applied to the simulation of DBDs, the adopted approach can be easily extended to other devices. Indeed, the same code – with a different set of chemical reactions and macroscopic parameters – is currently being employed to simulate atmospheric pressure plasma jets in pure helium.

In the second part of this work, a hybrid fluid/Particle-In-Cell code has been employed to study a miniaturized Hall thruster for space propulsion. The code operates on a 2D axially symmetric geometry. The ionic species are modelled using the Particle-In-Cell technique on a Cartesian grid. The electron transport and energy conservation equations are solved with a fluid model on a quasi 1-D grid along the magnetic field lines, under the Morozov thermalized potential approximation. The analysis has been carried out by comparing the results yielded by two different treatments of the anomalous electron transport with experimental measurements. In particular, the information provided by Laser Induced Fluorescence (LIF) spectroscopic measurements of the mean ion velocities – combined with the measured thruster performances – has been used to infer the anomalous transport collision frequency along the axis of the thruster. The obtained results showed a satisfactory agreement with the available experimental data when an appropriately extended grid has been employed. Indeed, it has been shown that the computational grid must be large enough to capture a substantial part of the acceleration of the (singly and doubly) ions. Overall, the study highlights that – in the context of modelling this kind of devices with non self-consistent methodologies, i.e., that rely on empirical parameters – the macroscopic information provided by the measurements of the thruster performances is not sufficient to provide an exhaustive representation of the detailed physics involved in such devices. In this spirit, thanks to the microscopic information provided by LIF measurements, the enforcement of the anomalous collision frequency allowed to accurately predict the acceleration structure of the considered Hall thruster, as well as the obtained fraction of doubly charged ions.

Finally, the respective efficiency of the two kinetic channels for the doubly charged ions production – double ionization from the ground state and stepwise ionization – has been assessed and correlated with the computed spatial distribution of the species.

Bibliography

[1] U. Kogelschatz, “Dielectric-barrier discharges: Their history, discharge physics, and industrial applications,” *Plasma Chemistry and Plasma Processing*, vol. 23, 03 2003.

[2] I. K. Dan M. Goebel, *Fundamentals of electric propulsion: ion and Hall thrusters.* JPL Space Science and Technology Series, Wiley, 2008.

[3] R. E. Bank, W. M. Coughran, W. Fichtner, E. H. Grosse, D. J. Rose, and R. K. Smith, “Transient simulation of silicon devices and circuits,” *IEEE Transactions on Computer-Aided Design of Integrated Circuits and Systems*, vol. 4, no. 4, pp. 436–451, 1985.

[4] M. Hosea and L. Shampine, “Analysis and implementation of tr-bdf2,” *Applied Numerical Mathematics*, vol. 20, no. 1-2, pp. 21–37, 1996.

[5] B. Parent, S. O. Macheret, and M. N. Shneider, “Electron and ion transport equations in computational weakly-ionized plasmadynamics,” *Journal of Computational Physics*, vol. 259, pp. 51–69, 2014.

[6] J. A. Bittencourt, *Fundamentals of plasma physics.* Springer Science & Business Media, 2013.

[7] K. H. Becker, U. Kogelschatz, K. Schoenbach, and R. Barker, *Non-equilibrium air plasmas at atmospheric pressure.* CRC press, 2004.

[8] G. E. Georghiou, A. P. Papadakis, R. Morrow, and A. C. Metaxas, “Numerical modelling of atmospheric pressure gas discharges leading to plasma production,” *Journal of Physics D: Applied Physics*, vol. 38, pp. R303–R328, sep 2005.

[9] J. R. Roth, *Industrial plasma engineering: Volume 2: Applications to nonthermal plasma processing*, vol. 2. CRC press, 2001.

[10] M. Kogoma and S. Okazaki, "Raising of ozone formation efficiency in a homogeneous glow discharge plasma at atmospheric pressure," *Journal of Physics D: Applied Physics*, vol. 27, pp. 1985–1987, sep 1994.

[11] U. Kogelschatz, *Advanced Ozone Generation*, pp. 87–118. Boston, MA: Springer US, 1988.

[12] S. Kanazawa, M. Kogoma, T. Moriwaki, and S. Okazaki, "Stable glow plasma at atmospheric pressure," *Journal of Physics D: Applied Physics*, vol. 21, no. 5, p. 838, 1988.

[13] S. Okazaki, M. Kogoma, M. Uehara, and Y. Kimura, "Appearance of stable glow discharge in air, argon, oxygen and nitrogen at atmospheric pressure using a 50 hz source," *Journal of Physics D: Applied Physics*, vol. 26, no. 5, p. 889, 1993.

[14] Y. Sawada, H. Tamaru, M. Kogoma, M. Kawase, and K. Hashimoto, "The reduction of copper oxide thin films with hydrogen plasma generated by an atmospheric-pressure glow discharge," *Journal of Physics D: Applied Physics*, vol. 29, no. 10, p. 2539, 1996.

[15] L. Mangolini, K. Orlov, U. Kortshagen, J. Heberlein, and U. Kogelschatz, "Radial structure of a low-frequency atmospheric-pressure glow discharge in helium," *Applied physics letters*, vol. 80, no. 10, pp. 1722–1724, 2002.

[16] R. Dorai and M. J. Kushner, "A model for plasma modification of polypropylene using atmospheric pressure discharges," *Journal of Physics D: Applied Physics*, vol. 36, no. 6, p. 666, 2003.

[17] V. Nikonov, R. Bartnikas, and M. Wertheimer, "Surface charge and photoionization effects in short air gaps undergoing discharges at atmospheric pressure," *Journal of physics D: applied physics*, vol. 34, no. 19, p. 2979, 2001.

[18] J. Boeuf, "Plasma display panels: physics, recent developments and key issues," *Journal of physics D: Applied physics*, vol. 36, no. 6, p. R53, 2003.

[19] G. Hagelaar, M. Klein, R. Snijkers, and G. Kroesen, "Energy loss mechanisms in the microdischarges in plasma display panels," *Journal of applied physics*, vol. 89, no. 4, pp. 2033–2039, 2001.

[20] B. Eliasson and U. Kogelschatz, “Nonequilibrium volume plasma chemical processing,” *IEEE Transactions on Plasma Science*, vol. 19, no. 6, pp. 1063–1077, 1991.

[21] Y. Ju, “Plasma assisted combustion” plasma assisted combustion,”,” *Progress in Energy and Combustion Science*, vol. 48, pp. 21–83, 2015.

[22] K. Zhang, B. Eliasson, and U. Kogelschatz, “Direct Conversion of Greenhouse Gases to Synthesis Gas and C4 Hydrocarbons over Zeolite HY Promoted by a Dielectric-Barrier Discharge,” *Industrial & Engineering Chemistry Research*, vol. 41, pp. 1462–1468, Mar. 2002.

[23] A. Mizuno, “Electrostatic precipitation,” *IEEE Transactions on Dielectrics and Electrical Insulation*, vol. 7, no. 5, pp. 615–624, 2000.

[24] T. Hammer, “Application of Plasma Technology in Environmental Techniques,” *Contributions to Plasma Physics*, vol. 39, no. 5, pp. 441–462, 1999.

[25] S. Kuo, I. M. Kalkhoran, D. Bivolaru, and L. Orlick, “Observation of shock wave elimination by a plasma in a mach-2.5 flow,” *Physics of Plasmas*, vol. 7, no. 5, pp. 1345–1348, 2000.

[26] J. Shang, S. Surzhikov, R. Kimmel, D. Gaitonde, J. Menart, and J. Hayes, “Mechanisms of plasma actuators for hypersonic flow control,” *Progress in Aerospace Sciences*, vol. 41, no. 8, pp. 642–668, 2005.

[27] J.-J. Wang, K.-S. Choi, L.-H. Feng, T. N. Jukes, and R. D. Whalley, “Recent developments in dbd plasma flow control,” *Progress in Aerospace Sciences*, vol. 62, pp. 52–78, 2013.

[28] A. Cristofolini, C. A. Borghi, and G. Neretti, “Charge distribution on the surface of a dielectric barrier discharge actuator for the fluid-dynamic control,” *Journal of Applied Physics*, vol. 113, no. 14, p. 143307, 2013.

[29] E. Ahedo, “Plasmas for space propulsion,” *Plasma Physics and Controlled Fusion*, vol. 53, no. 12, p. 124037, 2011.

[30] K. R. Stalder, “Plasma characteristics of electrosurgical discharges,” in *APS Annual Gaseous Electronics Meeting Abstracts*, pp. ET1–002, 2003.

[31] P. Cools, R. Ghobeira, S. V. Vrekhem, N. D. Geyterand, and R. Morent, "Non-thermal plasma technology for the improvement of scaffolds for tissue engineering and regenerative medicine-a review," in *Plasma Science and Technology* (T. Mieno, ed.), ch. 8, Rijeka: IntechOpen, 2016.

[32] P. K. Chu, J. Chen, L. Wang, and N. Huang, "Plasma-surface modification of biomaterials," *Materials Science and Engineering: R: Reports*, vol. 36, no. 5-6, pp. 143–206, 2002.

[33] L. Minati, C. Migliaresi, L. Lunelli, G. Viero, M. Dalla Serra, and G. Speranza, "Plasma assisted surface treatments of biomaterials," *Biophysical Chemistry*, vol. 229, pp. 151–164, 2017.

[34] L. A. Fridman, Alexander; Kennedy, *Plasma Physics and Engineering, Second Edition.* CRC Press, 2nd ed., 2011.

[35] M. Laroussi, "Low temperature plasma-based sterilization: overview and state-of-the-art," *Plasma processes and polymers*, vol. 2, no. 5, pp. 391–400, 2005.

[36] S. Perni, D. W. Liu, G. Shama, and M. G. Kong, "Cold atmospheric plasma decontamination of the pericarps of fruit," *Journal of food protection*, vol. 71, no. 2, pp. 302–308, 2008.

[37] E. Noriega, G. Shama, A. Laca, M. Díaz, and M. G. Kong, "Cold atmospheric gas plasma disinfection of chicken meat and chicken skin contaminated with listeria innocua," *Food microbiology*, vol. 28, no. 7, pp. 1293–1300, 2011.

[38] T. Xia, M. Yang, I. Marabella, E. Lee, B. Olson, D. Zarling, M. Torremorell, and H. Clack, "Inactivation of airborne porcine reproductive and respiratory syndrome virus (prrsv) by a packed bed dielectric barrier discharge non-thermal plasma," *Journal of Hazardous Materials*, vol. 393, p. 122266, 2020.

[39] R. Brandenburg, "Dielectric barrier discharges: progress on plasma sources and on the understanding of regimes and single filaments," *Plasma Sources Science and Technology*, vol. 26, no. 5, p. 053001, 2017.

[40] W. Siemens, "Ueber die elektrostatische induction und die verzögerung des stroms in flaschendrähten," *Annalen der Physik*, vol. 178, no. 9, pp. 66–122, 1857.

[41] J. Ehlbeck, U. Schnabel, M. Polak, J. Winter, T. von Woedtke, R. Brandenburg, T. von dem Hagen, and K.-D. Weltmann, “Low temperature atmospheric pressure plasma sources for microbial decontamination,” *Journal of Physics D: Applied Physics*, vol. 44, p. 013002, dec 2010.

[42] N. Gomathi, A. K. Chanda, and S. Neogi, *Atmospheric Plasma Treatment of Polymers for Biomedical Applications*, ch. 7, pp. 199–215. Wiley, 2013.

[43] C. Tendero, C. Tixier, P. Tristant, J. Desmaison, and P. Leprince, “Atmospheric pressure plasmas: A review,” *Spectrochimica Acta Part B: Atomic Spectroscopy*, vol. 61, no. 1, pp. 2–30, 2006.

[44] A. Fridman, A. Chirokov, and A. Gutsol, “Non-thermal atmospheric pressure discharges,” *Journal of Physics D: Applied Physics*, vol. 38, no. 2, p. R1, 2005.

[45] J. J. S. Shang and S. T. Surzhikov, *Plasma Dynamics for Aerospace Engineering*. Cambridge Aerospace Series, Cambridge University Press, 2018.

[46] V. V. Zhurin, H. R. Kaufman, and R. S. Robinson, “Physics of closed drift thrusters,” *Plasma Sources Science and Technology*, vol. 8, pp. R1–R20, jan 1999.

[47] R. G. Jahn, *Physics of Electric Propulsion*. Dover Publications, 2006.

[48] J.-P. Boeuf, “Tutorial: Physics and modeling of hall thrusters,” *Journal of Applied Physics*, vol. 121, no. 1, p. 011101, 2017.

[49] G. M. W. Kroesen, D. C. Schram, C. J. Timmermans, and J. C. M. de Haas, “The energy balance of a plasma in partial local thermodynamic equilibrium,” *IEEE Transactions on Plasma Science*, vol. 18, no. 6, pp. 985–991, 1990.

[50] M. A. Lieberman and A. J. Lichtenberg, *Principles of Plasma Discharges and Materials Processing*. Wiley-Interscience, 2nd ed., 2005.

[51] F. F. Chen, *Introduction to plasma physics and controlled fusion*. Springer, 3rd ed., 2016.

[52] A. M. Howatson, *An Introduction to Gas Discharges*. Pergamon, 2nd ed., 1965.

[53] J. Shang and P. Huang, “Modeling of ac dielectric barrier discharge,” *Journal of applied physics*, vol. 107, no. 11, p. 113302, 2010.

[54] J. Shang, F. Roveda, and P. Huang, "Electrodynamic force of dielectric barrier discharge," *Journal of Applied Physics*, vol. 109, no. 11, p. 113301, 2011.

[55] J.-P. Boeuf, "A two-dimensional model of dc glow discharges," *Journal of applied physics*, vol. 63, no. 5, pp. 1342–1349, 1988.

[56] J. Poggie, "Numerical simulation of direct current glow discharges for high-speed flow control," *Journal of Propulsion and Power*, vol. 24, no. 5, pp. 916–922, 2008.

[57] S. T. Surzhikov and J. S. Shang, "Two-component plasma model for two-dimensional glow discharge in magnetic field," *Journal of Computational Physics*, vol. 199, no. 2, pp. 437–464, 2004.

[58] S. O. Macheret, M. N. Shneider, and R. B. Miles, "Modeling of air plasma generation by repetitive high-voltage nanosecond pulses," *IEEE Transactions on Plasma Science*, vol. 30, no. 3, pp. 1301–1314, 2002.

[59] S. Roy, B. Pandey, J. Poggie, and D. V. Gaitonde, "Modeling low pressure collisional plasma sheath with space-charge effect," *Physics of Plasmas*, vol. 10, no. 6, pp. 2578–2585, 2003.

[60] W. Schmitt, W. E. Köhler, and H. Ruder, "A one-dimensional model of dc glow discharges," *Journal of applied physics*, vol. 71, no. 12, pp. 5783–5791, 1992.

[61] D. B. Graves and K. F. Jensen, "A continuum model of dc and rf discharges," *IEEE Transactions on plasma science*, vol. 14, no. 2, pp. 78–91, 1986.

[62] A. V. Likhanskii, M. N. Shneider, S. O. Macheret, and R. B. Miles, "Modeling of dielectric barrier discharge plasma actuator in air," *Journal of Applied Physics*, vol. 103, no. 5, p. 053305, 2008.

[63] D. J. Griffiths, *Introduction to Electrodynamics.* Cambridge University Press, 4th ed., 2017.

[64] M. P. Joel H. Ferziger, *Computational methods for fluid dynamics.* Springer, 3rd ed., 2002.

[65] J. D. Anderson and J. Wendt, *Computational fluid dynamics*, vol. 206. Springer, 1995.

[66] A. Cristofolini, A. Popoli, and G. Neretti, “A multi-stage model for dielectric barrier discharge in atmospheric pressure air,” *International Journal of Applied Electromagnetics and Mechanics*, vol. 63, pp. S21–S29, 2020.

[67] M. C. Michael Metcalf, John Reid, *Modern Fortran Explained: Incorporating Fortran 2018 (Numerical Mathematics and Scientific Computation).* Numerical Mathematics and Scientific Computation, Oxford University Press, 5th ed., 2018.

[68] G. Sharma and J. Martin, “MATLAB®: A Language for Parallel Computing,” *International Journal of Parallel Programming*, vol. 37, pp. 3–36, Feb. 2009.

[69] J. F. Thompson, B. K. Soni, and N. P. Weatherill, *Handbook of grid generation.* CRC press, 1998.

[70] D. Nikandrovand, L. Tsendin, R. Arslanbekov, and V. Kolobov, “Dynamics of ionization fronts during high-pressure gas breakdown,” in *Proceedings of the 59th Annual Gaseous Electronics Conference, vol. SRP2, Columbus, OH*, p. 31, 2006.

[71] S. Pancheshnyi, P. Ségur, J. Capeillère, and A. Bourdon, “Numerical simulation of filamentary discharges with parallel adaptive mesh refinement,” *Journal of Computational Physics*, vol. 227, no. 13, pp. 6574–6590, 2008.

[72] W.-G. Min, H.-S. Kim, S.-H. Lee, and S.-Y. Hahn, “A study on the streamer simulation using adaptive mesh generation and fem-fct,” *IEEE transactions on magnetics*, vol. 37, no. 5, pp. 3141–3144, 2001.

[73] G. Sinnott, D. Golden, and R. Varney, “Positive-ion mobilities in dry air,” *Physical Review*, vol. 170, no. 1, p. 272, 1968.

[74] Y. Gosho and A. Harada, “A new technique for measuring negative ion mobilities at atmospheric pressure,” *Journal of Physics D: Applied Physics*, vol. 16, no. 7, p. 1159, 1983.

[75] I. S. Grigoriev and E. Z. Meæilikhov, *Handbook of physical quantities.* CRC Press, 1997.

[76] J. Anderson, John D., *Fundamentals of aerodynamics; 5th ed. in SI units.* McGraw-Hill series in aeronautical and aerospace engineering, Singapore: McGraw-Hill, 2011.

[77] E. Anderson, Z. Bai, C. Bischof, S. Blackford, J. Demmel, J. Dongarra, J. Du Croz, A. Greenbaum, S. Hammarling, A. McKenney, and D. Sorensen, *LAPACK Users' Guide*. Philadelphia, PA: Society for Industrial and Applied Mathematics, 3rd ed., 1999.

[78] O. Schenk and K. Gärtner, "Solving unsymmetric sparse systems of linear equations with PARDISO," *Future Generation Computer Systems*, vol. 20, no. 3, pp. 475–487, 2004.

[79] I. Kossyi, A. Y. Kostinsky, A. Matveyev, and V. Silakov, "Kinetic scheme of the non-equilibrium discharge in nitrogen-oxygen mixtures," *Plasma Sources Science and Technology*, vol. 1, no. 3, p. 207, 1992.

[80] F. Massines, A. Rabehi, P. Decomps, R. B. Gadri, P. Ségur, and C. Mayoux, "Experimental and theoretical study of a glow discharge at atmospheric pressure controlled by dielectric barrier," *Journal of Applied Physics*, vol. 83, pp. 2950–2957, 3 1998.

[81] A. Likhanskii, M. Shneider, S. Macheret, and R. Miles, "Modeling of interaction between weakly ionized near-surface plasmas and gas flow," in *44th AIAA Aerospace Sciences Meeting and Exhibit*, p. 1204, 2006.

[82] J. Boeuf, Y. Lagmich, T. Unfer, T. Callegari, and L. Pitchford, "Electrohydrodynamic force in dielectric barrier discharge plasma actuators," *Journal of Physics D: Applied Physics*, vol. 40, no. 3, p. 652, 2007.

[83] J. Boeuf, Y. Lagmich, and L. Pitchford, "Contribution of positive and negative ions to the electrohydrodynamic force in a dielectric barrier discharge plasma actuator operating in air," *Journal of applied physics*, vol. 106, no. 2, p. 023115, 2009.

[84] N. Y. Babaeva and G. Naidis, "Two-dimensional modelling of positive streamer dynamics in non-uniform electric fields in air," *Journal of Physics D: Applied Physics*, vol. 29, no. 9, p. 2423, 1996.

[85] N. Y. Babaeva and G. V. Naidis, "Dynamics of positive and negative streamers in air in weak uniform electric fields," *IEEE transactions on plasma science*, vol. 25, no. 2, pp. 375–379, 1997.

[86] A. Cristofolini and A. Popoli, “A multi-stage approach for dbd modelling,” in *Journal of Physics: Conference Series*, vol. 1243, p. 012012, IOP Publishing, 2019.

[87] A. Cristofolini, G. Neretti, A. Popoli, A. Ricchiuto, and P. Seri, “Experimental and numerical investigation on the electric charge deposition in a dielectric barrier discharge,” in *2019 IEEE Conference on Electrical Insulation and Dielectric Phenomena (CEIDP)*, pp. 690–693, IEEE, 2019.

[88] C. A. Borghi, A. Cristofolini, F. A. Dragonas, G. Grandi, and G. Neretti, “Development of a multilevel plasma generator for dielectric barrier discharge actuators,” in *45th AIAA Plasmadynamics and Lasers Conference*, p. 2668, 2014.

[89] C. A. Borghi, A. Cristofolini, G. Grandi, G. Neretti, and P. Seri, “A plasma aerodynamic actuator supplied by a multilevel generator operating with different voltage waveforms,” *Plasma Sources Science and Technology*, vol. 24, no. 4, p. 045018, 2015.

[90] P. Seri, A. Wright, A. Shaw, F. Iza, H. Bandulasena, C. A. Borghi, and G. Neretti, “Influence of the voltage waveform’s shape and on-time duration on the dissolved ozone produced by a dbd bubble reactor,” *Plasma Sources Science and Technology*, vol. 28, no. 3, p. 035001, 2019.

[91] L. Brieda, *Plasma Simulations by Example.* CRC Press, 1st ed., 2019.

[92] K. Fujimoto, “Multi-scale kinetic simulation of magnetic reconnection with dynamically adaptive meshes,” *Frontiers in Physics*, vol. 6, p. 119, 2018.

[93] C. P. Sishtla, V. Olshevsky, S. W. Chien, S. Markidis, and E. Laure, “Particle-in-cell simulations of plasma dynamics in cometary environment,” in *Journal of Physics: Conference Series*, vol. 1225, p. 012009, IOP Publishing, 2019.

[94] J. Tenbarge and G. Howes, “Kinetic simulations of solar wind turbulence and heating,” *APS*, vol. 52, pp. PM1–000, 2010.

[95] A. Fedoseyev, V. Kolobov, R. Arslanbekov, and A. Przekwas, “Kinetic simulation tools for nano-scale semiconductor devices,” *Microelectronic engineering*, vol. 69, no. 2-4, pp. 577–586, 2003.

[96] L. Garrigues, G. Fubiani, and J. Boeuf, "Appropriate use of the particle-in-cell method in low temperature plasmas: Application to the simulation of negative ion extraction," *Journal of Applied Physics*, vol. 120, no. 21, 2016.

[97] G. Fubiani, L. Garrigues, and J. Boeuf, "Modeling of negative ion extraction from a magnetized plasma source: Derivation of scaling laws and description of the origins of aberrations in the ion beam," *Physics of Plasmas*, vol. 25, no. 2, 2018.

[98] R. Khaziev and D. Curreli, "hpic: A scalable electrostatic particle-in-cell for plasma–material interactions," *Computer Physics Communications*, vol. 229, pp. 87 – 98, 2018.

[99] J. Drobny and D. Curreli, "F-tridyn simulations of tungsten self-sputtering and applications to coupling plasma and material codes," *Computational Materials Science*, vol. 149, pp. 301–306, 2018.

[100] F. Taccogna and L. Garrigues, "Latest progress in hall thrusters plasma modelling," *Reviews of Modern Plasma Physics*, vol. 3, no. 1, p. 12, 2019.

[101] L. Brieda and D. VanGilder, "Multi-domain plasma expansion simulations using a particle-in-cell method," tech. rep., ENGINEERING RESEARCH AND CONSULTING INC (ERC INC) EDWARDS AFB CA, 2006.

[102] O. Buneman, "Dissipation of currents in ionized media," *Physical Review*, vol. 115, no. 3, p. 503, 1959.

[103] J. Dawson, "One-dimensional plasma model," *The Physics of Fluids*, vol. 5, no. 4, pp. 445–459, 1962.

[104] J. M. Dawson, "Particle simulation of plasmas," *Reviews of modern physics*, vol. 55, no. 2, p. 403, 1983.

[105] R. W. Hockney and J. W. Eastwood, *Computer simulation using particles.* crc Press, 1988.

[106] C. K. Birdsall and A. B. Langdon, *Plasma physics via computer simulation.* CRC press, 2004.

[107] R. Courant, K. Friedrichs, and H. Lewy, “On the partial difference equations of mathematical physics,” *IBM journal of Research and Development*, vol. 11, no. 2, pp. 215–234, 1967.

[108] K. Hammonds and D. Heyes, “Shadow hamiltonian in classical nve molecular dynamics simulations: A path to long time stability,” *The Journal of Chemical Physics*, vol. 152, no. 2, p. 024114, 2020.

[109] J. P. Boris, “Acceleration calculation from a scalar potential.,” tech. rep., Princeton Univ., NJ Plasma Physics Lab., 1970.

[110] J. P. Boris, “Relativistic plasma simulation-optimization of a hybrid code,” in *Proc. Fourth Conf. Num. Sim. Plasmas*, pp. 3–67, 1970.

[111] D. Tskhakaya, K. Matyash, R. Schneider, and F. Taccogna, “The particle-in-cell method,” *Contributions to Plasma Physics*, vol. 47, no. 8-9, pp. 563–594, 2007.

[112] S. D. Conte, C. De Boor, and C. W. De Boor, *Elementary numerical analysis: an algorithmic approach.* Mcgraw-Hill College, 1980.

[113] Y. Saad, *Iterative methods for sparse linear systems.* SIAM, 2003.

[114] Z. Pekárek, M. Lahuta, and R. Hrach, “Improving performance of multi-dimensional particle-in-cell codes for modelling of medium pressure plasma,” *Journal of Physics Conference Series*, vol. 63, 04 2007.

[115] R. Hrach, M. Lahuta, Z. Pekárek, and J. Šimek, “Multi-dimensional codes for particle modelling of plasma-solid interaction at higher pressures,” *Czechoslovak Journal of Physics*, vol. 56, no. 2, pp. B990–B995, 2006.

[116] P. Burger, “Elastic collisions in simulating one-dimensional plasma diodes on the computer,” *The Physics of Fluids*, vol. 10, no. 3, pp. 658–666, 1967.

[117] R. Shanny, J. M. Dawson, and J. M. Greene, “One-dimensional model of a lorentz plasma,” *The Physics of Fluids*, vol. 10, no. 6, pp. 1281–1287, 1967.

[118] M. Surendra, D. Graves, and G. Jellum, “Self-consistent model of a direct-current glow discharge: Treatment of fast electrons,” *Physical Review A*, vol. 41, no. 2, p. 1112, 1990.

[119] D. Vender and R. W. Boswell, "Numerical modeling of low-pressure rf plasmas," *IEEE transactions on plasma science*, vol. 18, no. 4, pp. 725–732, 1990.

[120] M. Surendra and D. B. Graves, "Particle simulations of radio-frequency glow discharges," *IEEE transactions on plasma science*, vol. 19, no. 2, pp. 144–157, 1991.

[121] C. Birdsall, "Particle-in-cell charged-particle simulations, plus monte carlo collisions with neutral atoms, PIC-MCC," *IEEE Transactions on Plasma Science*, vol. 19, pp. 65–85, 1991.

[122] J. Boeuf and L. Garrigues, "Low frequency oscillations in a stationary plasma thruster," *Journal of Applied Physics*, vol. 84, no. 7, pp. 3541–3554, 1998.

[123] G. Hagelaar, J. Bareilles, L. Garrigues, and J.-P. Boeuf, "Two-dimensional model of a stationary plasma thruster," *Journal of Applied Physics*, vol. 91, no. 9, pp. 5592–5598, 2002.

[124] J. Bareilles, G. Hagelaar, L. Garrigues, C. Boniface, J. Boeuf, and N. Gascon, "Critical assessment of a two-dimensional hybrid hall thruster model: Comparisons with experiments," *Physics of Plasmas*, vol. 11, no. 6, pp. 3035–3046, 2004.

[125] G. Hagelaar, J. Bareilles, L. Garrigues, and J.-P. Boeuf, "Role of anomalous electron transport in a stationary plasma thruster simulation," *Journal of Applied Physics*, vol. 93, no. 1, pp. 67–75, 2003.

[126] D. Rapp and P. Englander-Golden, "Total Cross Sections for Ionization and Attachment in Gases by Electron Impact. I. Positive Ionization," *The Journal of Chemical Physics*, vol. 43, pp. 1464–1479, Sept. 1965.

[127] R. C. Wetzel, F. A. Baiocchi, T. R. Hayes, and R. S. Freund, "Absolute cross sections for electron-impact ionization of the rare-gas atoms by the fast-neutral-beam method," *Physical Review A*, vol. 35, pp. 559–577, Jan. 1987.

[128] C. Achenbach, A. Muller, E. Salzborn, and R. Becker, "Single ionisation of multiply charged xenon ions by electron impact," *Journal of Physics B: Atomic and Molecular Physics*, vol. 17, pp. 1405–1425, Apr. 1984.

[129] A. Morozov, "Conditions for efficient current transport by near-wall conduction," *Sov. Phys. Tech. Phys*, vol. 32, no. 8, pp. 901–904, 1987.

[130] A. Bugrova, "Experimental investigation of near wall conductivity," *Sov. J. Plasma Phys.*, vol. 16, pp. 849–856, 1990.

[131] A. Morozov, Y. V. Esipchuk, A. Kapulkin, V. Nevrovskii, and V. Smirnov, "Azimuthally asymmetric modes and anomalous conductivity in closed electron drift accelerators," tech. rep., IV Kurchatov Atomic Energy Institute, Moscow, 1973.

[132] M. Hirakawa, "Electron transport mechanism in a hall thruster," in *26th International Electric Propulsion Conference, Cleveland, Ohio.*

[133] L. Garrigues, G. Hagelaar, C. Boniface, and J. Boeuf, "Anomalous conductivity and secondary electron emission in hall effect thrusters," *Journal of applied physics*, vol. 100, no. 12, p. 123301, 2006.

[134] D. Meeker, "FEMM – finite element method magnetics," 2019.

[135] D. Lee, H. Kim, S. Lee, G. Doh, and W. Choe, "Development and performance test of a 50 w-class hall thruster," in *36th International Electric Propulsion Conference (IEPC)*, University of Vienna, 2019.

[136] J. Bareilles, *Modélisation 2D hybride d'un propulseur à effet Hall pour satellites.* PhD thesis, Université de Toulouse, Université Toulouse III-Paul Sabatier, 2002.

[137] H. Kim, Y. Lim, W. Choe, and J. Seon, "Effect of multiply charged ions on the performance and beam characteristics in annular and cylindrical type hall thruster plasmas," *Applied Physics Letters*, vol. 105, no. 14, p. 144104, 2014.

[138] L. Garrigues, G. J. Hagelaar, J. P. Boeuf, Y. Raitses, A. Smirnov, and N. J. Fisch, "Simulations of a miniaturized cylindrical hall thruster," *IEEE transactions on plasma science*, vol. 36, no. 5, pp. 2034–2042, 2008.